Università degli Studi di Napoli "Parthenope"

Dipartimento di Ingegneria

Corso di Dottorato in Information and Communication
Technology and Engineering

XXXVII Cycle

Optimal design and energetic efficiency of Large Magnets for detectors in High Energy Physics

Year 2021-2024

Supervisor
Prof. Massimiliano de Magistris
Ph.D. Coordinator
Prof. Agostino Iadicicco

Ph.D. Candidate
Daniele Centanni

Daniele Centanni
ORCID: 0000-0001-6566-9838

ABSTRACT

Magnets are fundamental components in High Energy Physics (HEP) experiments, they are used both in particle accelerators and detectors to study the fundamental particles and forces of the Universe. In detectors such as those at CERN's Large Hadron Collider (LHC), large magnets play a critical role in identifying particles by analyzing the curvature of their tracks in a magnetic field, which provides charge and momentum information.

Magnet design in HEP has traditionally followed a stepwise process, beginning with analytical modelling followed by numerical validation, aiming to balance performance with cost efficiency. However, the increasing scarcity of resources and climate change challenges, largely linked to fossil fuel dependency, emphasize the need for more sustainable design practices in experimental physics. This Ph.D. work contributes to such a shift in magnet design philosophy, focusing on the development of an integrated optimization framework that considers energy efficiency alongside performance and technical constraints. The research proposes a reformulation of magnet design models to enhance their accuracy and interoperability for optimization purposes. Analytical and numerical tools have been developed and applied to the design of warm magnets within the context of the SND@LHC and SHiP collaborations at CERN. Results demonstrate the advantages of the integrated approach compared to traditional design methodologies, with a focus on balancing sustainability with experimental requirements.

CONTENTS

INTRODUCTION

Magnets are ubiquitous in the High Energy Physics field as they are essential tools to probe the smallest building blocks of our universe — fundamental particles and forces.

They are involved in particle accelerators as well as in detectors in experiments. In particle detectors, such as those used at the Large Hadron Collider (LHC) at CERN, large magnets play a vital role in identifying particles based on their behaviour in a magnetic field. In fact, when charged particles move through a magnetic field, they experience a force that causes them to curve. By observing their tracks' curvature, the charge and momentum of particles produced in different processes can be inferred.

Designing magnets is a complex task that must meet a wide range of requirements and constraints, from physics demands and expected performance to spatial limitations, budget considerations, and specific experiment needs. Traditional magnet design — at CERN in particular — established a step-by-step approach: an analytical design is created first, followed by a basic numerical design, that respects constraints and balances cost optimization while ensuring performance.

In recent years, however, the growing scarcity of resources and the impacts of climate change, largely driven by fossil fuel dependence, have made sustainable design concepts essential in particle experiments — particularly in magnet design. This — among other reasons — highlights the need for a shift in perspective on design and optimization processes. As a matter of fact, this Ph.D. work, within a larger scientific framework, is aimed at contributing to the effort on such a change of perspective, jointly involving different aspects of the design of warm magnets as part of a wider set of objectives and parameters considered at the same level, while focusing on energy efficiency.

Such a fresh approach therefore requires revisiting the formulation of models in order to achieve sufficient accuracy while making them more interoperable for easier optimization. This new proposed formulation of the optimization process is hence implemented through analytical and numerical tools and applied in different cases, in the context of the SND@LHC and SHiP Collaborations.

The thesis is structured in three chapters:

- **Chapter 1** provides an overview of the state of the art of large magnets involved in the major High Energy Physics experiments at CERN's LHC. Additionally, main features of the traditional methodology of warm magnet design are introduced, alongside a discussion about new perspectives arising from sustainability concerns.
- **Chapter 2** describes the considered models and tools involved in a mathematical framework for an integrated design of electro-magnets for detectors. Particular emphasis is given to analytical and semi-analytical models essential in the early phases of magnet design, whereas numerical tools are also discussed serving as field and particle interaction validation. Additionally, a dedicated Matlab tool, developed within the group of Electrical Engineering participating in the SHiP and SND@LHC Collaborations — and partly improved within this work — is detailed outlining its main advantages as the basis for the magnet design optimization.
- **Chapter 3** outlines the results of magnet design from both traditional and integrated optimized approaches applied to different case studies such as magnets for the SND@LHC and SHiP experiments, with a particular focus on the main criticalities and how they have been accounted for.

Specific contributions from this Ph.D. work are as follows:

- Energy optimization of the magnet designs [50, 51].
- General re-arrangement of the Matlab tool, improvement of cost estimate and integration of detection performance [17].
- Responsability and realization of GEANT4 neutrino interaction simulations in the SND@LHC experiment for physics performance assessment [40, 55, 56, 57].
- Contribution to the design of the air-core, iron-core [15, 16] and compact solutions for the SND@LHC experiment [58].
- Contribution to the formulation of the analytical statistical model and its implementation in case studies [31].

Chapter 1

MAGNETS FOR DETECTORS IN HEP EXPERIMENTS AT CERN

The role of magnets in High Energy Physics experiments is absolutely crucial. Their usage finds application in different fields, ranging from beam deflection to particle identification. As a matter of fact, in most of particle physics experiments, one or more magnets are used to identify particles emerging from interactions: while uncharged particles traverse the magnetic field without being affected, positively charged particles are deflected in one direction and negatively charged particles in the opposite direction, thus providing an initial although simple information about the particles. By "magnets" we almost exclusively mean electro-magnets, although permanent magnets have had applications too.

In case of accelerators, magnets play the main role: dipoles for trajectory curvature of circular orbits, quadrupoles for focusing, fast deflecting magnets for beam injection and extraction. More generally the deflection of the charged particle depends on three parameters: the strength of the field, the length of the trajectory in the field and the momentum of the particle. The size and the strength of the field can be precisely known from proper measurement devices, so by measuring the deflection one can find the momentum. In most cases, magnets are designed such that the magnetic field direction is perpendicular to the trajectories of the particles.

The use of electric and magnetic fields to bend particles' trajectories has become extensive in the last 20th century. Mass spectrometers are the first example of a device using a magnetic field to bend particles' trajectory and provide information about them, such as their mass (or momentum).

The acceleration and the deflection are due to the Lorentz force:

$$\vec{F} = q(\vec{E} + \vec{v} \times \vec{B}) \tag{1.1}$$

acting in the direction of the electric field **E** and orthogonally to the plane containing **v** and **B**. Particles with higher momentum will deflect less than low-speed ones, particles with opposite charge will be deflected in opposite directions and neutral particles will be unaffected. In this way, making use of a magnetic field, the charge and momentum of particles can be identified.

From Eq. (1.1) it can be easily derived that the bending radius R for a charged particle in a magnetic field B can be expressed as:

$$R = \frac{p_T}{qB} \tag{1.2}$$

where $p_T = mv$ is the momentum component transverse to the magnetic field B when considering the equation

$$qvB = mv^2/R \tag{1.3}$$

In the following section, it will be shown more in detail that the momentum resolution of such an apparatus depends on both B and R and so the choice of the magnetic field is often a compromise between the best spatial resolution and the optimum occupancy.

The majority of HEP detectors have been designed with a solenoid coil that provides a uniform magnetic field along the beam axis, but there are examples of dipoles especially when beam-to-target experiments are concerned, as will be discussed in Chap. 3. In the following the most common magnet designs will be presented alongside examples of their usage in the current HEP experiments.

1.1 Solenoids

Solenoids are conceptually simple and very effective magnets since they offer a cylindrically symmetric field, in the same direction of the colliding beams which is very suitable for recent 4π HEP detectors. In this design, only particles with a significant transverse momentum will be deflected, while those projected forward are almost untouched. The extensive use of such a design can be referred to a symmetric 2-D field that facilitates the reconstruction of the events, no material is present within the field volume which could give rise to unwanted secondary interactions, since the inner part of the magnet is fully equipped with detectors.

1.1.1 CMS

CMS is an acronym for Compact Muon Solenoid, it is one of the major experiments at the LHC currently operating at CERN since 2008 [1] It is a general-purpose proton-proton detector designed to run at the highest luminosity ($L > 10^{34}$ cm^2 s^{-1}) at the LHC.

Property	Value	Unit
Nominal (max.) central magnetic flux density	3.8(4)	T
Inductance	14	H
Magnetic stored energy at 4 T	2.6	GJ
Nominal (max.) current	18.4(19.1)	kA
Cold mass weight	220	ton
Stored energy/ unit cold mass	11.8	kJ/kg
Radial thickness of cold mass	312	mm
Magnetic length	12.5	m
Cold bore diameter	6.3	m

Table 1.1: CMS magnet main features

The design has been optimized for the search of the Standard Model Higgs boson over a mass range 80 GeV - 1 TeV but it also allows the detection of a wide range of possible signatures from alternative electro-weak symmetry breaking mechanisms. The most important aspect of the overall detector design is the configuration and parameters of the magnetic field for the measurement of particle momenta, in particular muons. The requirement for a good momentum resolution, keeping a compact spectrometer has naturally led to the choice of a high field and a solenoid magnet. Therefore, the detector features a superconducting solenoid having an inner diameter of 6 m and a magnetic length of 12.5 m, that has been designed to provide a central field of up to 4 T. Its coil has been produced in sections, transported to CERN and assembled on the surface and lowered into place in the underground experimental area [2]. It is constructed with an aluminium stabilised Rutherford Nb-Ti/Cu cable and operates at 4 K with indirect conduction cooling with boiling helium. The cold mass of the complete coil is 220 t.

The magnetic flux is returned via a 1.5 m thick saturated iron yoke that consists of a 6000 t barrel section and two 2000 t removable end caps. This has been designed as a 12-sided structure and a balance has been achieved between outer diameter of the yoke and the size of the muon stations, while trying to maximise the acceptance in azimuth of the inter-layer detectors that are interleaved between the iron plates of the yoke. The main characteristics of the magnet are resumed in Table 1.1 and a schematic of the magnet is shown in Figure 1.1.

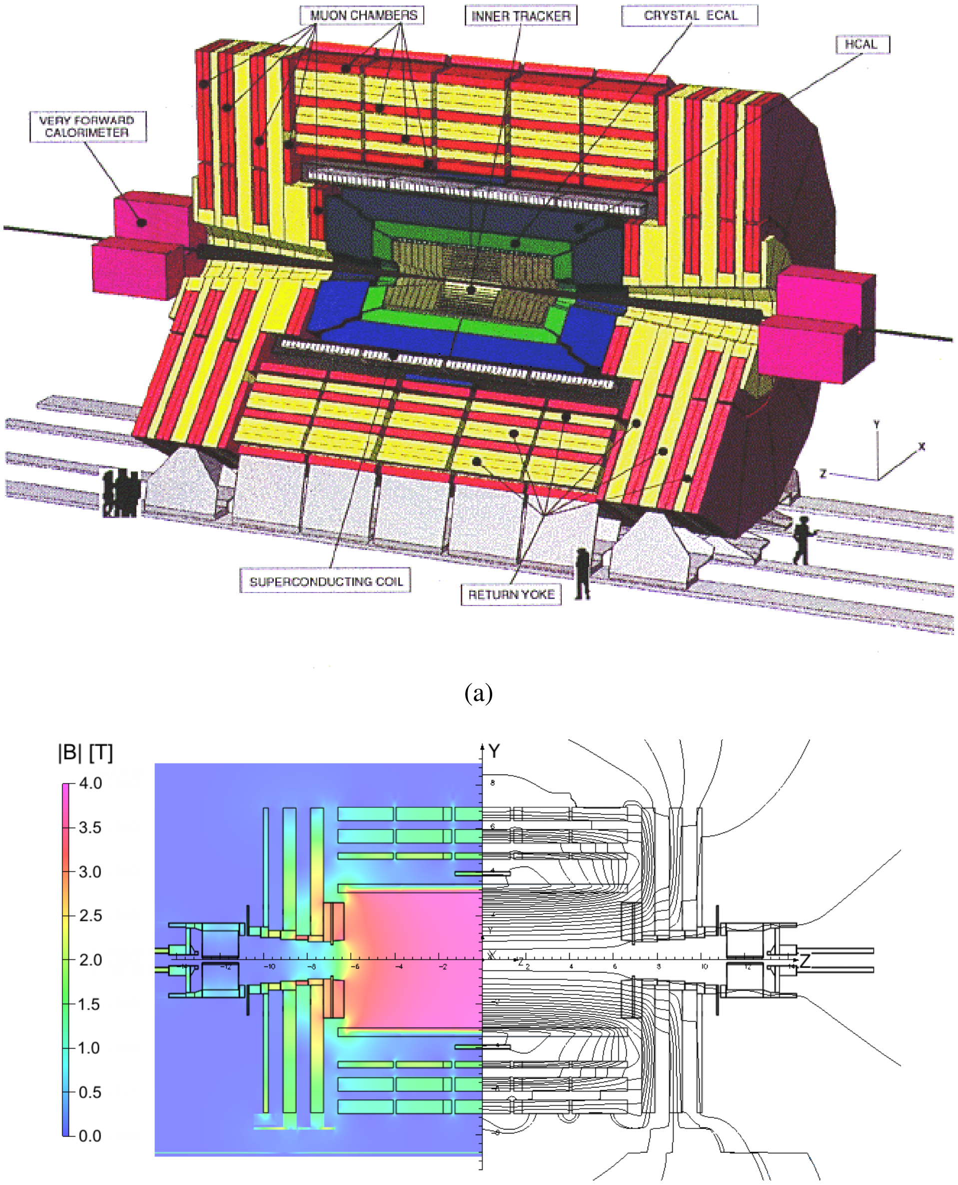

(a)

(b)

Figure 1.1: The CMS magnet system: schematic layout (a) as well as the value of $|B|$ (left) and field lines (right) predicted on a longitudinal section of the CMS detector (b), central magnetic flux density of 3.8 T.

1.1.2 ATLAS

ATLAS (A Toroidal LHC ApparatuS) [3] is a general purpose experiment, together with CMS (1.1.1) and ALICE (1.2.1, 1.1.3) at the LHC built for probing proton-proton collisions and nucleus-nucleus collisions. It presents similar physics goals as the CMS experiment therefore similar requirements on its design: fast, radiation-hard electronic and sensor elements, good charged particle momentum resolution and reconstruction efficiency, large acceptance in terms of azimuthal angle coverage as well as good muon identification and momentum resolution. In this respect the ATLAS detector is nominally forward-backward symmetric with respect to the interaction point, presenting a thin superconducting solenoid surrounding the inner-detector cavity, and three large air-core superconducting toroids, a special case of solenoid magnets.

In particular, the magnet design is optimized with an axial field in the central detector region combined with surrounding azimuthal field supporting the muon spectroscopy. Such a field configuration requires a hybrid magnet system of a solenoid coil making the axial magnetic field (Central Solenoid, CS), and toroidal coils generating the azimuthal magnetic field (Barrel Toroid, BT and two End-Cap Toroids, ECTs). As a matter of fact, the ATLAS magnet system has overall dimensions of 26 m in length and 20 m in diameter, as shown in Figure.1.2. Each of the three toroids consists of eight coils connected in series, with flat pancake type of winding, assembled around the beam axis.

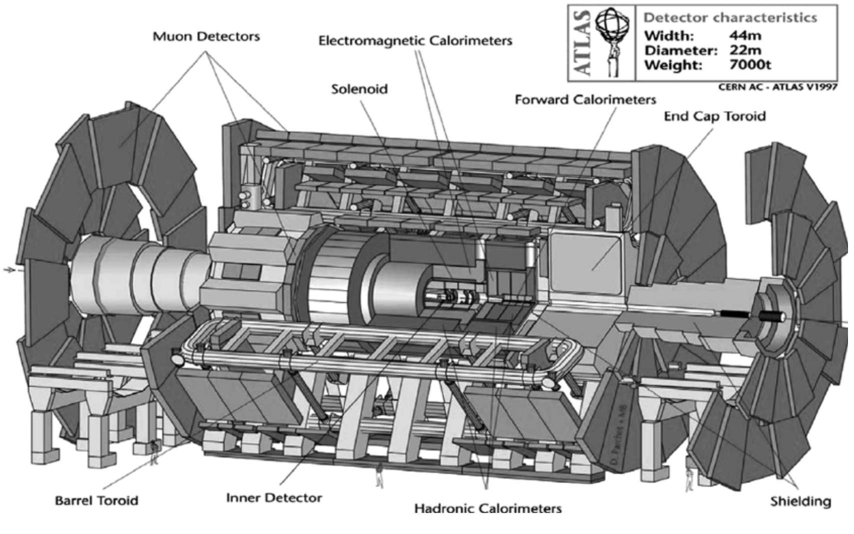

Figure 1.2: The ATLAS experiment layout: the overall dimensions of the sole magnet system are 26 m length and 20 m diameter.

Property	Unit	Barrel Toroid	ECT	CS
Peak magnetic flux density	T	3.9	4.1	2.6
Magnetic stored energy	GJ	1.08	2×0.25	0.04
Nominal current	kA	20.5	20.0	7.6
Cold mass weight	ton	370	2×160	5.4
Axial length	m	25.3	5	5.3
Inner diameter	m	9.4	1.65	2.46
Outer diameter	m	20.1	10.7	2.63

Table 1.2: Main design parameters of the ATLAS magnet system.

The ATLAS-CS magnet provides an axial magnetic field of 2 T in a warm bore of 2.3 m in diameter in the central tracker region with a deflection power of 4.6 Tm, whereas the BT has an inner bore of 9.5 m, outer diameter of 20 m and length of 26 m, it provides a deflection power of 2-6 Tm depending on the angle; on the other hand, the ECTs provide a deflection power of 4-6 Tm at each end. Both barrel and end-cap toroids are to be cooled by using cold pumps to provide forced flow two-phase helium. The main parameters of the magnets are listed in Table 1.2.

1.1.3 ALICE *solenoid*

ALICE (A Large Ion Collider Experiment) [4] is a general purpose, heavy-ion detector at the CERN LHC which focuses on QCD, the strong interactions sector of the Standard Model. It consists of a central barrel part, which measures hadrons, electrons, and photons, and a forward muon spectrometer. The central part covers polar angles from 45° to 135° and is embedded in a large resistive solenoid magnet reused from the L3 experiment at LEP [5]. The solenoid foresees a magnetic length of 12 m and a clear bore diameter of 12 m which produces a weak field. As a matter of fact, the choice of a weak and uniform solenoidal field together with continuous tracking eases the task of pattern recognition. The field strength, as a result of a compromise between momentum resolution, low momentum acceptance and tracking efficiency, is 0.2 T, allowing full tracking and particle identification down to $\sim$ 100 MeV/c in p_T.

1.2 Dipoles

Dipoles, on the other hand, although not adequate for the central part of 4π detectors, are magnets of choice for dedicated "forward" detectors that concentrate the cone of particles travelling in the forward direction, up to $\theta \approx 300$ mrad with θ as the azimuthal angle. In this respect, in order to control the stray field, the geometry of the yoke and coil(s) needs to be studied carefully. The preferred saddle shape for the coils is much easier to achieve with a resistive than with a superconducting coil. A dipole provides a uniform field between its two poles which is excited by a current circulating in the coils. The system follows the right-hand convention, i.e., a current circulating clockwise around the poles produces a magnetic field pointing downwards. The magnetic flux density between these two poles is ideally constant and has only a component in the y-direction (or alternatively x-direction).

1.2.1 ALICE *dipole*

The presence of studies of heavy flavour quark production via the muonic channel in the ALICE physics program has led to the need for a Muon spectrometer, made up of different components, in particular a Muon Dipole Magnet. Muon momenta are indeed determined by a muon tracking system in a magnetic field generated by a warm dipole of 820 t with a nominal field of 0.7 T and a field integral along beam axis $\int |B| dz \sim 3$ Tm. The magnetic field is directed in the horizontal plane perpendicular to the beam direction defining a bending plane and a non-bending plane.

The general concept of the dipole magnet is based on a window frame return yoke, fabricated from low carbon steel sheets.

The flat vertical poles follow the defined acceptance angle of 9° from physics requirements. The coils are of saddle type with coil ends and sides that fit the acceptance angle of 9°. The coils are wound from large hollow aluminium conductor. They are cooled by pressurized demineralized water. The coil ends are located on both sides of the magnet yoke and determine the overall length of the magnet. A schematic of the ALICE Muon Dipole Magnet is shown in Figure 1.3.

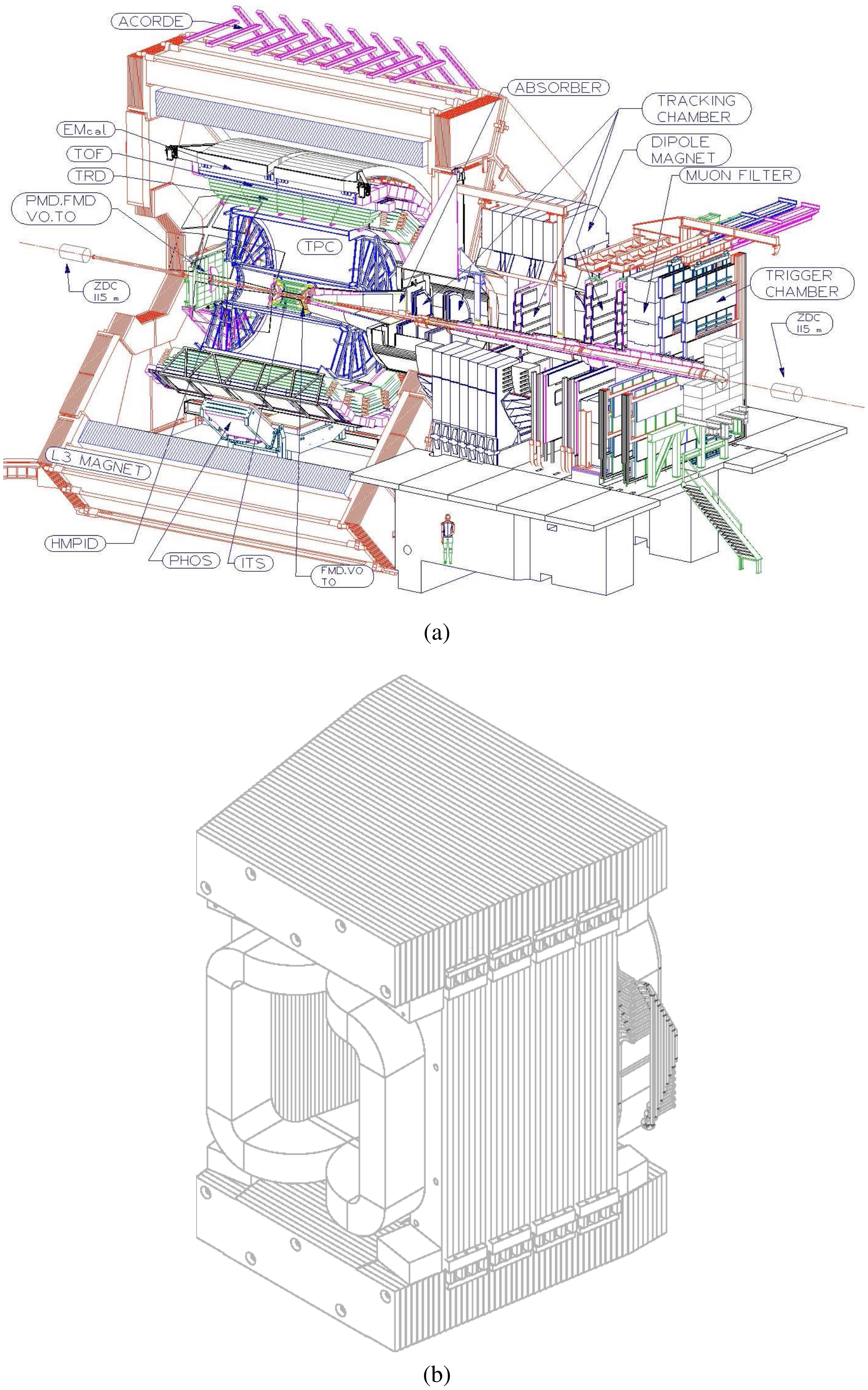

(a)

(b)

Figure 1.3: ALICE experiment layout (a) and schematic of the ALICE Muon Dipole Magnet (b).

Property	Value	Unit
Bending power $\int Bdl$	4	Tm
Magnetic length	10	m
Excitation current NI	2×1.3	MA
Inductance	≈ 2	H
Electric power dissipation	4.2	MW
Stored magnetic energy	≈ 32	MJ
Overall magnet dimensions H×V×L	$11 \times 8 \times 5$	m^3
Weight of yoke	1500	ton
Weight of coils	2×27	ton

Table 1.3: LHCb dipole magnet main features.

1.2.2 LHCb

The LHCb [6] experiment focuses on the observation of evidence for CP violation, exploiting the forward region of the proton-proton collisions at the LHC collider. This leads to a fixed-target-like open structure of the experimental set-up with a large dipole magnet for charged particle separation and momentum measurement. For reasons of cost, simplicity and robustness, a magnet with resistive coils has been chosen, a magnet with super-conducting coils would have required high investment costs and an unacceptably long construction time.The required momentum resolution of about 0.4 % for momenta up to 200 GeV/c demands an integrated field of 4 Tm. The pole gap is 2.2 to 3.5 m vertically (the direction of the field) and 2.6 to 4.2 m horizontally. The two coils are of conical saddle shape and strictly identical. They are mounted mirror-symmetrically to each other in the magnet yoke. The yoke is assembled from identical horizontal bottom and top parts and two mirror-symmetrical vertical parts. It shapes and guides the magnetic flux generated by the two coils in the useful volume required by the detector acceptance. It produces an almost vertical field in a double wedge-shaped gap between the pole faces. The overall length of the magnet (in the beam direction) is 5 m and its total weight is about 1500 t. The power dissipation in the aluminium coils is 4.2 MW. Figure 1.4 shows a perspective view of the magnet including its current and cooling water circuits and Table 1.3 reports its main parameters.

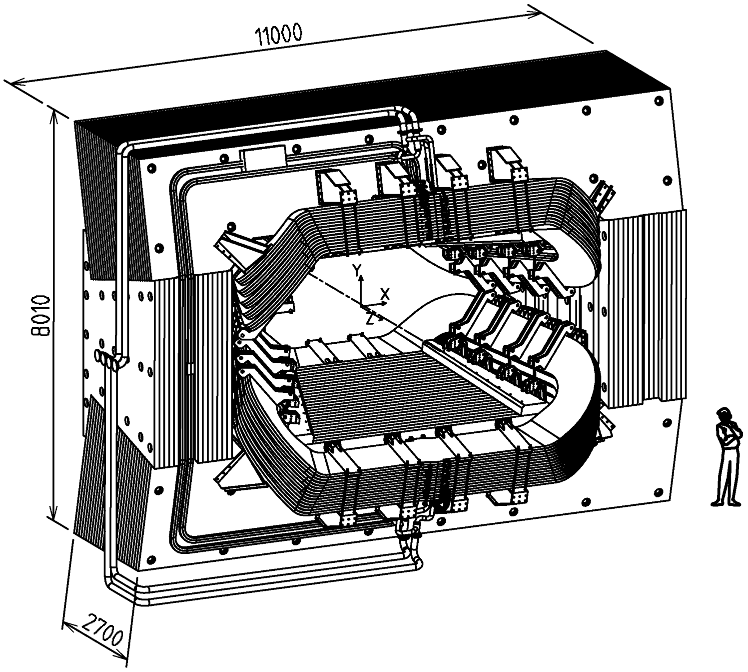

Figure 1.4: Perspective view of the LHCb dipole magnet (units in mm).

1.3 Elements of classical design of warm magnets

The design of warm magnets refers to (electro-) magnets that operate at ambient temperature primarily using a normal-conducting coil. These magnets are categorized as resistive, often using a soft steel return yoke to enhance magnetic efficiency. Designs typically focus on optimising the yoke's shape and the current density of the coils for better performance and efficiency [7].

The magnet design process is rather complex and can be divided into distinct steps that are typically followed sequentially, although feedback loops may occur at certain stages. At the start of each project, requirements, constraints, and boundaries are established. From this, normally an analytical design is developed, followed by a basic numerical design. After each phase such as electrical design, mechanical design, integration assessment, and cost estimation, revisions to the analytical design may be needed. Once these steps are successfully completed, an advanced numerical design — possibly multi-physics — with accurate field evaluation is established [8]. It is essential to keep in mind that a detector magnet in a HEP beam line is not a stand-alone device, it has various interactions with other devices — such as detectors — and services — like cooling plant, power supply, transport and integration as well as safety.

These aspects have to be fully considered in the design phase and the magnet designer calls on his experience to ensure that nothing is forgotten.

Some of them as power supply and cooling are obvious and therefore always taken into account from the beginning whereas others like integration and transportation, tend to be addressed later in the project. Maintaining clear and consistent communication with all relevant partners from the start, along with a well-defined interface strategy, can help mitigate potential issues.

Typical design process

The first step is to define the magnet type (dipole, quadrupole, solenoid, etc.) and its primary purpose. It is also crucial to determine where the magnet will be installed. To begin the initial design process, the magnet designer needs to be provided with the basic constraints, which are usually dictated by physics requirements, expected performance, available space, unwanted interactions, budget and specific requirements. A typical list of parameters and attributes follows

- Physics performance: geometrical acceptance, particle momentum resolution and detection efficiency.
- Space: return yoke and coil dimensions, overall magnet length, active area dimensions, and special shape requirements.
- Magnetised volume: reference magnetic field in the active region, air or iron magnetised region.
- Operation mode: continuous (DC) operation, pulsed mode and ramp rates.

A key consideration for the mechanical layout, which is closely tied to the magnetic design, is identifying any geometric boundaries or constraints. These could include limited space and shape in the experimental area, as well as weight limitations of the supporting structure, and transport restrictions such as the maximum load capacity of an existing crane. Additionally, the accessibility of the installed magnet is critical. The magnet designer must not only ensure that the magnet can be transported to its designated position but also provide unrestricted access to the reference points, enabling the survey team to accurately align the magnet in its final position.

When it comes to interfaces, these refer to how the magnet interacts with other systems such as power supplies and cooling infrastructure. The interfaces with the following equipment should be clearly defined:

- **Power supplies**: maximum current, maximum/minimum voltage, operation mode, stability and reproducibility requirements, maximum current ramp rates.
- **Cooling system**: available cooling capacity, maximum flow rate, maximum pressure difference, water quality, conductor type (aluminium or copper), water inlet temperature, pancake configuration and temperature stability.

Additionally, environmental factors must be considered in the magnet design process. It's important to remember that these interactions can be two-way: the magnet may affect its environment, and the environment can impact the magnet. For example, high ambient temperatures can raise the dew point, leading to condensation on water-cooled coils. Conversely, the heat emitted by the magnet may be substantial enough to overwhelm the ventilation system, causing an increase in temperature within the experimental area. Moreover, the stray field generated by the magnet may interfere with the surrounding devices.

Furtherly, in the context of High Energy Physics (HEP) magnets, ionizing radiation poses a concern. Magnets operating in high-radiation zones require specialized designs that allow for quick repairs or replacements, minimizing human intervention. This also necessitates the use of radiation-hard materials and components. Furthermore, magnetic fringe fields from the magnets can interfere with nearby equipment, such as sensitive particle detectors, while surrounding equipment made of magnetic materials can divert part of the magnetic flux, causing local perturbations in the field quality. Table 1.4 summarizes the aspects to be considered in the magnets design process.

Basic requirements	Magnet type and purpose Operation mode
Performance requirements	Momentum resolution Detection efficiency Magnet aperture
Space requirements	Geometric boundaries Accessibility
Interfaces	Power supply Cooling
Environmental aspects	Temperature Ionizing radiation Electromagnetic compatibility and admitted stray field

Table 1.4: Aspects considered in the magnet design.

1.4 Sustainability issues in magnets' design

Nowadays increasing energies are reached at particle accelerators such as the Large Hadron Collider (LHC) and the need for greater precision in experiments requires the magnets to be larger providing stronger fields. For these, the sustainability concern has become somewhat dominant in the particle experiment design and in particular in the design of magnets.

The scarcity of resources and the impact of climate change, driven by the overuse of fossil fuels, are increasingly pressing concerns for humanity. In particular, the total electricity consumption of scientific facilities is becoming more critical as the dependence on fossil fuels decreases, carbon-neutral energy sources are still in development, and a growing portion of energy use shifts from fossil fuels to electric power. As far as the field of HEP is concerned, it is essential to prioritise the implementation of sustainable concepts, especially when planning the next generation of large accelerator-based facilities. The significantly enhanced performance of these proposed facilities, which is translated into higher beam energy and intensity, is expected to be accompanied by a corresponding increase in electricity consumption. In this respect, the effort towards more sustainable designs finds its application in improving the **energy efficiency**.

1.4.1 Energy optimisation

In recent years, a shift in perspective on magnet's optimal design has emerged. Traditional design procedures of warm magnets basically ground on realizing a reference field in a specified region, with a coil balancing capital and operational costs. Nowadays these factors — along with performance — are part of a broader set of parameters' optimization space. Moreover, a special focus on energy efficiency is considered, aiming to minimize power needs besides costs.
Efforts towards energy efficiency find their application in different development areas which can be classified into three different categories: technologies, concepts and general aspects [9].
As for the technologies, energy efficiency has a long-standing history in particle physics accelerator facilities, as the required performance often could only be achieved using highly energy-efficient devices like superconducting magnets.Few examples can be provided of technologies which could further improve energy efficiency: *permanent magnets*, as they don't need electrical power with the positive side effect that no heat is produced; another important development is *efficient cryogenic systems*, allowing to optimise heat removal in cold systems from beam induced energy deposition, furthermore High Temperature Superconductors (HTS) allow to power high-current devices, such as magnets, with no or little losses.

The present Ph.D. work, along with the involved research group one, aims at contributing to offer a fresh point of view of the traditional approach to magnet design by placing a strong emphasis on integrated optimal design and sustainability issues. In particular, the quite frequent case of limited room for the magnet — and, in turn, for the coil — at expected detection performance is explored, with the goal of minimizing power and occupancy.

1.4.2 Dry superconducting options

It is well-known that iron-dominated magnets are constrained by iron saturation, which limits their magnetic flux density to below 1.8–2.0 T. For applications requiring a magnetic field across a large gap or volume, the use of normal-conducting coils results in bulky designs and demands considerable electric power, often in the megawatt (MW) range. This can lead to substantial operating costs, depending on the magnet's duty cycle.

The recent surge in energy prices, coupled with the growing need for sustainability in research infrastructures, has made superconducting coils in iron-dominated magnets an appealing option for energy saving. Two strategies can be employed in these designs: one involves replacing the resistive coil with a superconducting one while keeping the existing iron yoke, and the other involves a complete redesign of the magnet to fully leverage the capabilities of superconductors, though this may lead to higher overall magnet costs. If the gap between the superconducting coil and the iron yoke becomes too large due to the mechanical frame or cryogenic system requirements, the second approach may be required.

The complete absence of electrical resistivity for the passage of direct current below a certain critical temperature (usually designated with the symbol T_c) is the basic premise of superconductivity, very low temperatures ($4 \div 20$ K) have to be attained, making essential the role of cryogenics [10].It must be noted that the cost of using a superconducting coil with cryogenics required to reach the desirable temperature of operation may overcome the one of a water- or air-cooled warm magnet operating at higher temperatures achieving similar performance goals, therefore an accurate balancing of performance, costs and power should be carried out. Nevertheless, in the past decade, new opportunities have arisen with the development of superconductors that can be operated at intermediate temperatures and do not require liquid helium cooling, a scarce resource today whose losses are required to be minimised. Until around 1990, all superconducting magnets were "wet", meaning they were cooled by liquid helium. The discovery of HTS, combined with advances in cryocooler technology, led to the development of "dry" (cryogen-free) magnets cooled by a cryocooler. Dry cryogenic systems are less cumbersome to operate and maintain. Moreover, they can be designed to be less intrusive than their wet counterparts. For most applications, dry magnets are now preferred, provided that the magnet itself generates minimal dissipation, such as AC losses, during its normal operation.

In the context of HEP, magnets for large scale particle detectors and their bus lines require high currents in high magnetic fields at a wide range of operating temperatures. The operating limits of NbTi and Nb_3Sn conductors, Low Temperatures Superconductors (LTS) widely used in such a field, in terms of magnetic field, current density and temperature have led to the development of cables made from HTS. Such materials, such as ReBCO, BSCCO or MgB_2 have greatly broadened the operating spectrum of temperature, current and magnetic field ranges compared to cables using traditional Nb-based low temperature superconductors.

In particular, the use of MgB_2 cable made from round wires, as demonstrated in [11], has enabled high current densities for large-scale applications, such as some of the magnets needed for the recently approved Search For Hidden Particles (SHiP) experiment [12] at CERN, and for that its main characteristics are presented in the following.

The MgB_2 conductor

The discovery of the superconductor MgB_2 in 2001 generated significant excitement in both fundamental and applied research fields. While its critical temperature (T_c) of 39 K is lower than that of high-temperature superconductors (HTS), it is significantly higher than Nb_3Sn, which has a T_c of 18 K. Given that both magnesium and boron are abundant and relatively not expensive, MgB_2 wires, produced through conventional deformation methods, were expected to be competitive for superconducting applications above 4.2 K, particularly in devices cooled by closed-circuit refrigerators or even liquid hydrogen.

Shortly after the discovery of MgB_2 superconductivity, the University of Genova initiated extensive research on its fundamental properties and wire production techniques. The materials commonly used for the matrix in industrial MgB_2 wires include nickel and Monel, with a niobium barrier to prevent diffusion of magnesium into the stabilizing copper or reactions with the nickel matrix. The critical current density (J_c) of multi-filamentary wires shows an almost linear increase with applied uniaxial strain (ε) up to approximately 0.4%, after which degradation sets in. The primary production methods for MgB_2 wires include the *ex-situ*, *in situ*, and Internal Magnesium Diffusion (IMD) techniques. A detailed description of such production methods will not be covered in this manuscript, although it has been resumed in [13].

At the beginning of the development process, conductors were produced in a flat shape, useful if we consider the winding of a magnet with a pancake-like configuration, but in other cases such as solenoids, a wire with a round or square geometry is preferred, as it presents clear advantages concerning the insulating and winding techniques. At present, several different wires with round and square cross-sections have been developed as well as the arrangement with respect to the copper, as seen in Figure 1.5.

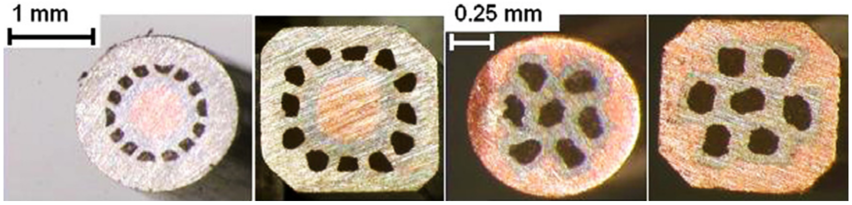

Figure 1.5: Some different geometries of MgB_2 wires with various numbers of filaments and copper configuration.

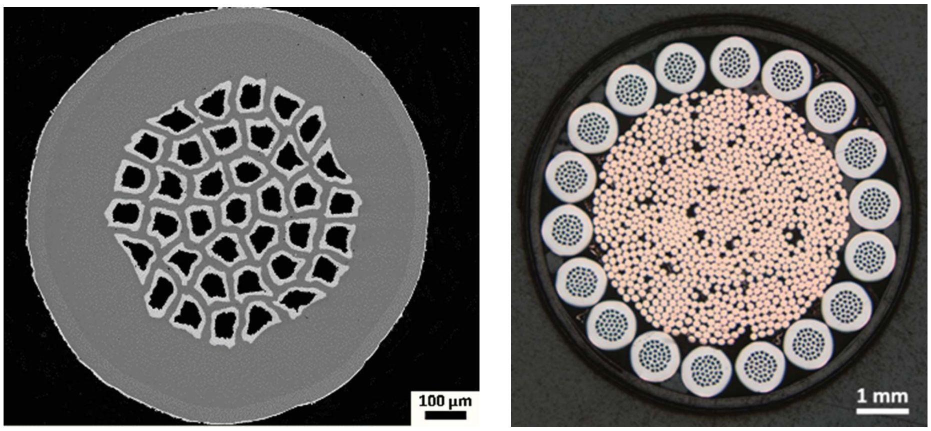

(a) (b)

Figure 1.6: Cross-sectional views of the MgB_2 wire (a) and cable (b) used for superconducting windings.

The MgB_2 type of superconducting wire has been rigorously tested at CERN as part of the high-luminosity upgrade of the LHC [11]. The strands were developed in collaboration between ASG and CERN, with production handled by ASG. The MgB_2 wire has a diameter of 1 mm. The superconducting filaments are embedded within a Monel matrix, which features a thin layer of copper plating on the outer surface, as shown in Figure 1.6 (a).

This copper layer is coated with a tin-silver alloy to ensure the wire's surface quality and provide controlled electrical resistance between wires when assembled into cables. The cable, illustrated in Figure 1.6 (b), has a nominal diameter of 9.4 mm and is made up of eighteen wires twisted around a central stranded copper core with a 4.9 mm diameter. Two layers of tinned copper braids cover the cable, primarily for mechanical stability. In the magnet design and manufacturing process, a minimum bending radius of 300 mm has been established, a value confirmed to cause no degradation. However, the critical bending radius of the wire is 100 mm.

Chapter 2

MODELS AND TOOLS

The design optimization of a magnet or more broadly, a magnetic system for HEP often requires the integration of both physical and engineering analyses. The physical design determines factors such as detection performance, which involves setting the magnet length, magnetic field, and detector positions. In contrast, the engineering design focuses on aspects like power consumption and construction costs, yielding key parameters such as coil thickness, iron yoke thickness, and magnetomotive force. Both analyses rely on basic analytical laws and numerical tools, with Monte Carlo simulations used to assess physics performance and Finite Element Method (FEM) or Boundary Element Method (BEM) analyses employed to evaluate magneto-static fields, temperature, and mechanical and thermo-mechanical stress in the magnet.

However, the numerical tools do not allow for direct coupling between the two analyses in a straightforward way, and optimization processes are generally time-consuming. Analytical models are essential for achieving a coupled analysis that considers both physical and engineering requirements simultaneously, as well as for streamlining the optimization process. Besides the contributions to the design of a number of options for SND detectors in SHiP and SND@LHC experiments, this Ph.D. work describes a mathematical framework for an integrated design of electromagnets for detectors, with emphasis on analytical and semi-analytical models, as the synthesis of the effort in the direction of new emerging perspectives in optimal design of magnets for HEP [14, 15, 16].

2.1 Basic analytical tools

Analytical tools are essential in the early phases of magnet design, and it is quite common to use them for conceptual design. This approach enables the derivation of key characteristics and parameters of the future magnet with reasonable accuracy, providing a solid starting point for numerical design work and simulation validation, ultimately reducing the number of design iterations. Moreover, an analytical approach is essential as it will be shown in the following.

As already mentioned in Sec. 1.3, a magnet is made of different components, for instance a typical design of a warm magnet includes: the magnetic circuit, the excitation coils, cooling circuits, sensors, electrical and hydraulic connections and supports.

Without loss of generality, we can define analytical formulae for a particular type of detector magnets, i.e. **spectrometer magnets**, whose aim is to contribute to the momentum measurement of the particle beam traversing it, discussed in Sec. 2.1.3. The first step is to derive the geometry of the magnetic circuit or magnet yoke. This means translating the physics requirements into a magnetic design defining the yoke characteristics such as the magnetic induction, the aperture size and the magnet excitation (*ampere-turns*). A good starting point to define the necessary magnetic induction is to take into account the *bending power* that the magnet must offer in order to achieve the desirable detection performance, defined as the particle momentum resolution which quantifies the spectrometer's ability to distinguish between close but distinct values of the momentum of particles. It can be expressed as a function of the bending power, in particular, greater bending powers lead to better momentum resolution:

$$\frac{\Delta p}{p} \propto \frac{1}{B\ell} \tag{2.1}$$

where ℓ is the magnetic length of the magnet, as will be discussed in the following and B is the reference magnetic field. As lower momentum resolution leads to better physics performance, a more detailed discussion will be presented in Sec. 2.1.3. Under certain assumptions, asking for a desirable particle momentum resolution constrains the spectrometer's bending power without imposing restrictions on the magnetic field induction or the magnetic length. This allows them to serve as parameters within the optimization framework.

The aperture size of a magnet is mainly defined by the central region around the theoretical beam trajectory, called the "good field region". This region determines where the field quality must stay within certain tolerances. The good field region can be circular, rectangular, or elliptical, depending on the maximum beam size and other functional features. Figure 2.1 shows a typical magnet dipole aperture.

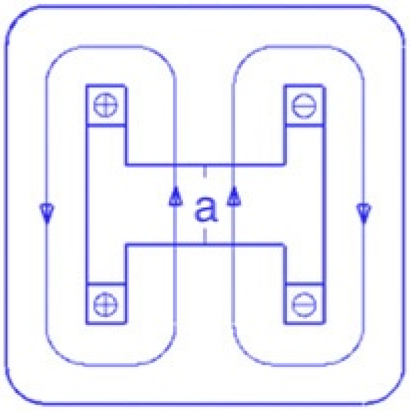

Figure 2.1: Typical dipole magnet aperture alongside the closed integration path.

2.1.1 Field formulae

This section will provide expressions for the main electromagnetic features on the magnet design through an approximate analytical magnetic model, based on magnetic reluctance — with reference to [14] — in the magneto-static formulation.

Knowing the aperture of the magnet we can calculate the excitation current in the coils required to drive the desired field strength. In this respect, we can use the Ampere's law

$$\oint \vec{H} \cdot \vec{dl} = NI \tag{2.2}$$

as well as the relationship between magnetic induction and magnetic field

$$\vec{B} = \mu \vec{H} \tag{2.3}$$

and the definition of magnetic permeability

$$\mu = \mu_0 \mu_r$$

to have the following expression of the ampere-turns (MMF):

$$NI = \oint \frac{\vec{B}}{\mu} \cdot \vec{dl} = \int_{\text{gap}} \frac{\vec{B}}{\mu_{\text{air}}} \cdot \vec{dl} + \int_{\text{yoke}} \frac{\vec{B}}{\mu_{\text{iron}}} \cdot \vec{dl} = \frac{Ba}{\mu_{\text{air}}} + \frac{B_{\text{iron}}\, l}{\mu_{\text{iron}}} \tag{2.4}$$

The gap height is indicated by a and the mean flux path in the iron circuit by l, the last term of the expression $\frac{l}{\mu_{\text{iron}}}$ is called "normalized reluctance" of the yoke.
The choice of the integration path is critical as different approximations can yield varying results.

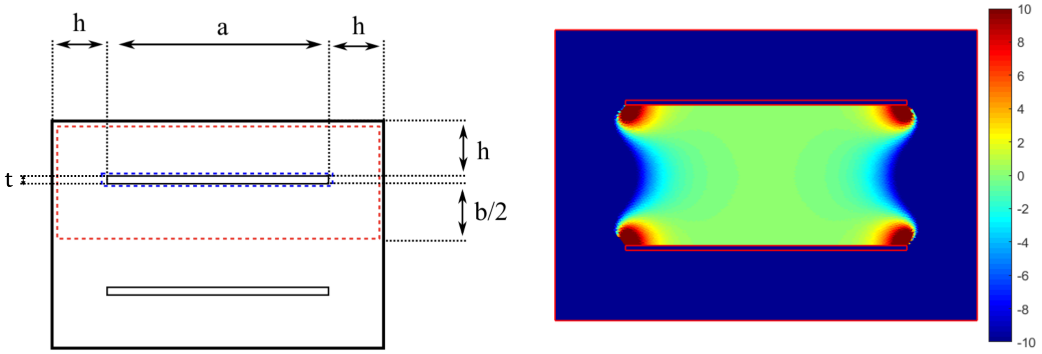

(a) (b)

Figure 2.2: Different integration paths for the evaluation of the magneto-motive force (a) and field spatial distribution in an iron core magnet from a 2-D simulation (b).

Referring to Figure 2.2 (a), two integration paths lead to different expressions of l:

$$l = 2a + 2t \qquad \text{Blue path} \tag{2.5}$$

$$l = 2a + 2t + 6h + b \qquad \text{Red path} \tag{2.6}$$

where t is the overall coil thickness. A comparison with 2D simulations shows that the red path offers a more pessimistic approximation, while the blue path is more optimistic. Additionally, Figure 2.2 (b) illustrates the relative variation of the magnetic flux density along the x-direction, showing a field fluctuation of approximately ±10 %, especially for iron-core magnets. As a result, the integration path closer to the coil leads to a more conservative solution [14, 17].

In analogy to Ohm's law, Hopkinson's law defines the "resistance" in a magnetic circuit — the *reluctance* — as

$$R = \frac{NI}{\Phi} = \frac{l}{A\mu_r\mu_0} \tag{2.7}$$

with Φ indicating the magnetic flux in Wb, l the flux path length in the iron part in meters (m) and A the iron cross-section perpendicular to the flux in square meters (m^2). In this respect, an expression for magnetic efficiency can be defined for air-core magnets as:

$$\eta = \frac{R_{\text{gap}}}{R_{\text{gap}} + R_{\text{yoke}}} \tag{2.8}$$

which is usually kept above 95%. This quantity, and thus the reluctance itself as can be seen in (2.7), is strictly related to the magnetic permeability defined earlier in this Section.

The relative permeability μ_r, in particular, characterises the magnetic behaviour of materials, and it is strictly related to the concept of non-linear — possibly hysteretic — $B - H$ characteristic with **saturation**. In particular, for the construction of electromagnets, materials with high relative permeability are crucial as they are mainly involved in the construction of **yokes**. A discussion about yoke materials and their modelling will be presented in Sec. 2.1.2.

Magnetic length and flux

Another important concept that needs to be defined in magnet design is the **magnetic length**, as referenced in Eq. (2.1). To better understand this, imagine approaching the magnet with a measurement probe along the beam axis, starting from a distant point and moving towards the centre of the magnet: as you approach the edge of the iron yoke, the instrument will show a gradual increase in the magnetic field, as the probe passes through the magnet's stray field. The field continues to rise even after entering the magnet's aperture, reaching its peak near the centre of the magnet, where it stabilizes until the probe is moved away from the centre toward the opposite end of the magnet. Figure 2.3 illustrates how the field increases steadily, rather than abruptly, as the probe approaches the edge of the iron yoke. If the magnetic field is integrated along the longitudinal axis from a point far outside one end of the magnet to a point far outside the other end, the resulting value will be greater than simply multiplying the local magnetic field by the physical length of the iron. At this stage, the magnetic length can be defined as:

$$\ell_{\text{mag}} = \frac{\int_{-\infty}^{+\infty} B(z) \cdot dz}{B_0} \tag{2.9}$$

Thus, to calculate exactly the magnetic length analytically can be quite difficult. Usually, it is derived from numerical computations by integrating the field along the magnet as described above and dividing it by B_0, the local field in the centre of the magnet. Nevertheless, the expression can be approximated providing a certain value of precision, approximated expressions will be provided in further Sections.

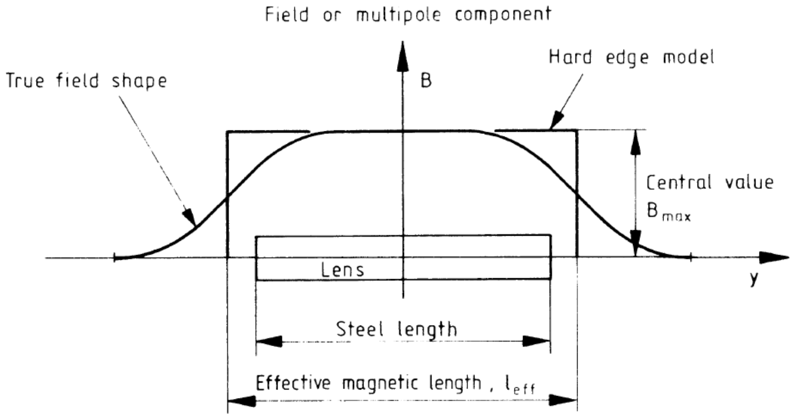

Figure 2.3: Shape of the magnetic field in the longitudinal dimension (named as y) for an air-core magnet.

In the context of such an approximate model, the magnetic circuit can be modelled as a set of magnetic flux tubes defined as

$$\Phi_i = \int_{S_i} \vec{B} \cdot \hat{n} dS \tag{2.10}$$

for which the conservation of flux holds

$$\sum_{i=1}^{N} \Phi_i = 0 \tag{2.11}$$

By neglecting the stray flux, which is a reasonable assumption for a well-designed yoke, the flux is balanced when the internal flux Φ_{int}, that is the sum of the fluxes corresponding to the gap and the coil, is equal to the flux into the yoke Φ_{yoke}, so that:

$$\Phi_{\text{int}} = \Phi_{\text{yoke}} \tag{2.12}$$

Coil and yoke design

In the following, the design of magnet coils and yokes will be discussed. The coil design is not entirely independent of the yoke layout, as optimizing the coils, for example, to minimize power consumption often comes at the cost of a larger yoke cross-section. The magnet designer's task is to strike the right balance between an efficient coil design and an effective yoke design. A high-quality coil design combines low electrical power consumption, adequate cooling performance, appropriate insulation thickness, and reasonable material and manufacturing costs.

(a) Bedstead type coil. (b) Racetrack type coil.

Figure 2.4: Standard coil types for warm magnets in HEP experiments.

Achieving this balance and ensuring optimal magnet performance usually requires multiple design iterations.

The coil design sequence involves the selection of an adequate coil type, to compute the required power, to choose the proper cooling circuit configuration and to select the conductor dimensions.

Coil types can differ depending on the application, Figure 2.4 shows the most commonly used types for normal-conducting magnets. As far as racetrack coils are concerned, they are relatively easy to manufacture and therefore the least expensive, whereas bedstead or saddle coils are often more expensive as they are more complicated to wind and require a complex impregnation mould. To facilitate production and installation, coils are often manufactured in **pancakes**.

On the other hand, regarding the design of the yoke of a dipole magnet for a HEP experiment, the so-called O- or window frame family of yoke layout is preferred, although different ones exist for different purposes such as particle accelerators and beam transfer lines, as discussed in [8]. However, for any yoke design, the choice for one or the other option is led by constraints and requirements such as the purpose of the magnet, the available space, and the required performance. The window frame yoke layout offers a good mechanical stability and a very homogenous field quality. Figure 2.5 shows two basic versions of this magnet type which employ different coil designs. The left-hand image (a) represents the classical window-frame magnet whereas the version on the right-hand side (b) is the O-frame layout. Both may involve racetrack coils installed around the vertical legs of the return yoke. The latter is less efficient in terms of excitation, as it requires more ampere-turns. Moreover, it produces a significant amount of stray magnetic field in the surrounding area.

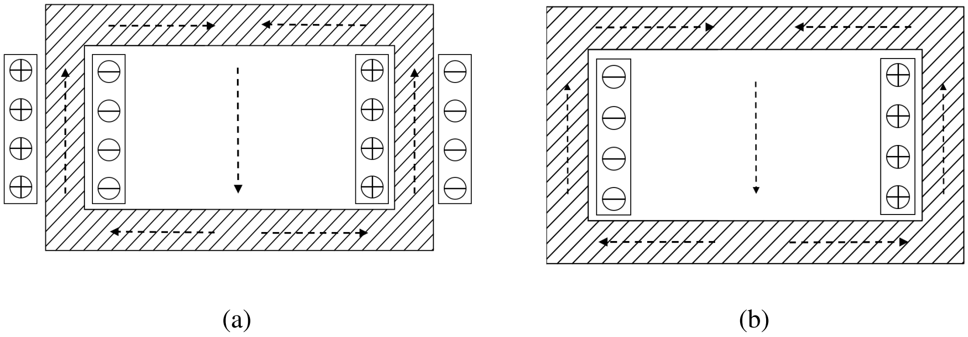
(a) (b)

Figure 2.5: Typical window-frame (a) or O-frame (b) layout for yokes of dipole magnets.

Power and current density

Once the coil type has been selected, the next step is to determine the **power requirements**. For this, we assume that the magnet cross-section and the yoke length are known. The total dissipated power for an individual magnet can be calculated as follows for dipole magnets:

$$P = \rho \cdot J^2 \cdot V_{\mathrm{Cu}} = \rho \frac{Ba}{\eta \mu_0} J l_{\mathrm{t}} \tag{2.13}$$

where ρ is the resistivity in Ωm, V_{Cu} is the volume of the coil, $l_{\mathrm{t}} \approx 2(b + c)$ is the average turn length in m — with b and c height and longitudinal length of the active region, respectively — and J is the current density in A/m^2, defined as:

$$J = \frac{B}{\eta \mu_0 f t} \tag{2.14}$$

with t representing the overall coil thickness, and $f = \frac{\sum_i a_i}{A}$, the geometric filling factor, which is the ratio between the net conductor area and the coil cross-section, accounting for insulation material, cooling ducts, and conductor edge rounding, Figure 2.6 shows visually the quantities just mentioned. Voltage and current can be determined using the power from Eq. (2.13), with $P = VI$. Additionally, the following basic relationships hold:

$$R \propto N^2 J \qquad V \propto NJ \qquad P \propto J^2$$

These relations can be used to improve the efficiency of power converters.

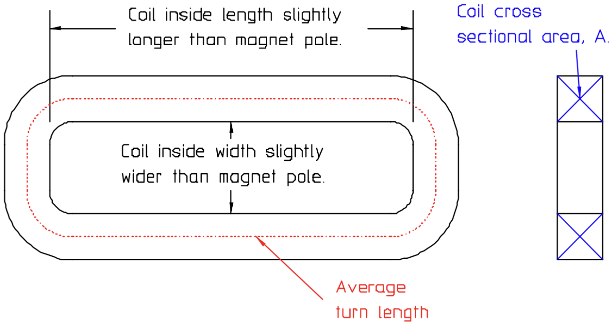

Figure 2.6: Schematic of a pancake coil.

A large number of turns implies low current but high voltage, requiring thicker insulation for both coils and cables, which in turn leads to a lower filling factor. Therefore, coils with many turns are typically chosen for magnets with moderate magnetic field strengths that are powered individually.

Conversely, a small number of turns implies high current but low voltage. This choice requires larger terminals and a larger conductor cross-section but offers advantages such as a better conductor filling factor in the coils, smaller coil cross-sections, and less stringent insulation requirements for the coils and cables.

Additionally, in order to size power converters, we must determine the maximum current, the RMS current, the DC power consumption, and the voltage that the converter needs to provide. The total required voltage depends on the maximum current needed to excite the coils, the coils' resistance and inductance, and the foreseen speed for achieving the maximum field. The voltage on a ramped magnet can be expressed as:

$$V_{\text{tot}} = RI + L\frac{dI}{dt} \tag{2.15}$$

where R is the total electrical resistance of the excitation coils in Ω, L is the inductance of the magnet in H and dI/dt is the maximum ramp rate in A/s. The coil resistance can be easily calculated taking into account the conductor length l, the effective cross-section $a = fA$ and the resistivity ρ of the conductor material:

$$R = \frac{l\rho}{a} \tag{2.16}$$

The inductance L is a quantity not easy to compute, it depends on the number of turns and the geometry of the coils as well as of the yoke surrounding the coils.

The alternative is to compute it via the stored energy U in the magnet for which the current relation holds:

$$L = \frac{2U}{I^2} \tag{2.17}$$

The stored energy depends on the non-uniform field distribution in the gap, coils and iron yoke and it is usually determined by numerical computation. However, in the case of window-framed magnets with a constant field in the gap, the stored energy can be estimated as follows:

$$U_{\text{gap}} = \frac{B^2}{2\mu_0} V_{\text{gap}} \qquad U_{\text{coil}} = \frac{B^2}{6\mu_0} V_{\text{coil}} \qquad U_{\text{yoke}} = \frac{B^2}{2\mu_r \mu_0} V_{\text{yoke}} \tag{2.18}$$

where V_{gap}, V_{coil} and V_{yoke} are the volumes of the gap, coil and yoke respectively in m^3. Therefore the total stored energy in the magnet can be expressed as:

$$U_{\text{magnet}} = U_{\text{gap}} + 2U_{\text{coil}} + U_{\text{yoke}} \tag{2.19}$$

So that the inductance can be calculated from Eq. (2.17) and used in Eq. (2.15).

Cooling

The electrical power which is dissipated in the coils has to be removed from the magnets otherwise overheating can seriously damage the coil insulation and cause short circuits between the coil conductor and the surrounding equipment which is usually on ground potential. In the field of normal conducting magnets, often reported as warm magnets, we distinguish between two different cooling techniques:

- **Air cooling** (or *dry cooling*): this kind of cooling is suitable only for low current densities. As a rule of thumb, the maximum current density for voluminous coils which are almost entirely enclosed in the magnet yoke should not exceed 1 A/mm^2 [8, 18]. For small, thin coils, current density can be higher, but below 2 A/mm^2. A precise thermal study of air-cooled magnets by analytic means is not straightforward, combinations of convection, radiation and heat conduction come into place and they all depend on coil geometry, coil surface as well as thermal contact with the surrounding materials. However, cooling performances of air-cooled coils can be improved by equipping them with appropriate heat sinks with enlarged radiation surfaces as well as cooling fans providing forced airflow.

- **Water cooling** (also known as *wet cooling*) is employed when current densities exceed the limits of air cooling. The use of demineralized water from a cooling plant can safely support current densities up to 10 $\mathrm{A/mm^2}$, providing a reliable solution and allowing for a more compact coil design. While it is possible to achieve current densities as high as 80 $\mathrm{A/mm^2}$ for specific applications, this is not advisable for standard magnets, as it significantly reduces the reliability and lifespan of the coils. Higher current densities require a more complex cooling system, often involving multiple parallel circuits per coil and high coolant velocities, which increase the risk of erosion.

As for the manufacturing of either dry or wet-cooled conductors, both can be made of round, rectangular, or square wires. They are commercially available in various grades and dimensions. The water-cooled ones are provided with a central duct for demineralized water as shown in Figure 2.7. The inter-turn and ground insulation is provided by one or more layers of half-lapped glass fibre tape impregnated in epoxy resin. Inter-turn thickness is normally between 0.3 mm and 1.0 mm whereas the ground insulation thickness should be between 0.5 mm and 3.0 mm depending on the applied voltage [8].

Whereas, as far as water cooling modelling is concerned, we know that to increase the temperature of 1 kg of water by 1 °C we need 1 kcal=1/4.186 kJ, this means that a water flow of 1 litre/s can draw 1/4.186 kW by increasing its temperature by 1 °C.

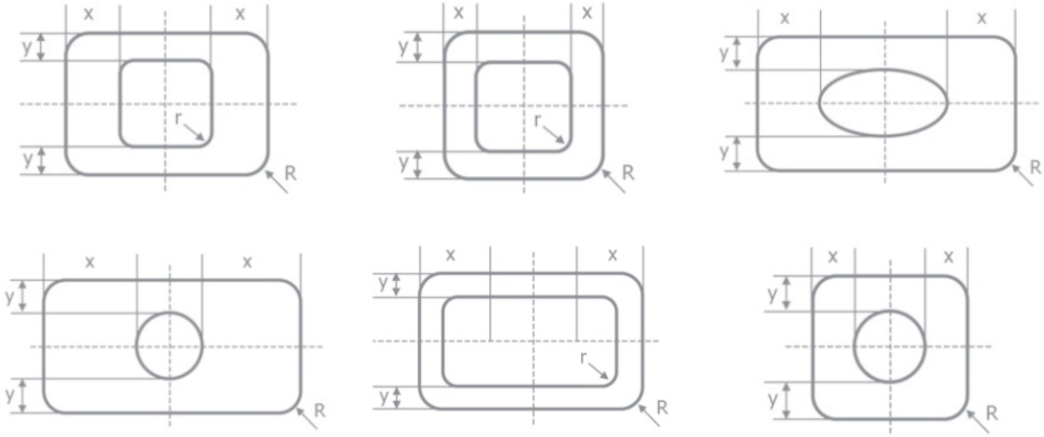

Figure 2.7: Hollow conductor cross-sections for water-cooled coils.

Therefore the following relation between water flow Q in L/min and power P in kW holds, valid with good approximation in the range between 20 °C and 60 °C:

$$Q = 14.3\frac{P}{\Delta T} \tag{2.20}$$

with ΔT being the increase of temperature of the water. This relation tells us that one can cool about 2 kW with a water flow of 1 litre/min with a temperature increase of 30 °C. For optimal thermal performance, the water flow should exhibit moderate turbulence. This requirement is met when the *Reynolds number*, which represents the ratio of inertial forces and viscous forces, is greater than 2000 but less than 10^5. The Reynolds number is given by the formula:

$$R_e = \frac{dv}{\nu} \tag{2.21}$$

where v is the water velocity, ν is the dynamic viscosity and d the equivalent hydraulic diameter of the cooling pipe. As a rule of thumb water speed should satisfy the relation:

$$v > \frac{1.4}{d}$$

where v is measured in m/s and d in mm.

In order to achieve a good combination of diameter and water velocity the following relation adds as well for a given flow:

$$Q = 0.06\pi\frac{d^2}{4}v$$

keeping in mind to avoid excessive water velocities which can cause erosion corrosion of the cooling pipe, in copper this starts to happen at $v > 3$ m/s [18]. The last parameter to take into account for the cooling modelling is the pressure drop, given by the expression, valid in the same range as Eq. (2.20):

$$\Delta P = 60L\frac{Q^{1.75}}{d^{4.75}} \tag{2.22}$$

for hydraulically smooth pipes of length L (in m) and diameter d (in mm) with inlet and outlet at about the same height, as in magnet coils, with moderately turbulent flow. The pressure drop typically provided by modern cooling plants is between 1 and 10 bar, nevertheless, advanced cooling stations can supply water with a pressure of up to 20 bar. Equation (2.22) comes into place in case a low-pressure drop offered by the cooling plant must be compensated by a higher cooling flow. Table 2.1 summarises criteria and formulae for the determination of cooling circuits.

Parameter	*Expression*
Cooling flow	$Q \sim 14.3\frac{P}{\Delta T}$
Water velocity	$v = \frac{10^3}{15\pi d^2}Q$
Turbulent flow for water at ~40 °C	$R_e \sim 1400dv > 2000$
Water velocity limit	$v < 3\ \mathrm{m\,s^{-1}}$
Pressure drop	$\Delta P \sim 6 \times 10^4 L\frac{q^{1.75}}{d^{4.75}}$

Table 2.1: Criteria and formulae for the determination of water cooling circuits, quantities are expressed in practical units: Q in litre/min, d,L in mm and ΔP in bar.

Cost estimate

Within any project, cost estimate is every time a fundamental feature characterising the magnet's design. In traditional designs, it used to play a somewhat determining role in the coil design [8], but in the context of sustainability concerns, costs are no longer a target function alone but part of a set of parameters within the optimization process. Accurately estimating the cost of a magnet project demands considerable experience and a solid understanding of the market. Although material prices are generally well-established, assessing the manufacturing costs of a magnet is not an exact science and is influenced by numerous factors. Previous experience has demonstrated that the range of bids can differ significantly, sometimes by as much as a factor of three between the lowest and highest offers.

As a matter of fact, one of the main goals in magnet design is the minimum total cost over the magnet's lifetime. Total cost can be divided into **capital** and **operational cost**, the power consumption is important as it enters in both the capital and operational costs. Two cost models have been built to estimate the magnet capital cost. The first is a linear model where the fabrication cost of the magnet is directly proportional to the mass of the coils and the iron. The second model is also linear but includes constant factors representing the cost of tooling and engineering [19]. From Eq. (2.14) it can be easily deduced that the magnet coil mass is inversely proportional to the coil conductor current density J and the yoke mass has a weak inverse dependence on it, since coil and yoke sizes are linked. So that the two models can be expressed as:

$$C_{\mathrm{M}} = A_{\mathrm{coil}} M_{\mathrm{coil}} + B_{\mathrm{yoke}} M_{\mathrm{yoke}} \tag{2.23}$$

$$C_{\mathrm{M}} = \Gamma_{\mathrm{coil}} + A_{\mathrm{coil}} M_{\mathrm{coil}} + \Gamma_{\mathrm{yoke}} + B_{\mathrm{yoke}} M_{\mathrm{yoke}} \tag{2.24}$$

where A_{coil} is the cost function per unit coil mass and B_{yoke} is the cost function per unit yoke mass, which will be iron. The Γ factors are constants encompassing the costs of tooling and engineering that are independent of the current density. The Eqs. (2.23) and (2.24) don't represent the overall expression of the magnet capital cost, the cost of providing the power and the cooling to the coil must be addressed, this part will depend on the magnet power consumption P, which is directly proportional to the current density from Eq. (2.13), therefore the cost equations for the power supply C_{PS} and the magnet cooling system C_{CS} are as follows:

$$C_{\mathrm{PS}} = \Gamma_{\mathrm{PS}} + D_{\mathrm{PS}} P \tag{2.25}$$

$$C_{\mathrm{CS}} = \Gamma_{\mathrm{CS}} + E_{\mathrm{CS}} P \tag{2.26}$$

where Γ_{PS} and Γ_{CS} are the fixed portions of the power supply cost and the cooling system, respectively, i.e. power supply controllers, interfaces with computers and cable cost as well as hoses and piping and water piping system. Whereas D_{PS} and E_{CS} are the proportional parts of the cost which include the cost of the power-delivering unit in the power supply and the piping system, respectively. Finally, the overall capital cost of the magnet can be expressed as the sum of the three types of costs we have identified so far:

$$C_{\mathrm{Cap}} = C_{\mathrm{M}} + C_{\mathrm{PS}} + C_{\mathrm{CS}} \tag{2.27}$$

In view of the cost optimization, the conventional magnet system capital cost is minimum when

$$\frac{dC_{\mathrm{Cap}}}{dJ} = 0$$

As far as the magnet's operating cost is concerned, it includes electric power, the cost of maintenance and the cost of cooling water over the operating life of the magnet. The operating cost over a time t can be calculated as follows:

$$C_{\mathrm{Op}} = \left[P_{\mathrm{M}} \left(\frac{1}{\eta} + \alpha \right) \right] F_{\mathrm{P}}\, t \tag{2.28}$$

where P_{M} is the power in (in kW) used by the magnet, η is the efficiency of the power supply itself plus the cables that carry power to the magnets which usually is $0.85 \div 0.90$ whereas α is the fraction of the magnet power that is needed to provide the cooling, typical values are around $0.1 \div 0.12$.

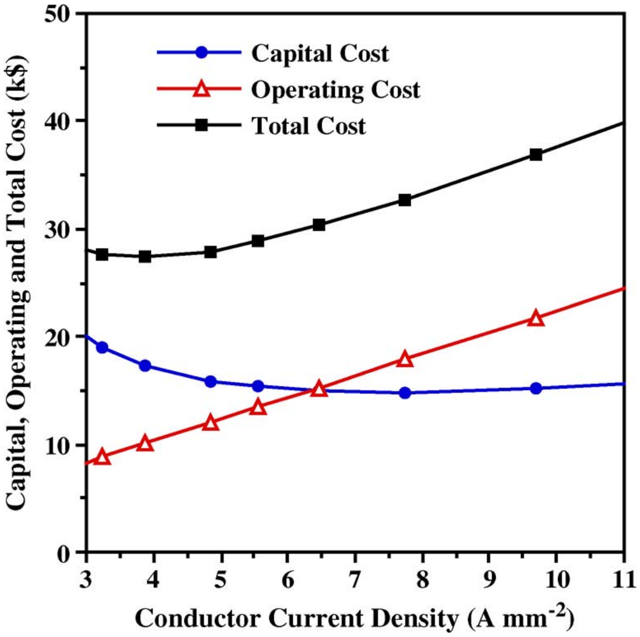

Figure 2.8: Capital cost, operating cost (for 5×10^4 h) and total cost as a function of conductor current density for a dipole magnet at MSU [19].

F_P is the cost of electric power given in currency/kWh and the time t is the operating life for the magnet, given in hours.

The total cost of operating a magnet over its lifetime can be therefore expressed as:

$$C = C_{\mathrm{Cap}} + C_{\mathrm{Op}} \tag{2.29}$$

where expressions for C_{Cap} and C_{Op} are given in Eq. (2.27) and Eq. (2.28), respectively. If we plot the total cost as a function of the current density J, as shown in Figure 2.8, a minimum can be observed representing the optimum current density value for which the total magnet cost is minimized. This is a critical point to be stressed: achieving the optimal current density for which the cost is minimized doesn't necessarily coincide with the aim of the energy-efficient design optimisation. A "rule of thumb" states that conventional water-cooled magnets for which the coil is made of copper should be designed with a current density of 5 A/mm^2[18, 19]. However, as it will be shown in Sec. 3.2.2, a design procedure oriented to sustainability is shifting the cost estimate's optimal point to a different one jointly evaluating multiple target functions.

2.1.2 Iron characteristics and modelling

Magnetic materials are key elements of magnet technology. They should be procured on the basis of careful selection and adapted specifications, since their primary and secondary metallurgy, chemical composition, purity, applied thermal treatments, and microstructure will have a significant influence on their final properties. The modelling of such materials in the context of magnet design can be crucial as it affects several aspects such as the magnetomotive force.
We can distinguish between three main categories of materials:

- diamagnetic materials ($\mu_r < 1$),
- paramagnetic materials ($\mu_r > 1$),
- ferromagnetic materials ($\mu_r >> 1$).

For their extremely favourable typical μ_r values ferromagnetic materials like steel are commonly used for magnetic circuits or yokes. Nevertheless, they exhibit a non-linear relationship between the magnetic field strength H and the flux density B that has to be properly considered for accurate field evaluation. The total flux density within the material is the sum of the flux density in free space, $\mu_0 H$, and the magnetic polarization M (measured in Tesla), expressed by the equation:

$$B = \mu_0 \left(H + M \right) = \mu_r \mu_0 H \tag{2.30}$$

where μ_r is the relative permeability. The magnetic polarization M for specific materials is typically provided through $B - H$ curves.
Furthermore, ferromagnetic materials show what is called *hysteresis*, a phenomenon for which the flux density $B(H)$ as a function of the field strength is different when increasing and decreasing excitation, as shown in Figure 2.9. When the current is switched off, some magnetic polarization of the iron remains: this is called remanent field B_r. The width of the hysteresis curve is determined by the coercive force or *coercivity* H_c, defined as the value of field strength that reduces the magnetic flux density in the iron to zero, although this effect is known to be present in the steel while designing the magnet, in the following it will not be taken into account.
Materials having $H_c < 1000$ A/m are called *soft magnetic* materials, those with $H_c > 1000$ A/m are called *hard magnetic*, e.g. permanent magnets.

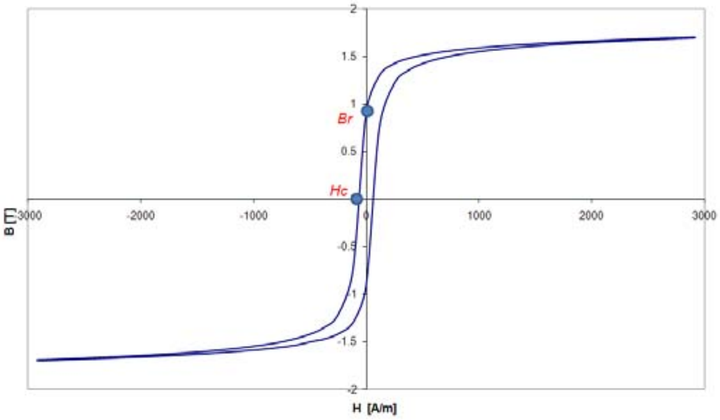

Figure 2.9: Example of a hysteresis curve for a soft magnetic material.

The magnetic properties of steel can vary significantly, influenced by both the chemical impurities present in the iron and its mechanical and thermal treatment. The carbon content plays a dominant role in determining steel's magnetic performance, while other chemical impurities have a lesser but still important impact. As a result, most magnet steel is classified based on its equivalent carbon content. In fact, iron is considered "high purity" when the total impurity concentration (primarily carbon and silicon) does not exceed a few hundred parts per million (ppm).
Otherwise, it is categorized as low-carbon steel or non-alloyed steel.

The 1010 steel grade and saturation

Not all types of steel alloys are suitable for use as iron yoke materials. Most magnets utilize steel alloys with a low carbon content, typically less than 0.1%, for flux return yokes. An example of this kind of steel is referred to as 1010 steel [18] used in HEP magnets, for instance already employed in the ATLAS spectrometer [20]. However, due to the wide range of permissible impurity levels, the composition of low-carbon steel can vary between different manufacturers and production batches, making it difficult to guarantee consistent magnetic properties. In the case of 1010 steel, the silicon content can fluctuate even depending on the specific form of the product [20]. This variation accounts for the significant differences in magnetisation curves observed between different production batches of the same steel grade, as shown in Figure. 2.10.

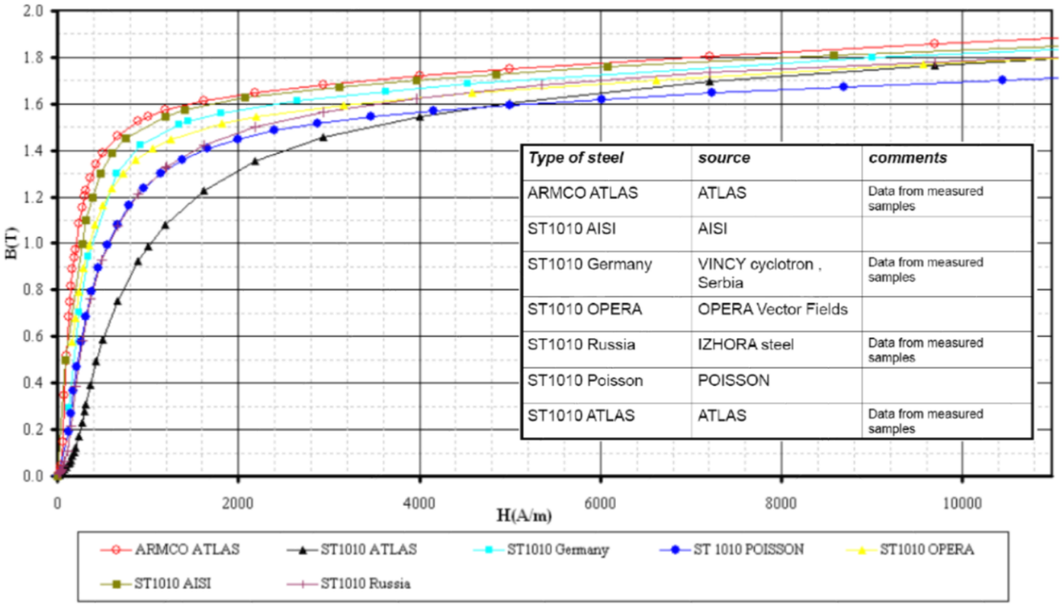

Type of steel	***source***	***comments***
ARMCO ATLAS	ATLAS	Data from measured samples
ST1010 AISI	AISI	
ST1010 Germany	VINCY cyclotron , Serbia	Data from measured samples
ST1010 OPERA	OPERA Vector Fields	
ST1010 Russia	IZHORA steel	Data from measured samples
ST1010 Poisson	POISSON	
ST1010 ATLAS	ATLAS	Data from measured samples

Figure 2.10: Magnetisation curves of different heats of constructional steels used as magnetic steel in different experiments, such as ARMCO and 1010 heats.

In magnet design, it is advisable to select the magnetisation curve that represents the "worst-case scenario" once the steel grade is chosen. This ensures that the design is robust and can accommodate any variability in the magnetic properties of the actual iron used, allowing for improvements if the real material performs better. Secondarily, the coercive field is also a key factor, and for steel alloys used for electromagnets' yokes, it is desirable to have a low coercive field. A common requirement for steel in both accelerator and detector magnets is that the coercive field should be less than 80 A/m. While hysteresis and coercive field are crucial in determining how a material responds to changes in magnetic fields, another key concept to consider in yoke materials is **magnetic saturation**. As the magnetic field strength increases, the magnetic domains within the material align more and more with the external field. However, beyond a certain point, the material reaches a state where almost all of its magnetic domains are fully aligned. At this stage, any further increase in the external magnetic field results in minimal additional magnetization of the material, as shown in Figure 2.10, this happens when $\mu_{\mathrm{r\,diff}} = \frac{1}{\mu_0}\frac{dB}{dH} \longrightarrow 1$. For materials like steel, especially those used in magnets, the saturation point defines the limit of magnetic flux the material can handle. This is particularly important in applications where the magnetic field strength needs to be high and consistent, as operating near or beyond the saturation point can lead to reduced efficiency and increased energy losses.

As a matter of fact this translates into a local decrease of the iron permeability (small μ_{iron}).

It is good practice to keep the iron yoke reluctance smaller than a few per cent of air reluctance by providing a sufficiently large iron-cross section such that the magnetic flux in the iron stays not too high, for instance for the AISI1010 it remains smaller than 1.75 T. If the recommendation

$$\frac{h}{\mu_{\mathrm{iron}}} < 0.01\frac{a}{\mu_0}$$

is followed, the magnetic efficiency is better than 98% [8]. This in practice translates into choosing a working point between the knee and deep saturation on the magnetisation curve, whenever possible, ensuring greater reliability. This helps attenuate any fluctuations in the actual magnetic field.

Grain Oriented steel

Yokes are generally built from massive iron or assembled from laminations (cold-rolled steel). Rolled steel may have different directional magnetic properties. Isotropy can be restored by *annealing* the rolled steel at some temperature high enough to re-grow the crystalline grain structure. In particular, some peculiar iron-silicon steel alloys, such as the oriented steels, provide superior magnetic properties in the rolling direction. They are mainly involved in transformers industry [21] but can be implemented in some magnet designs or in general when the design permits the directional magnetic characteristics to be used efficiently. Grain-oriented silicon iron has been developed by altering the silicon content in the steel, cold rolling the strip to the desired thickness, followed by high-temperature annealing at 1200 °C to evolve secondary re-crystallization. Cold rolled grain-oriented (CRGO) steel is a delicate steel to be handled with care. The magnetic property of the steel with better tensile strength is the most important quality to be required. The sheet of CRGO steel should not be bent dented or damaged during handling as it directly affects the losses and magnetic properties [22]. However, in the context of magnet design, a possible GO steel to be used as a yoke should withstand to bending, and cutting in order to align its magnetic domains to the magnetic field direction as much as possible. Tests have been performed on GO steel, subject to bending in [23] with different bending radii. It can be seen that annealing can partially restore the magnetisation properties to some extent, depending on the bending applied.

2.1.3 Detection statistical tools

In the previous sections, several formulae and procedures for the design of magnets for the HEP have been presented, in particular for dipole magnets, which are typically involved in experiments for the measurement of the particle momentum. Such a type of magnets are called *spectrometers*, as already mentioned.
In the following an analytical approach for momentum estimate of muons with spectrometers is presented, that is aimed at introducing the performance in the design/optimization process **at the same integration level** of other quantities.

Muon spectrometers

Muons are elementary charged particles similar to the electron belonging to the same particle family, the *leptons*, but with a much greater mass, about 200 times the electron one. They are crucial in particle physics for several reasons: although similar to electrons, some key differences make them valuable for probing the fundamental nature of matter and forces. Muons are involved in Standard Model testing, in studies about the Weak Force (through their decay in electrons for instance), in probing deep inside atomic nuclei (Deep Inelastic Scattering) or in high-energy particle collisions like those at CERN, and many other reasons. Due to their greater mass, muons accelerate slower than electrons in electromagnetic fields and emit less bremsstrahlung (deceleration radiation).
This allows muons to be one of the most penetrating particles in the Standard Model because the deceleration of particles like electrons and muons is primarily due to energy loss by the bremsstrahlung mechanism. Such a peculiar feature of muons is exploited by particle physics experiments to gain information on physics processes which muons are originating from (such as *neutrino interactions*) through their momentum estimation with *muon spectrometers*.

In accelerator-based experiments, such as those conducted at CERN, the muon holds a unique role as a long-lived particle that interacts uniquely through electromagnetic forces, making it relatively easy to identify. A muon spectrometer typically includes one or more position-sensitive detectors that record the track of charged particles, which — with a magnetic field — allow the determination of charge and momentum from the curvature of these tracks.

The identification of muons often relies on a large amount of absorber material in front of the muon detector, which allows only muons (and neutrinos) to pass.
Almost all modern general-purpose detectors at colliders use muon spectrometers of multifunctional design with various magnetic field configurations. Muons can be *detected* via their electromagnetic interactions in matter, for instance:

- In modern detectors, often the ionisation of gas molecules (drift chambers) [24] or the creation of electron-hole pairs in semiconductors (silicon detectors) [25] is exploited to recognise the passage of a muon and to measure at the same time space points along the trajectory. Typical resolutions are in the range $10 \div 100$ µm.
- Also chemical processes can be exploited, notably in nuclear emulsions; this technique has been extensively used in past experiments as in OPERA [26] but also in today's experiments as the SND@LHC experiment [27] at CERN and under discussion within the SHiP Collaboration [12]. The nuclear emulsion technology provides a three-dimensional spatial resolution of the order of one µm;

In muon spectrometers, high-resolution tracking detectors are essential, like those mentioned earlier.

Momentum and charge measurement

In the following discussion, only *relativistic* muons will be considered, as they are primarily relevant in high-energy physics (HEP) experiments. Measuring both the momentum and charge of muons simultaneously requires a combination of a magnetic field and a tracking detector.

Within a uniform magnetic field, a particle with a unitary charge (the electron charge) follows a circular path, with the radius given by Eq. (1.2). The direction of the curvature depends on the charge's sign. Since the momentum components parallel to the magnetic field are unaffected, the overall trajectory forms a helix. Eq. (1.2) serves as the basis for all magnetic spectrometers. In the following, only the motion of the particle, whether a muon or anti-muon, in the plane perpendicular to the magnetic field will be considered.

A high-energy muon cannot be "trapped" by the magnetic field; typically, it enters the field, follows a short circular arc with a large bending radius, and exits the field in a slightly different direction.
To determine the transverse momentum of the muon, it is often required:

- A strong large magnet with a well-known field strength;
- Several precise measurements of the particle's position along its trajectory inside and/or outside the magnetic field with tracking detectors.

However, muons — along their trajectory through matter — suffer repeated elastic **Coulomb scatterings** from nuclei. The vast majority of these collisions result, therefore, in a small angular deflection of the muon. These thus follow a random zigzag path as it traverses the material. The cumulative effect on these small angle scatterings is, however, a net deflection from the original particle direction [28] which biases the measurement of the muon momentum, as it will be discussed in the following.

Without loss of generality, two momentum and charge measurement techniques can be identified depending on the magnetic spectrometer layout: bending angle measurement and the sagitta, extensively discussed in elementary particle physics books [29]

Bending angle measurement Four tracking stations are foreseen **outside** of the magnetic spectrometer, as presented in Figure 2.11. The bending angle of a track traversing the magnet can be measured and therefore the momentum (and charge). The bending angle θ is determined by two tracking detectors before the magnet separated by the lever arm a, measuring the track coordinates x_1, x_2 and two tracking detectors behind the magnet, measuring the track coordinates x_3, x_4 also separated by the lever arm a. From the track coordinates the bending angle is obtained

$$\theta = \frac{x_4 - x_3}{a} - \frac{x_2 - x_1}{a} = \frac{qB\ell}{p} \tag{2.31}$$

where ℓ is the length of the magnet (or better its *magnetic length*) and p the transverse momentum of the muon.

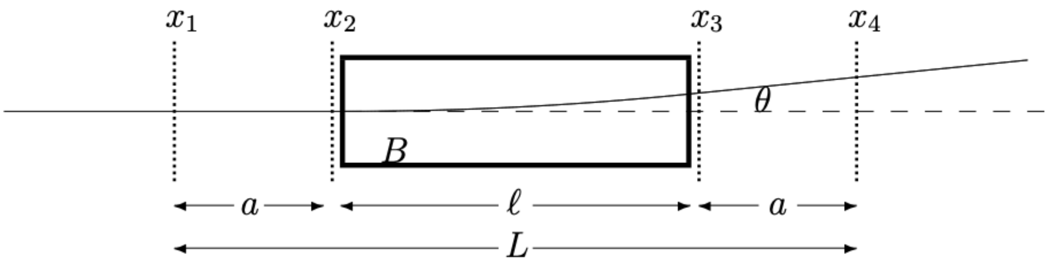

Figure 2.11: Magnetic spectrometer measuring the bending angle of a particle track [30].

Hence the muon momentum resolution in such a configuration can be identified as the resolution on the bending angle measurement, as the following:

$$\frac{\Delta p}{p} \approx \frac{\Delta\theta}{\theta} = \frac{2\varepsilon p}{qB\ell a} \tag{2.32}$$

defining $\Delta\theta = 2\varepsilon/a$ as the error on the measurement of θ and ε as the coordinate measurement error on the tracking stations, namely their spatial resolution.

Sagitta measurement Four (or even three) detectors are foreseen: two of them will record the particle track position **outside** of the magnet and two (or one) will record it **inside** the magnetic field. The layout of a spectrometer measuring the sagitta of a track is shown in Figure 2.12. The sagitta s is determined but two detectors before and behind the magnet, measuring the track coordinates x_1, x_4 and two detectors in the middle of the magnet, measuring the track coordinates x_2, x_3. From the track coordinates the sagitta is obtained

$$s = \frac{x_2 + x_3}{2} - \frac{x_1 + x_4}{2} = \frac{qB\ell^2}{8p} \tag{2.33}$$

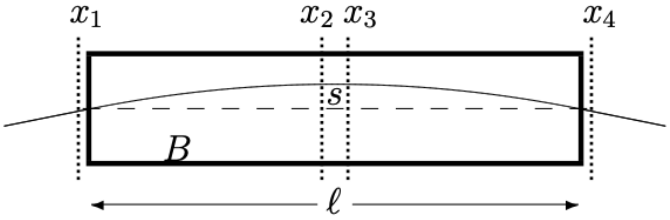

Figure 2.12: Magnetic spectrometer measuring the sagitta of a particle track [30].

Similarly to the bending angle configuration, the muon momentum resolution can be expressed as

$$\frac{\Delta p}{p} \approx \frac{\Delta s}{s} = \frac{8\varepsilon p}{qB\ell^2} \tag{2.34}$$

with $\Delta s = \varepsilon$.

Analytical statistical model

The following discussion takes inspiration from the note at Ref. [31]. Let us consider a detector layout made up of mainly three sub-detectors: a target, from which particles of interest are generated and two magnetised regions, one made of alternating passive material (as iron) and detectors, also referred to as "calorimeter" and the other one made of an iron bulk, instrumented with proper tracking stations placed on both sides of each magnet, as depicted in Figure 2.13.
Each particle's trajectory is defined by a set of random variables and can be represented as an event within a sample space. Specifically, we have

$$\Omega \rightarrow \left\{ \underbrace{p, X_0, S_0, \Theta_0,}_{\text{Particle Initial State}} \; \underbrace{\Delta_1, \Delta_2, \Delta_3, \Delta_4,}_{\text{Measurement Errors}} \; \underbrace{\Theta_{\sigma 01},\ S_{\sigma 01},\ \Theta_{\sigma 12},\ S_{\sigma 12},\ \Theta_{\sigma 34},\ S_{\sigma 34}}_{\text{Scattering Effects}} \right\} \tag{2.35}$$

where p is the particle momentum, S_0, X_0 and Θ_0 are the initial position and angle of the particle, Δ is the set of measurement errors on the tracking stations, and Θ_σ and S_σ are the angular deviations and displacements due to the multi Coulomb scattering (MCS) in the passive materials.

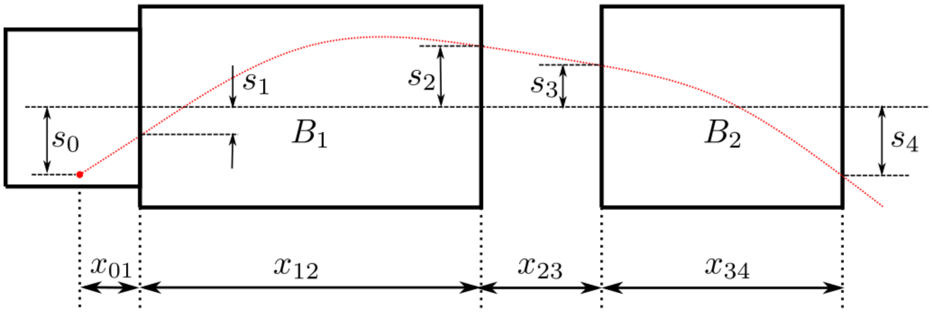

Figure 2.13: Schematic layout of the magnetic system: two magnetised regions are present alongside a target region where muon are generated.

At each tracking station the state of the particle is defined by the angle Θ_i and the vertical displacement S_i, the vertical displacement is measured by the tracker, whereas the angle, we assume it is not directly provided by the tracking station measurement. The particle dynamic is modelled using the classical equation of motion in the small angle approximation:

$$\text{Displacement:}\begin{cases} S_4 - S_3 = \Theta_3\, x_{34} + \dfrac{qB_2}{2p} x_{34}^2 + S_{\sigma 34} \\ S_3 - S_2 = \Theta_2\, x_{23} \\ S_2 - S_1 = \Theta_1 x_{12} + \dfrac{qB_1^*}{2p} x_{12}^2 + S_{\sigma 12} \\ S_1 - S_0 = \Theta_0 x_{01} + S_{\sigma 01} \end{cases} \tag{2.36}$$

$$\text{Angle:}\begin{cases} \Theta_3 = \Theta_2 \\ \Theta_2 = \Theta_1 + \dfrac{qB_1^*}{p} x_{12} + \Theta_{\sigma 12} \\ \Theta_1 = \Theta_0 + \Theta_{\sigma 01} \end{cases} \tag{2.37}$$

where the superscript $*$ denotes a corrected field to take into account the presence of gaps in the first magnet section, and the quantities with subscript σ are the effects of the scattering, assumed to be random variables.

Replacing the angle equations (2.37) in the displacement equations (2.36) it yields

$$\begin{aligned} S_{43} &= S_4 - S_3 = \Theta_0\, x_{34} + \frac{qB_1^*}{p} x_{12} x_{34} + \Theta_{\sigma 01} x_{34} + \Theta_{\sigma 12}\, x_{34} + \frac{qB_2}{2p} x_{34}^2 + S_{\sigma 34} \\ S_{32} &= S_3 - S_2 = \Theta_0\, x_{23} + \frac{qB_1^*}{p} x_{12} x_{23} + \Theta_{\sigma 01} x_{23} + \Theta_{\sigma 12}\, x_{23} \\ S_{20} &= S_2 - S_0 = \Theta_0\, (x_{12} + x_{01}) + \frac{qB_1^*}{2p} x_{12}^2 + \Theta_{\sigma 01} x_{12} + S_{\sigma 12} + S_{\sigma 01} \end{aligned} \tag{2.38}$$

Momentum Estimator To simplify the approach, we would like a momentum estimator based on a linear combination of the measured particle displacements. Using the displacement difference as expressed in (2.38), we obtain

$$\alpha S_{43} + \beta S_{32} + \gamma S_{20} = (\Theta_0 + \Theta_{\sigma 01})(\alpha x_{34} + \beta x_{23} + \gamma x_{02}) + \frac{q}{2p} \mathcal{B}(\alpha, \beta, \gamma) + \Sigma(\alpha, \beta, \gamma) \tag{2.39}$$

where α, β and γ are parameters to be chosen and $x_{02} = x_{01} + x_{12}$, and Σ and $\mathcal{B}$ are the effects of scattering and magnetic field respectively

$$\mathcal{B}(\alpha, \beta, \gamma) = (2\alpha x_{34} + 2\beta x_{23} + \gamma x_{12}) B_1^* x_{12} + \alpha B_2 x_{34}^2 \tag{2.40}$$

$$\Sigma(\alpha,\beta,\gamma) \quad = (\alpha x_{34}+\beta x_{23})\,\Theta_{\sigma 12}+\gamma S_{\sigma 12}+\gamma(S_{\sigma 01}-x_{01}\Theta_{\sigma 01})+\alpha S_{\sigma 34} \tag{2.41}$$

Note that Σ and $\mathcal{B}$ also depend on the spacing between tracking stations x_{ij} although it is not explicitly written in notation (2.40) and (2.41). Moreover, Σ, while being provided by the MCS, is thought to be a random variable.

In order to remove the dependence of the momentum on the unknown initial angle Θ_0, the coefficients α, β and γ must satisfy the constraint

$$\alpha x_{34}+\beta x_{23}+\gamma x_{02}=0 \tag{2.42}$$

so that Eq. (2.40) and Eq. (2.41) are recast as functions of α and γ only

$$\mathcal{B}(\alpha,\gamma) \quad = \alpha B_2 x_{34}^2-\gamma B_1^* x_{12}(x_{12}+2x_{01}) \tag{2.43}$$

$$\Sigma(\alpha,\gamma) \quad = \alpha S_{\sigma 34}+\gamma(S_{\sigma 12}-x_{02}\Theta_{\sigma 12})+\gamma(S_{\sigma 01}-x_{01}\Theta_{\sigma 01}) \tag{2.44}$$

and the reciprocal of the momentum is given by

$$\frac{1}{p}=\frac{2}{q}\frac{\alpha S_{43}+\beta S_{32}+\gamma S_{20}-\Sigma(\alpha,\gamma)}{\mathcal{B}(\alpha,\gamma)} \tag{2.45}$$

The tracking station measurement is affected by error, modelled by defining the measured displacement $\overline{S}_i=S_i+\Delta_i$, where Δ_i is a random variable with zero mean and standard deviation ε.

Using the displacements available from measurements (affected by error), we define the estimator

$$\hat{\Pi}(\alpha,\gamma)=\frac{2}{q}\frac{\alpha\,\overline{S}_4+(\beta-\alpha)\,\overline{S}_3+(\gamma-\beta)\,\overline{S}_2-\gamma\,\overline{S}_0}{\mathcal{B}(\alpha,\gamma)} \tag{2.46}$$

since the scattering error has zero average, the expected value of the estimator (2.46) yields the reciprocal of the momentum

$$\mathbb{E}\left[\hat{\Pi}\right]=\frac{1}{p} \tag{2.47}$$

where the operator $\mathbb{E}$ is the expected value.

There are three main sources of error to be taken into account in the momentum measurement of the muon:

- Energy loss
- The deflection due to the MCS
- The finite position resolution of the trackers

Therefore in order to evaluate the momentum resolution, having already an estimator for $1/p$, an estimate of the momentum standard deviation is required. After some algebra, Eq. (2.46) and Eq. (2.45) give

$$\sigma\left[\hat{\Pi}\right] = \frac{2}{q}\,\frac{\sqrt{\varepsilon^2[\alpha^2+(\beta-\alpha)^2+(\gamma-\beta)^2+\gamma^2]+\sigma^2_\Sigma(\alpha,\gamma)}}{|\mathcal{B}(\alpha,\gamma)|} \tag{2.48}$$

where σ is the standard deviation, and σ^2_Σ is the variance referred to the scattering defined in [31] as

$$\sigma^2_\Sigma(\alpha,\gamma) = \frac{P_0^2}{p^2}\left[\frac{\gamma^2}{3}\left(\frac{x_{01}^3}{X_\mathrm{T}}+\frac{x_{12}^3+3x_{01}x_{12}x_{02}}{X_\mathrm{C}^*}\right)+\frac{\alpha^2}{3}\frac{x_{34}^3}{X_\mathrm{C}}\right] \tag{2.49}$$

with $P_0 = 15$ MeV/c, and X_M and X_T represent the radiation lengths associated with the magnets' and target's passive materials, respectively. The asterisk (*) indicates that the radiation length should include a correction to account for the fact that the first magnetized region is not entirely composed of passive material, as it contains *gaps* for the detectors, this could also be modelled introducing a *filling factor* for the first magnetised area:

$$X_\mathrm{C}^* = X_\mathrm{C}\,\cdot f_\mathrm{C}$$

The momentum resolution (or momentum uncertainty) is defined as $\sigma[\hat{P}]/p$. Assuming the standard deviation to be much smaller than the mean of $\hat{\Pi}$, the resolution on the momentum is obtained using the propagation of uncertainty, i.e. truncating the Taylor expansion of $\hat{P} = \hat{\Pi}^{-1}$ at the first order around the expected value. The resolution on the momentum is then approximated with the resolution on its reciprocal

$$\sigma\left[\hat{P}\right] \approx \sqrt{\left(\frac{\mathrm{d}}{\mathrm{d}\hat{\Pi}}\hat{P}\right)^2}\Bigg|_{\hat{\Pi}=\mathbb{E}[\hat{\Pi}]} \sigma[\hat{\Pi}] = p^2\,\sigma[\hat{\Pi}] \implies \frac{\sigma[\hat{P}]}{p} \approx p\cdot\sigma[\hat{\Pi}] \tag{2.50}$$

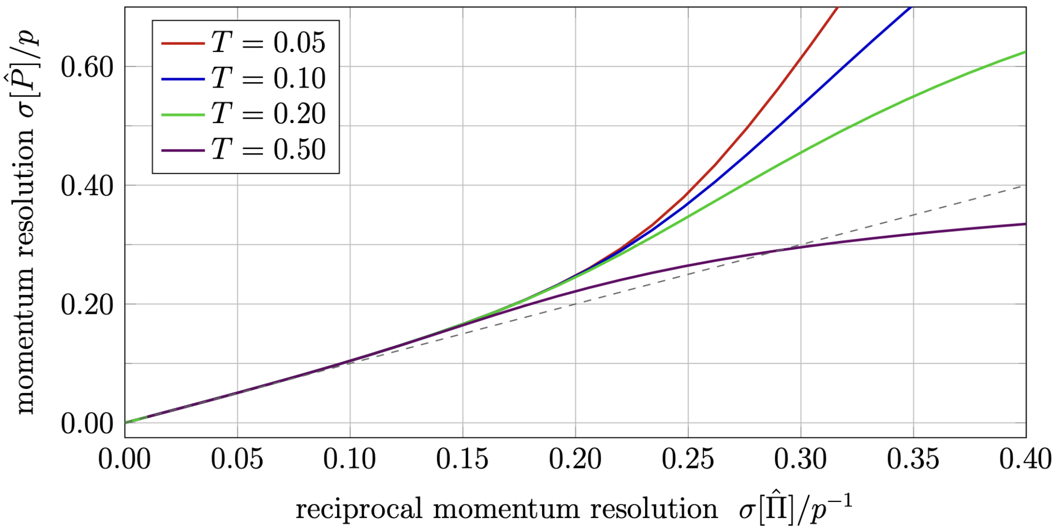

Figure 2.14: The standard deviation of the relative error is shown as a function of the resolution of $1/p$ for various values of the threshold $p_{\max}$. The grey dashed line represents the identity function, which corresponds to the resolution predicted by the first-order model.

This approximation usually holds for small values of the standard deviation, roughly up to $\sigma[\hat{P}]/p \approx 0.15$, but it underestimates the actual resolution, especially for higher values of $\sigma[\hat{P}]/p$, as can be shown in Figure 2.14. An exact computation of the relation between $\sigma[\hat{P}]$ and $\sigma[\hat{\Pi}]$ is not possible due to a non-integrable singularity. In order to solve this issue, we consider a maximum limit $p_{\max}$ for the measured momentum, assuming that the measurements exceeding such threshold are due to errors. Given a chosen threshold, it is possible to integrate numerically the probability distribution, obtaining the relation between the momentum resolution and the resolution on the momentum reciprocal.

Higher-order approximations yield more accurate analytical results, but the equations quickly become complex, and the improvement is only marginal [31].

2.2 EM field and particle interaction numerical tools

2.2.1 The Magneto Quasi Static formulation

Solving an EM field problem in the context of a magnet's design requires knowing the value of the magnetic flux density at every point of the space. Maxwell equations offer the general framework formulation allowing to solve any EM problem in general. They can be written as the following, in their differential form:

$$\begin{cases} \nabla \cdot \vec{D} = \rho \\ \nabla \times \vec{E} = -\frac{\partial \vec{B}}{\partial t} \\ \nabla \cdot \vec{B} = 0 \\ \nabla \times \vec{H} = \vec{J} + \frac{\partial \vec{D}}{\partial t} \\ \nabla \cdot \vec{J} = -\frac{\partial \rho}{\partial t} \end{cases} \tag{2.51}$$

Eqs (2.51) are a set of partial derivative equations defined on the domain Ω. A unique solution can be provided if:

- **Constitutive equations** are defined, which for linear, isotropic and time-invariant media are:

  $$\begin{cases} \vec{J} = \sigma \vec{E} + \vec{J}^* \\ \vec{B} = \mu \vec{H} \\ \vec{D} = \varepsilon \vec{E} \end{cases} \tag{2.52}$$

  where $\vec{J}^*$ is the imposed current field.

- Proper **boundary conditions** are defined, i.e. tangential components of $\vec{E}$ or $\vec{H}$ field or normal components of $\vec{J}$, $\vec{D}$, $\vec{B}$ fields.

- In case of non-stationary time-domain problems, **initial conditions** are to be set as well.

- Within homogeneous domains, spatial regularity of the components of the unknown fields must be satisfied. In practical problems — where different materials are involved — such condition is not satisfied, therefore Eqs. (2.51) must be written for each material and **interface conditions** must be defined on the surface of separation of media with different properties.

However, in many practical problems some, time derivative terms can be considered as zero or even neglected. In this case, simplified models are concerned, namely *static* or *quasi-static*, in which the delay of the propagation of the signal can be either zero or neglected. In the context of magnet's design **magneto-static** (MS) and **quasi-stationary magnetic** (QSM) models are involved. In the present work, since it is aimed at stationary detectors, only MS problems are considered.

The magneto-static problem aims at the definition of the magnetic field $\vec{H}$ and magnetic induction field $\vec{B}$ values starting from the distribution of the current field in the whole space. In particular, the set of Maxwell equations simplifies to:

$$\begin{cases} \nabla \times \vec{H}_k = \vec{J}_k^* \\ \nabla \cdot \vec{B}_k = 0 \\ \vec{B}_k = \mu_k \vec{H}_k \end{cases} \tag{2.53}$$

when considering — without loss of generality — two homogeneous and linear domains with different magnetic permeability, where $k = 1, 2$.
As previously stated, boundary conditions are required to assure the uniqueness of the solution:

$$\begin{cases} \vec{B} \cdot \hat{n}_s \big|_{\Sigma B} = 0 \\ \vec{H} \times \hat{n}_s \big|_{\Sigma H} = 0 \\ \left| \vec{B} \right|_{r \to \infty} \Big|_{\Sigma \infty} \to 0 \quad \text{as } r^{-3} \end{cases} \tag{2.54}$$

And with them, interface conditions must be defined on the separation surface Σ_{12}:

$$\begin{cases} \vec{H} \times \hat{n}_s = \vec{K}_\Sigma \\ \vec{B} \cdot \hat{n}_s = 0 \end{cases} \tag{2.55}$$

with $\vec{K}_\Sigma$ a surface current on Σ_{12}. This assures the continuity of the normal and tangential components of the magnetic induction field and magnetic field in the interface between the two media. However, there are some caveats to be taken into account when magneto-statics is concerned:

- All magnetic materials often used in magnet's design have a non-linear characteristic, therefore the third relation in (2.53) is adopted only as a simplification and in numerical computations where the μ_k is computed iteratively at each step. In the general case $\vec{B} = f(\vec{H})$ where f can be either a matrix or even a tensor when the material is not isotropic.

- It is not always possible to work with scalar potentials therefore the magneto-static problem is intrinsically a vector problem, at least — in the best case scenario — N^2 times more demanding in terms of computational time and memory allocation, where N is the number of unknown scalars.
- The first two boundary conditions in (2.54) are rigorously satisfied only when the symmetry of the geometrical domain and the sources is concerned. Without it, they could be used to provide approximated solutions. Therefore, in general, the magneto-static problem is solved on unlimited domains.

These limitations make the magneto-static problem the most difficult among the stationary problems, therefore different formulations have been proposed in the literature. The formulation based on the vector magnetic potential $\vec{A}$ is the one used in projects carried out in the PhD, which will be discussed in the following. As a matter of fact, the magneto-static problem — defined $\vec{B} = \nabla \times \vec{A}$ — can be expressed as follows:

$$\nabla \times \frac{1}{\mu} \nabla \times \vec{A} = \vec{J}^* \qquad \begin{cases} \nabla \times \vec{A} \cdot \hat{n}_s \big|_{\Sigma B} = 0 \\ \frac{1}{\mu} \nabla \times \vec{A} \times \hat{n}_s \big|_{\Sigma H} = 0 \\ \left| \vec{A} \right|_{r \to \infty} \Big|_{\Sigma \infty} \to 0 \quad \text{as } r^{-2} \end{cases} \tag{2.56}$$

with the conditions

$$\begin{cases} \left[\nabla \times \vec{A} \right] \cdot \hat{n}_s \big|_{\Sigma_{12}} = 0 \\ \left[\frac{1}{\mu} \nabla \times \vec{A} \right] \times \hat{n}_s \big|_{\Sigma_{12}} = 0 \end{cases} \tag{2.57}$$

Gauge definition

However, the main disadvantage of such a formulation is that $\vec{A}$ is a vector field and in general (2.56) doesn't have a unique solution since $\vec{A}' = \vec{A} - \nabla \Psi$, where Ψ is a scalar field, still satisfies the equations in (2.56). In this respect, an additional constraint must be applied on $\nabla \cdot \vec{A}$ according to the Helmholtz-theorem, namely "gauge", in order to restore the uniqueness. One of the most common gauges in the context of the magneto-static problem is the gauge of Coulomb:

$$\nabla \cdot \vec{A} = 0 \tag{2.58}$$

Alternatively, a different choice can be the following:

$$\vec{w} \cdot \vec{A} = 0 \tag{2.59}$$

where $\vec{w}$ is an arbitrary vector field without closed field lines. This last choice can be used when solving the magneto-static problem numerically based on the *finite element method*. With such methods, the domain is modelled by a mesh. In analogy with electrical circuits, the edges of the mesh can be broken down into the complementary sets of the three and co-tree. The last step is to use the set of the edges of the tree as $\vec{w}$ to impose the gauge [32]. This choice is found to be very advantageous if the functional basis used to find the solution is made by "edge elements". In this case, the unknowns are the line integrals of the vector potential along the edges of the mesh. In this case, the gauge is translated into posing to zero all the unknowns related to the edges of the tree of the mesh and looking for the solution in the sole functional basis made up of unknowns related to the edges of the co-tree.

Both of the aforementioned problems are solved if the geometry of interest is 2-D. In this hypothesis — in a Cartesian plane (x, y, z) — let us suppose that the current density is in the form

$$\vec{J} = J_z(x, y)\hat{i}_z$$

The magnetic induction field $\vec{B}(x, y)$, will have zero as the z-component and — in the Coulomb's gauge — the vector potential can be expressed as:

$$\vec{A} = A_z(x, y)\hat{i}_z$$

therefore if follows

$$\vec{B} = \nabla \times \vec{A} = \nabla A_z(x, y) \times \hat{i}_z$$

so that the solving equation becomes:

$$\nabla \cdot \left(\frac{1}{\mu}\nabla A_z\right) = -J_z^* \quad \begin{cases} A_z\big|_{\Sigma B} = 0 \\ \frac{1}{\mu}\frac{\partial A}{\partial n}\big|_{\Sigma H} = 0 \\ |A_z|_{r\to\infty}\big|_{\Sigma\infty} \to 0 \quad \text{as } r^{-2} \end{cases} \tag{2.60}$$

with the conditions

$$\begin{cases} [A_z] \cdot \hat{n}_s\big|_{\Sigma_{12}} = 0 \\ \left[\frac{1}{\mu}\frac{\partial A}{\partial n}\right]\big|_{\Sigma_{12}} = 0 \end{cases} \tag{2.61}$$

The ungauged formulation

However, also in 3-D problems, it is often possible to numerically solve the MS problem using a formulation based on the magnetic vector potential $\vec{A}$ without imposing, at least explicitly, any gauge. In order to let the numerical solver to converge, some hypotheses must be satisfied. The solving equation requires the known term to be solenoidal for

$$\nabla \times \frac{1}{\mu} \nabla \times \vec{A} = \vec{J}^* \rightarrow 0 = \nabla \cdot \left(\nabla \times \frac{1}{\mu} \nabla \times \vec{A} \right) = \nabla \cdot \vec{J}^*$$

However, if the MS problem is solved in an iterative way with a FEM formulation, $\nabla \cdot \vec{J}^* = 0$ does not guarantee that the residual of the discretised equation converges to zero. It is indeed necessary that the known term belongs to the range accessible by the functional basis used for the numerical solution. In order to satisfy both conditions a two-step pre-processing on the known term is needed:

- Express the known term as the curl of a vector potential in order to ensure it to be divergence-free: $\vec{J}^* = \nabla \times \vec{T}^*$
- Project the vector potential on the functional basis made up of the form functions used for the solution of finite elements of the numerical problem

Fulfilling such conditions ensures that the known term is compatible with the used functional basis.
Actually, if the conjugate gradient method is used for the iterative numerical solution, it can be shown that the gauge on the vector potential is automatically imposed.
Finally, it can be noted that the ungauged formulation, when converging, allows to solve the numerical problem in a faster way for two reasons:

- Avoiding explicitly imposing the gauge reduces the number of equations to be solved.
- The pre-processing of the edges of the mesh is not needed to build the complementary sets of the tree and co-tree (if the gauge is numerically imposed as $\vec{w} \cdot \vec{A} = 0$).

2.2.2 COMSOL Multiphysics

A FEM formulation based on edge elements and a non-gauged magnetic potential vector formulation [33, 34] has been employed to find the DC steady-state magnetic non-linear solution for the total field through the Magnetic Fields interface of the AC/DC module of COMSOL Multiphysics [35] software package.

Boundary conditions have been imposed by infinite elements. The numerical solution of the non-linear equation system has been obtained using a flexible generalized minimum residual method (FGMRES iterative solver). For the solution of each linear step, an iterative method based on the geometric multi-grid couples with a successive over-relaxation (SOR) pre-smoother and post-smoother has been used. Before performing the steady-state study, a coil geometry analysis through a COMSOL built-in tool has been preliminarily performed in order to compute the current flowing within the coil elements [16]. This step, as already mentioned, is essential to avoid imposing the gauge explicitly.

In particular, regarding the infinite boundary condition, a good approximation of the field to the infinite is achieved using a particular kind of spherical shell with thickness *dR*. The characteristic relationships of the material are chosen in order to simulate the behaviour of a spherical shell with a hundreds times greater thickness. However, the spherical symmetry of the boundary conditions requires that the barycentre of the domain of the currents and materials with high permeability is placed at the center of the domain. Additionally, in order to improve the quality of the solution, a structured mesh is used: in particular attempts were made to use hexahedrons and prisms wherever possible. These regions were then connected through buffer regions modelled with pyramidal elements, together with more irregular areas of the domain in which the use of tetrahedral elements was unavoidable. The fineness of the mesh indeed directly impacts the accuracy of the solution, finer meshes are required in regions with higher field gradients, such as near the coils or magnetic core.

2.2.3 Geant4

Modern particle and nuclear physics experiments present significant challenges in developing complex and resilient software frameworks and applications. A critical aspect of this is the growing need for large-scale, precise, and comprehensive simulations of the particle detectors employed in these experiments and in this perspective, GEANT4 has been developed.

The GEANT4 (Geometry and Tracking) [36] simulation toolkit is a powerful and widely used platform for simulating the passage of particles through matter. Developed and maintained by the CERN collaboration, GEANT4 is designed to handle the complexities of particle interactions with materials, making it an indispensable tool in High Energy Physics (HEP) and other fields that require detailed modelling of particle behaviour.

Every aspect of the simulation process has been addressed: the system's geometry, the materials involved, the fundamental particles of interest, particle tracking through materials and external magnetic fields, the physics processes governing particle interactions, and the response of sensitive detector components.

The toolkit enables users to construct a geometric model comprising numerous components of varying shapes and materials, as well as to define "sensitive" elements that record information (hits) necessary for simulating detector responses (digitisation). Additionally, GEANT4 offers an extensive set of physics processes to accurately model particle behaviour.

Volumes and materials

GEANT4 makes use of *logical* and *physical* volumes to describe the structure of a detector or in general a complex and a *material* which the volume is made of that comes in to place when particle interactions with matter is concerned. A logical volume defines a detector element with a specific shape that can enclose other volumes and possess various attributes. The physical volume specifies the spatial arrangement of the logical volume relative to an enclosing mother (logical) volume. This arrangement enables the construction of a hierarchical tree structure, where each volume can contain smaller nested volumes. Materials on the other hand are made of a single element or a mixture of elements, elements are made of a single isotope or a mixture of isotopes; therefore specifying the material of a volume defines the behaviour of particles when interacting with them.

Particle propagation

A large variety of interactions is experienced by particles passing through matter. In GEANT4 this variety is expressed by a division into several major process categories, including: *electromagnetic*, *hadronic*, *transportation* and *decay*. Each particle type contains a list of physics processes that the particle can undertake. For a particle interaction or decay it is useful to distinguish between the *process*, i.e. a particular initial and final state which therefore has a well-defined cross-section or mean-life, and the *model* that implements the production of secondary particles, in this respect there is the possibility of offering multiple models for the same process. In GEANT4, particles are moved in steps that are determined by physics processes or by the detector geometry, therefore all physics processes associated with the particle propose a *step*.
A particle in flight is subject to many competing processes. Moreover, in a real detector, it will often travel through many regions of different materials, shapes and sizes before interacting or decaying. In simulation, the particle proceeds in steps, and we have to find an efficient and unbiased way of choosing what limits the step and, if the particles continue, of updating the parameters for the next step. The process which returns the smallest distance is selected and its *post step action* is invoked. If this is an interaction or decay, the particles is *killed* and secondaries are generated. If not, the particle gets another chance to interact or decay.

GEANT4 neutrino simulation for SND

In the context of such a PhD work, experiments of interest are related to neutrino physics, therefore the performance of the magnetic system's design from the physics point of view has been assessed with muons produced in simulated neutrino interactions occurring in the experimental apparatus.
The GEANT4 simulation is the last step of a 3-step simulation "recipe" with three different simulation packages, i.e. FLUKA [37, 38], GENIE [39] and finally GEANT4. Details on the first two simulation packages are out of the scope of this work, nevertheless, information about the neutrino flux such as the energy spectrum and position distribution recorded on a virtual scoring plane are provided by the FLUKA simulation. This is therefore given to the GENIE neutrino event generator which simulates neutrino interactions in the experiment material.

The simulation of the neutrino interaction involves the production of several particles, including muons, particularly in muon neutrino interactions. The **propagation** of particles through the experimental apparatus coming from the interaction is then simulated with GEANT4, including the bending in magnetic field in case of charged particles. The experiment geometry, including the magnetic spectrometer, is modelled as **volumes** with appropriate **materials** — e.g. copper for the coil, iron for the yoke — which GEANT4 takes into account to simulate particle interactions with matter.

Additionally, detectors — implemented as *sensitive* elements — record the passage of particles as **hits** which are provided as a set of different pieces of information, including their (x, y, z) coordinates. Hits, in particular the ones from muons, are therefore used as the main information element for assessment of the muon magnetic spectrometer performance.

2.3 A dedicated Dipole Magnet Matlab tool

It has been already mentioned, in Sec 2.1, how in early magnet design phases and, even more, for multi-objective optimization processes, analytical modelling, although approximate, can be practically largely superior to typical Multiphysics numerical simulation. In particular the early definition of parameters, within the context of general design of experiments in large collaborations, is often a complex process requiring several iterations and prompt evaluation of new proposals.

In response to such a challenge a dedicated Matlab tool has been built — within the group of Electrical Engineering participating in the SHiP and SND@LHC Collaborations — with this Ph.D. work as part of its development. It utilizes analytical formulae as introduced and discussed in Sec. 2.1, combining both engineering and physical issues at the same time. Its key advantages lie in its speed and flexibility, allowing it to quickly adapt to sudden parameter changes.

Moreover, it has been the basis for power optimization and a more general optimization framework, as it will be shown in Chap. 3.

In particular, the contributions to the Matlab tool within this Ph.D. activity have been the reformulation of the optimization process to address multiple factors including particle momentum resolution and, additionally, software documentation as well as a general re-organization have been tackled.

Available analyses and parameters

The tool is the result of different contributions addressing several aspects of the magnet's design, ranging from the modelling of basic physical requirements, geometrical constraints and of the iron non-linearity to the thermal analysis.
The underlying mathematical core is the non-linear reluctance model for dipole magnets, detailed in Sec. 2.1, in the magneto-static formulation which is solved starting from the geometrical and electrical parameters provided as input. The flexibility of the model and the interchangeability of parameters are fully exploited by the encompassing framework, enabling a range of analyses tailored to the specific configurations of the magnet system, whether air-core or iron-core magnets, for instance.
Additionally, the framework computes a complete set of design-defining quantities, making it easy to examine their relationships through visualisations allowing for assessing the design.
The tool is organised into three primary sections.

Input parameters and constraints setting In this section, users can define magnet's input parameters and constraints, such as geometric dimensions as well as material properties. They can be categorized as:

- *Physics-Related Parameters*: This category focuses on the core physics requirements. It includes defining the desired muon momentum resolution, the maximum detectable momentum, and the resolution of the particle trackers. Users also select the method for muon momentum estimation, choosing between sagitta or bending angle methods.
- *Magnet Dimensions and Configuration*: Here, key dimensional constraints are set, such as the magnet's maximum height and the aperture size, along with the total active magnetised area. The design can accommodate different magnet configurations, whether a segmented structure with magnetised iron slabs or a single block for iron-core magnets. Additionally, this section specifies the conductor's cross-sectional area, the number of turns.

- *Cooling System Parameters*: This part involves defining the cooling system requirements, including the number of conductor pancakes, the cooling circuit's diameter, and the maximum allowable temperature difference between the inlet and outlet. These values are set following best practices and recommendations from sources such as [18].
- *Cost-Related Parameters*: Finally, the economic aspects are addressed by setting the material costs per weight unit and energy costs per kilowatt. Multiplying factors that account for the material manufacturing processes are also included, ensuring a realistic estimate of total costs based on the weight of materials used.

Computation of main electromagnetic features Based on the input parameters, the tool computes the main electromagnetic features including field strength as well as magneto-motive force, for instance. These computations are driven by underlying analytical scaling laws that describe the magnet's behaviour. The notation follows the conventions introduced in [14], with reference to Figure 2. The section presents different approximate expressions for the magnetic length depending on the magnet's type — either open or closed:

$$\ell_m = 2\left(\frac{c_s}{2} + \left(\frac{a}{2} + r_H\right)\sin\theta\right) \qquad \text{for open coil} \tag{2.62}$$

$$\ell_m = c_s + 2r_V + t \qquad \text{for closed coil} \tag{2.63}$$

where c_s is the length of the coil excluding curved sections, r_H and r_V represent the horizontal and vertical curvature radii, respectively, and θ is the coil aperture angle. The magnetic flux density in the active region, referred to as the reference magnetic flux density, can either be provided as an input or calculated based on the expected muon momentum resolution:

$$\frac{\Delta p}{p} = \frac{2\epsilon p}{qB_0\ell_m\ell} \tag{2.64}$$

Next, the flux balance equation is applied to determine the magnetic flux density in the iron yoke. For instance, in the case of an air-core magnet, the equation is:

$$B_0\ell_m(b+t) = B_{\text{Fe}}\ell_m 2h \tag{2.65}$$

This equation is neglecting the stray flux, which is a reasonable assumption for a non- or weakly-saturated iron yoke. However, in a general case, the contribution from the stray flux is non-negligible and therefore Eq. (2.65) modifies including an unknown B_{stray}, this is taken into account as well using reluctances in parallel.

Once the magnetic flux density in the iron yoke is obtained, the corresponding field strength in the yoke is evaluated. This is strictly related to the material used for the iron yoke. As a matter of fact, the characteristic B-H curve of the material is provided as discrete points, from which the field strength value is obtained by interpolating the curve. Most magnet designs aim for weakly saturated yokes to maintain high performance. At this stage, the main design figures of merit are introduced, including magnet efficiency, electrical power, and magneto-motive force (MMF). Thermal analysis is performed, where the number of pipes, water flow rate, and water velocity are calculated. Additionally, warnings are triggered if the design deviates from common recommendations, as discussed in Sec. 2.1.1 and shown in Table 2.1. The cost estimation section is included as well, applying the formulas defined in Sec. 2.1.1, which represent one of the contributions of this Ph.D. work to the tool. Specifically, the tool evaluates the total volume for the iron yoke — and the active region in iron-core magnets — and the coil, allowing for the calculation of both operational and capital costs. Total operating time can be provided as input as well.

Visualisation The visualisation section is the surrounding layer of the integrated optimization framework constituted by such a dedicated Matlab tool. Here results of the analyses are presented to the user allowing to assess the design features or possibly to adjust the parameters in order to achieve better performance within an optimization loop. Additionally, parameters can be provided as multiple sets of values, enabling — through visualisation — to explore the features space thanks to calculations handled by the core.

It enables users to analyse how changes in parameters affect the magnet's performance and design at a glance, offering visual insights through graphs.

Results of all the integrated analyses so far are presented through this functionality.

The **electromagnetic analysis** provides the relationship between the main electromagnetic features and the free parameters, Figure 2.15 — for instance — illustrates trends of magnet efficiency, power, MMF, magnetic flux density in the iron yoke as well as the stray magnetic flux density as a function of the iron yoke thickness for an air-core magnet. This visualisation enables users to easily identify optimal design points.

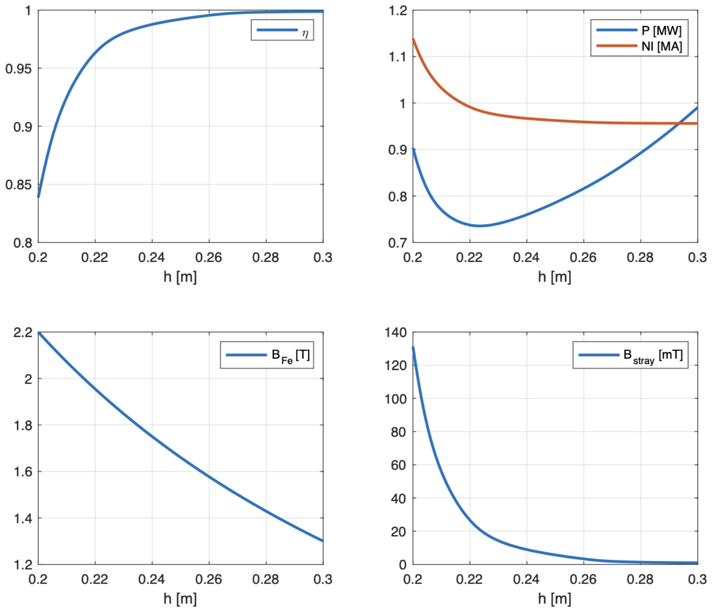

Figure 2.15: Main magnet figures of merit as functions of the iron yoke thickness: magnetic efficiency (top left), power and MMF (top right), magnetic flux density in the iron yoke (bottom left) and stray magnetic flux density (bottom right).

Moreover, a detailed **coil design analysis** — integrated into the tool — allows to provide a complete overview of the coil geometrical layout and its main parameters such as the arrangement of the conductors as well as the number of turns and their average length, as shown in Figure 2.16, where a sketch of the upper section of the coil of an air-core magnet is presented, visually highlighting the conductors' configuration.

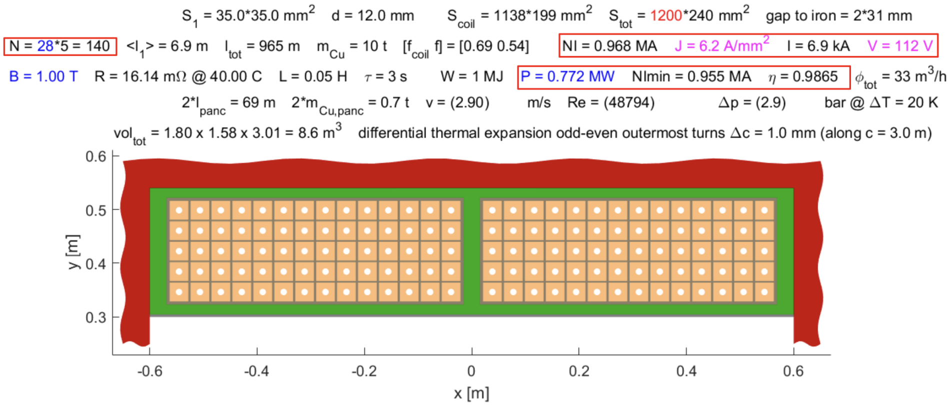

Figure 2.16: Conductors' configuration and coil main parameters as a result of the coil design analysis module for an air-core magnet.

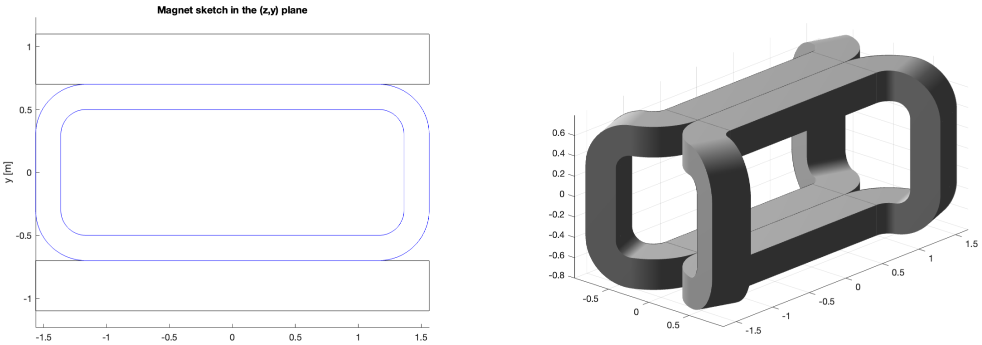

(a) (b)

Figure 2.17: 2-D (a) and 3-D (b) models as provided by the tool for an air-core magnet within an "open-coil" configuration.

Geometrical parameters computed among different modules of the tool are exploited to allow the visualisation of both **2-D and 3-D models** of the coil and of the overall magnet design, as illustrated in Figure 2.17 for an air-core magnet whose coil is provided with an aperture angle.

The **cost estimate** module, on the other hand, given the main cost parameters and exploiting the free parameters — as done already by the electromagnetic analysis module — provides a clear overview of the capital, operating as well as total costs, as illustrated in Figure 2.18, where magnet's costs are shown as functions of the overall thickness of the coil for a particular configuration of an air-core magnet design.

The integration of a graphic overview of the results from the **thermal analysis** module is in the scope of the future work of this Ph.D. activity. So far, results from thermal analysis are provided only as text output of the Matlab tool, nevertheless providing essential information about the design, a typical output of the module is illustrated in Figure 2.19.

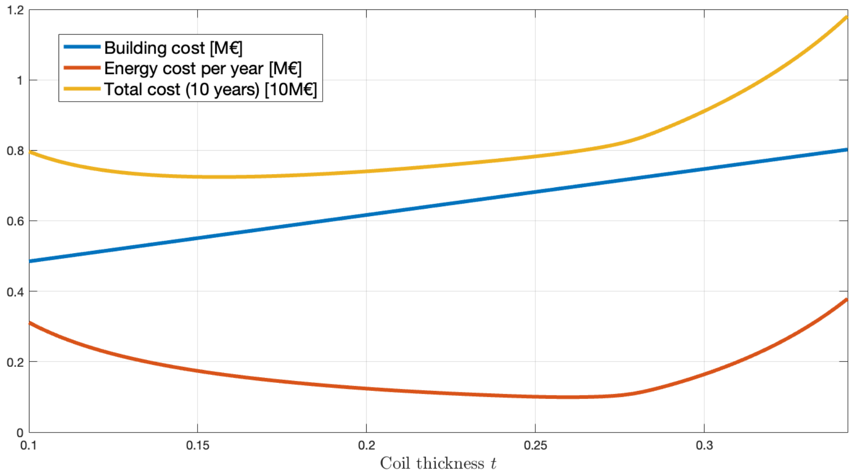

Figure 2.18: Building (blue), energy (red) and total (yellow) cost curves as functions of the overall coil thickness for an air-core magnet design configuration. Total cost accounts for a 10-year life span of the magnet, it has scaled by 10 for visualisation purposes.

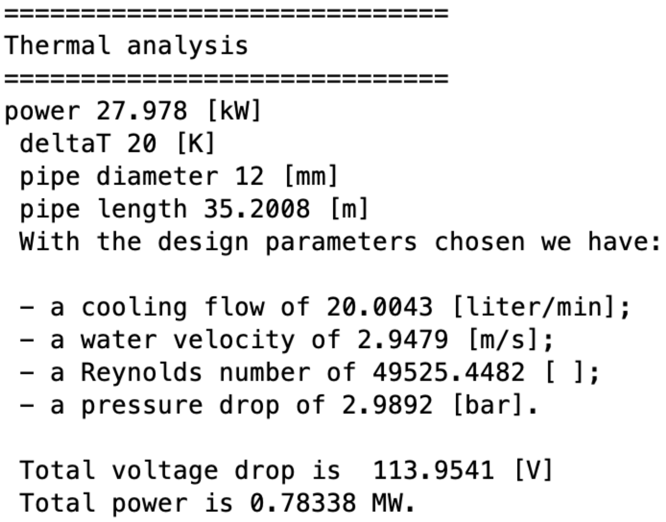

```
=============================
Thermal analysis
=============================
power 27.978 [kW]
 deltaT 20 [K]
 pipe diameter 12 [mm]
 pipe length 35.2008 [m]
 With the design parameters chosen we have:

 - a cooling flow of 20.0043 [liter/min];
 - a water velocity of 2.9479 [m/s];
 - a Reynolds number of 49525.4482 [ ];
 - a pressure drop of 2.9892 [bar].

 Total voltage drop is  113.9541 [V]
 Total power is 0.78338 MW.
```

Figure 2.19: Typical output of the thermal analysis performed on a particular air-core magnet design as provided by the Matlab tool.

Chapter 3

CASE STUDIES AND RESULTS

The analytical and semi-analytical models detailed in Chap. 2, implemented in a dedicated Matlab tool and validated through numerical methods, provide a robust framework for magnet design and optimization. This framework is applied — where feasible — in case studies conducted within the SND@LHC and SHiP experiments at CERN, described above. Although these are large collaborations, the design process is complex and has required multiple iterations, often driven by new proposals. Thanks to the efficiency of the dedicated Matlab tool, rapid evaluations have been possible to accommodate these evolving needs.

3.1 The upgrade of SND@LHC

The Scattering and Neutrino Detector (SND@LHC) is a compact stand-alone experiment to perform measurements with neutrinos produced at the LHC in a hitherto unexplored pseudo-rapidity region of $7.2 < \eta < 8.4$ [27], complementary to all other experiments at the LHC, where $\eta = -\ln(\theta/2)$, with θ angle of the trajectory with the main beam direction. The experiment is located 480 m downstream of IP1 in the unused TI18 tunnel. The configuration of such an experiment allows efficiently distinguishing between all three neutrino flavours, probing physics of heavy flavour production at the LHC in the region that is not accessible to ATLAS, CMS and LHCb. The physics programme includes studies of charm production, and lepton universality tests in the neutral sector.

The SND@LHC experiment has been collecting data at the LHC since the start of Run 3. While the results are promising, the Run 3 measurements will be statistically limited due to the geometric constraints of the current detector and the anticipated integrated luminosity. In 2024, the Collaboration submitted a Letter of Intent (LOI) [40] proposing a detector upgrade to fully leverage the potential of the High Luminosity LHC (HL-LHC), i.e. a factor 5 increase of instantaneous luminosity foreseen, and expand the LHC's physics reach in the neutrino sector.

Along with the increase of statistical precision, significant improvements are foreseen for the experimental setup: a **magnetic spectrometer** is planned which would allow the first experimental direct observation and the study of tau antineutrinos while extending the range of flavour conservation tests. The new magnetised detector is foreseen to be placed in the same area where the SND@LHC detector is currently located, i.e. in the TI18 tunnel at about 480 m from the ATLAS proton-proton interaction point (IP1).

Motivation

The SND@LHC experiment aims to detect high-energy neutrinos produced by the LHC to study their properties and investigate charm production in the very forward region. The initial results from the last few years of data collection, including the observation of collider muon neutrinos [41] and the measurement of the muon flux [42], have provided valuable insights into the signal and background environment. This progress sets the stage for further exploration of the LHC's neutrino physics potential. With key upgrades, the HL-LHC will significantly enhance the experiment's physics reach in both neutrino physics and Beyond Standard Model (BSM) searches.

The current SND@LHC detector maximises the available space in the TI18 tunnel to cover the desired pseudo-rapidity range. However, its 2021 design was based on the assumption that no civil engineering work could be completed in time for Run 3 operations. The planned upgrades aim to improve detector performance and address the geometric limitations caused by the tunnel's structure and sloping floor.
The energy measurement and muon identification set the lower limit for the detector's length. However, this requirement competes with the azimuthal angular acceptance of the target, which influences the overall intercepted flux and, consequently, the total number of observed interactions. Given the tunnel constraints and sloping floor, the Collaboration has proposed excavating the floor to reduce the impact of the proton beam crossing angle planned for Run 4 and to mitigate the potential effect of switching to a vertical crossing angle in Run 5.

In principle, the environment of TI18 doesn't permit the installation of a magnetic spectrometer. This limits the precision of the measurement of the neutrino energy and does not permit the separation of neutrinos from anti-neutrinos.

In this respect a possible spectrometer design must comply with all the constraints provided by either the environment or the physics of the processes of interest, i.e. measuring the momentum of muons outgoing from neutrino interactions. As a matter of fact, the main constraint sources can identified as:

- **Interface with the environment**: civil engineering works are needed in order to fit the magnet or in general the whole spectrometer system in the TI18 tunnel affecting the shape of the magnet itself. Moreover, the presence of the magnetic field generated by the magnet could affect the nearby LHC, or even viceversa, this sets a constraint on the stray field of the magnet. Furthermore, compliance with CERN power supply standards must be taken into account.
- **Physics**: a certain muon momentum resolution achieved by the spectrometer system is *desirable*, this sets a constraint mainly on the bending power $B\ell$ provided by the magnet. Furthermore, a high geometrical acceptance is required, therefore setting constraints on the magnet aperture and in general on its shape and dimensions.

Such constraints often don't go in the same direction, therefore a trade-off must be taken into account. However, different layouts and magnet designs have been proposed as a result of a feedback loop that has been established within groups involved in the Collaboration. In the following sections, different layouts and magnet designs — developed by our group and with contributions of this Ph.D. work — will be presented, highlighting their main features alongside their advantages and disadvantages.

3.1.1 The air-core spectrometer system

The first considered layout of a spectrometer system is a stand-alone one: a spectrometer made up of four tracking stations upstream and downstream of an air-core electromagnet, as shown in Figure 3.1. This layout features a compact vertex detector (also known as target) placed upstream, where the majority of neutrino interactions are expected to occur, followed by a hadronic calorimeter (HCAL) serving as a muon identification system. Downstream, a muon spectrometer is positioned to measure the muon's momentum. This modular design has been consistently applied across all iterations.

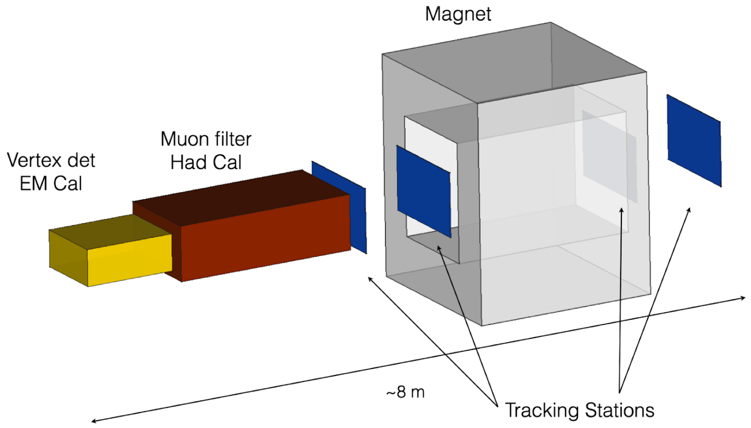

Figure 3.1: Schematic layout of the first proposed spectrometer system for the upgrade of SND@LHC.

The spectrometer is designed to employ the “bending angle” method, which estimates the muon momentum by measuring its deflection in a magnetic field. The resolution of the momentum measurement follows the relation, presented in Eq (2.32):

$$\frac{\Delta p}{p} = \frac{2\varepsilon p}{q B_0 \ell_\mathrm{m} \ell} \tag{3.1}$$

where in this case $\varepsilon = 100\ \mu\mathrm{m}$ and ℓ is the distance between two trackers and ℓ_m is the magnetic length, defined in Eq. (2.9). As seen in Eq (3.1), assuming the tracker technology — and hence ε — and the total length of the spectrometer as fixed, one can improve momentum resolution by either increasing the lever arm or enhancing the bending power of the magnet. The latter can be performed with a stronger magnetic field B_0 or — alternatively — a longer magnetic length ℓ_m.

This is a critical consideration: as an **air-core** magnet, significantly larger power is required — about 10^3 times more — than an iron-core magnet to magnetise the same volume. Moreover asking for a higher magnetic flux density or a longer magnetic length both require a larger magnet, which directly conflicts with the need for a compact design, constrained by limited space. However, employing an air-core magnet the contribution of the multi Coulomb scattering is drastically lower given the density difference between air and iron, therefore lower muon momentum resolutions (thus better) are expected.

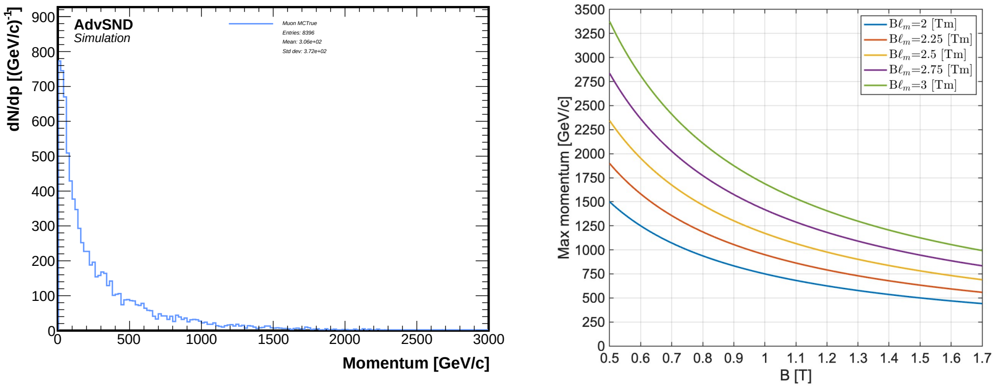

(a) (b)

Figure 3.2: Expected momentum distribution of muons from neutrino interactions (a), max momentum dependence on the magnetic flux density for different bending power values $B\ell_m$ (b).

The air-core design

The spectrometer's optimization was guided by several key targets: achieving high performance by minimizing muon momentum resolution, sustainability by reducing power consumption and keeping total costs low by minimizing material usage. At the same time, several constraints had to be considered: the magnet must fit within the available space, limiting both its length and cross-section; the stray field must be controlled to avoid interference with other devices and pose no health risks; and magnetic efficiency must be maximized.

An analysis has indicated that, under certain assumptions, the trends of the main figures of merit of the electromagnetic design — such as magnetomotive force and power consumption, coil and yoke dimensions — exhibit a monotonic relationship with respect to the magnetic flux density. Additionally, defined $p_{\max}$ as the maximum momentum for which a charge assignment is feasible

$$p_{\max} = \frac{qB_0\ell\ell_m}{8\varepsilon},$$

Figure 3.2 provides the relationship between $p_{\max}$ and the reference magnetic flux density B_0 at different values of the bending power $B_0\ell_m$. In particular, $p_{\max} =$ 750 GeV/c — which covers the 95‰ of the muon momentum distribution predicted by simulations — leads to a $B_0 = 1$ T if a bending power of 2 T m is considered. This has constituted the starting configuration for the design process.

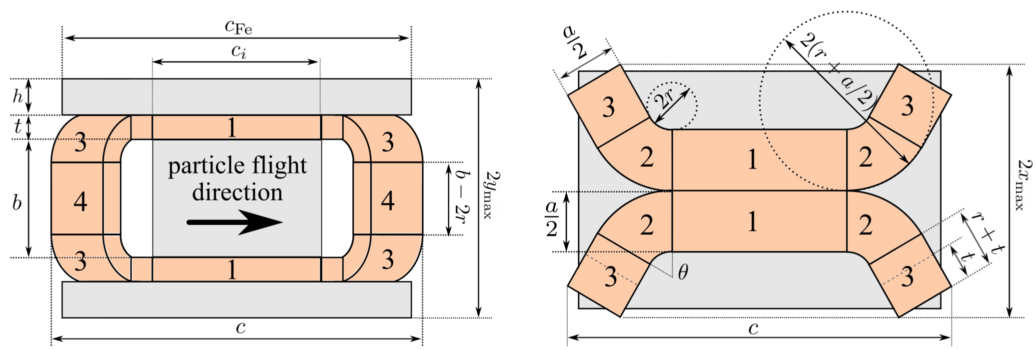

(a) (b)

Figure 3.3: Side view (a) and top view (b) of the magnet with the notation used in the formulas. Grey elements represent iron parts and orange elements represent copper parts.

The optimisation approach follows the one proposed in [15]. The analytical framework — described in Chap 2 — has been exploited providing a design solution which satisfies the dimensional and stray field constraints while minimizing the power consumption. The process starts by establishing fundamental constraints based on the physics requirements, such as the desired momentum resolution (defined in Eq.(3.1)) and the geometrical acceptance, which refers to the ratio of muons entering the magnet to the total number of incoming particles. Hence, the desired value of acceptance is achieved with an aperture of 1.20×60 m^2, defining a and b as the width and height of the aperture, respectively. Whereas, regarding the momentum resolution, a value lower than 0.2 has been considered desirable.

In addition to the physical requirements, further constraints are imposed by the limited available space. Specifically, the total length of the spectrometer, $L = c + 2\ell$, with ℓ as the distance between the trackers, as well as the transverse dimensions $2y_{\max}$ and $2x_{\max}$, shown in Figure 3.3, are taken into account. The exploitation of analytical laws — such as Ampere's law, the current density and power consumption expression — together with optimisation parameters and goals leads to different scenarios. In such a process, the total length of the magnet c, the overall thickness of the coil t and the aperture angle θ have been considered as the optimization set of independent variables.

All the remaining fundamental quantities can be obtained as a function of the independent variables:

- The magnetic flux density in the active region can be obtained from Eq. (3.1)
- The maximum magnetic flux density achieved in the iron yoke B_{Fe} can be obtained from the flux conservation:

  $$B_{\mathrm{Fe}} \approx \frac{(c_i + 2r\theta + 2r + t)(b + t)B_0}{2hc_{\mathrm{Fe}}} \tag{3.2}$$

  where $h = y_{\max} - t - a/2$ is obtained imposing the constraint on the maximum height of the magnet.
- The magnetomotive force can be expressed as:

  $$NI = \frac{B_0}{\mu_0}a + \frac{B_{\mathrm{Fe}}}{\mu_{\mathrm{Fe}}}(a + 2t) \tag{3.3}$$

  where the permeability, μ_{Fe} of the iron, is determined based on the magnetic field in the yoke B_{Fe}, after selecting the material. The AISI 1010 steel, with a nonlinear characteristic, has been chosen as a reference material for the yoke. To align with the specific heat used in the ATLAS experiment, an appropriate scaling has been applied, representing the worst case scenario for the current design. The characteristic $B - H$ curve is shown in Figure 3.4.
- The electric current density and the electrical power are in turn functions of the magnetomotive force:

  $$J = \frac{NI}{atf}, \qquad P = \rho_{\mathrm{Cu}}\, J^2\, V_{\mathrm{Cu}} \tag{3.4}$$

  where f is the filling factor of the coil, ρ_{Cu} is the copper electrical resistivity and V_{Cu} is the volume of the coil.

The relationship between power consumption — the objective to be minimised — and both coil thickness and magnet length is illustrated in Figure 3.5. The power minimum, marked by the blue dot, arises from several competing effects. Specifically, increasing the coil thickness lowers the current density, which is directly tied to power, but also reduces the yoke thickness, leading to saturation and therefore into an increase in reluctance, thus raising the magnetomotive force.

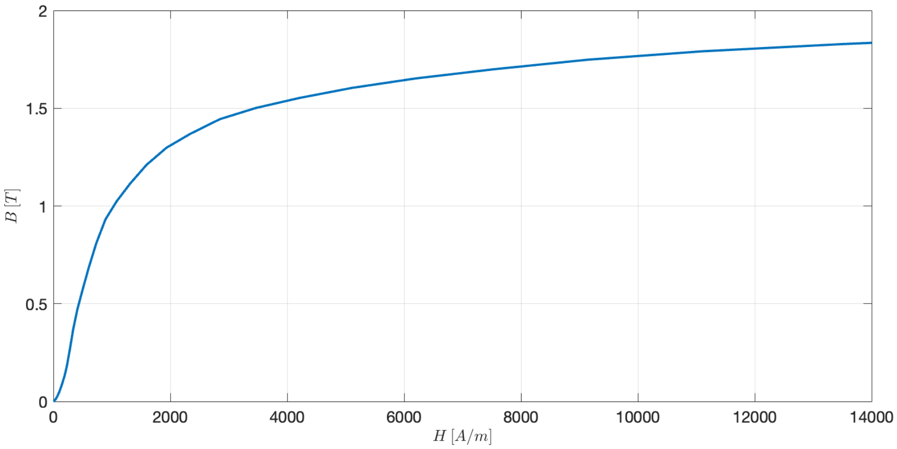

Figure 3.4: Magnetisation curve as modelled in the optimisation process, it has been obtained from the magnetisation curves already shown in Figure 2.10.

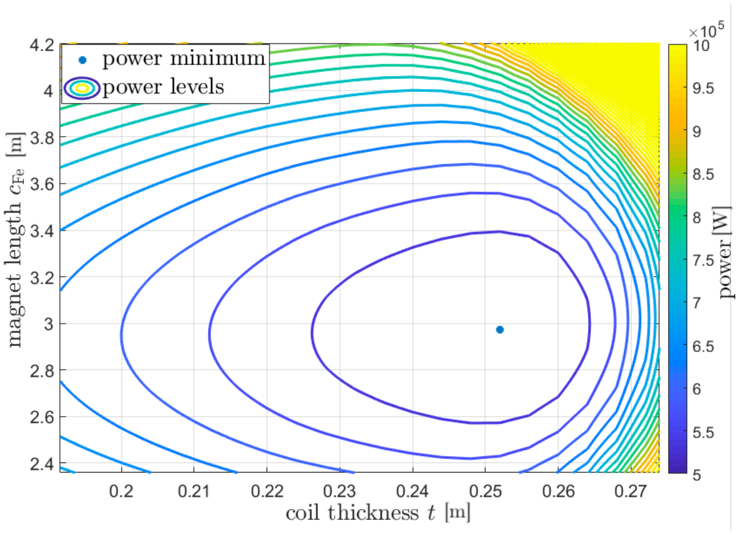

Figure 3.5: Level curves of the electric power as a function of the optimisation variables t and c_{Fe}, coil thickness and magnet length, respectively.

Meanwhile, the magnet length influences the denominator of Eq. (3.1), affecting both the strength of the magnetic field and the magnetised volume. The optimisation is performed numerically over a 3D grid by adjusting the three variables. It's worth noting that while exploring the variable space, the dependence on both c and θ is found to be quite smooth, eliminating the need for complex minimisation techniques. Figure 3.6 illustrates the scaling laws for power and magnetic field as functions of the magnetic length, for different values of the coil aperture angle.

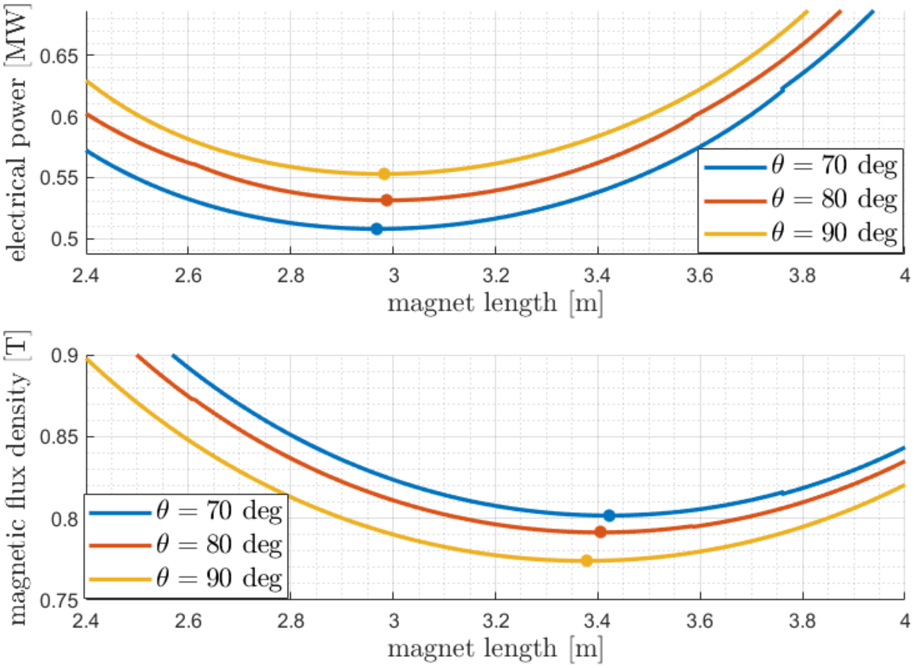

Figure 3.6: Scaling laws of minimum power and the corresponding magnetic flux density as a function of the magnet length c_{Fe} for three values of the coil aperture angle. These plots have been obtained considering $L = 6$ m, $p_{\max} = 800$ GeV/c, $t + h = 0.4$ m and $\Delta p/p = 0.2$.

The influence of coil thickness is eliminated by selecting, for each c, the coil thickness that minimises electric power. Interestingly, the parameters that minimise power do not correspond to the minimum magnetic field, which is often the focus when the physical design is conducted independently of the engineering design. This discrepancy highlights the advantage of a unified optimisation approach that incorporates both physical and engineering considerations.

Indeed, according to the step-by-step design approach the minimum magnetic field required for an opening angle of 80°, for instance – set at 0.8 T – is attained with a magnetic length of approximately 3.4 m which results in a power consumption of 0.56 MW. This value is approximately 10 % higher compared to the optimal solution identified using the unified approach.

Main magnet features	Value	Unit
Reference magnetic flux density	0.83	T
Total magnet length	2.96	m
Total power consumption	0.51	MW
Yoke thickness	15	cm
Coil thickness	20	cm
Coil fill factor	0.71	
Total turns	140	
Magnetomotive force	0.804	MA
Current per turn	5.7	kA
Current density	4.9	$\mathrm{A/mm^2}$
Voltage	88	V
Total resistance at 37.5°C	15	mΩ
Inductance	50	mH
Inlet-outlet temperature rise	15	°C
Water speed	2.5	$\mathrm{m\,s^{-1}}$
Reynolds number / 1000	43	
Pressure drop	2.3	bar

Table 3.1: Optimal design configuration obtained by zero-dimensional and 2D models after the optimisation procedure. Note that 2D model is referred to the sole thermal analysis.

Result

The key design parameters are presented in Table 3.1. Notably, copper hollow conductors have been chosen to enable active water cooling of the coil in a single pancake configuration, with all cooling parameters falling within the typical operating limits used in CERN experiments [43]. Remarkably, all features comply with the general recommendations outlined in the previous chapters. Before moving on to validation through simulations, a cost-benefit analysis was conducted as part of the design process. Based on the discussions in previous chapters, the main operational cost of the magnet system is determined by the electrical energy required to power the magnet, as expressed in Eq. (2.28). At the time of this analysis, the average cost of electricity in Europe was $F_p = 0.25$ €/kW h, though large research labs often have special contracts with energy providers, making a more realistic price range between $F_p = 0.05$ and 0.10 €/kW h.

On the other hand, evaluating the capital cost, as shown in Eq. (2.27), requires knowledge of the costs of iron and copper.

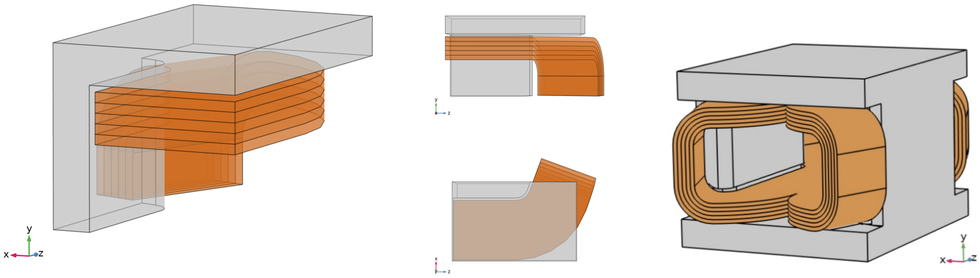

(a) (b)

Figure 3.7: Three-dimensional view of one-eighth of the magnet from different angles (a) and the full magnet model (b), showing the iron yoke in grey and the coil in orange.

A reasonable estimate for copper, $A_{\mathrm{Cu}} = 8.30$ €/kg, can be found in [44], while the cost of iron varies significantly depending on its type and application. For this analysis, the iron cost was assumed to be $A_{\mathrm{Fe}} = 1.5$ €/kg. Additionally, Eq. (2.27) has been adjusted with two multiplying factors — one for copper and one for iron — to account for manufacturing costs, which are proportional to their respective masses. Therefore, cost analysis for such a design yields to a capital cost of about 472 k€, and an operating cost of 156 k€, supposing a duty cycle of 70% in one year.It is noteworthy that, in less than three years, the operating cost becomes larger than the capital cost, therefore constituting the largest expense so far.

To verify the accuracy of the proposed design, the main results are compared with three-dimensional finite element (FE) electromagnetic models. A 3D FE model offers a more realistic representation of the final magnet, providing detailed insights into the spatial distribution of magnetic field variables. The magneto-static problem is implemented and solved numerically using COMSOL software. To reduce computational complexity by leveraging the model's symmetry, only one-eighth of the structure is simulated, as illustrated in Figure 3.7 (a). For visualisation purposes, Figure 3.7 (b) presents the complete magnet model. The mesh used for the FE analysis employs hexahedral elements and tetrahedra elements for the coil as well as iron yoke domains and the surrounding air domain, respectively. In Figure 3.8 the results of the FEM simulations, in terms of magnetic flux density norm $|B|$, both in 3D (a) and in 2D (b) views are presented. The bending power is calculated for a particle travelling through the center of the magnet, with B_0 representing the magnetic flux density component along the x-axis at the magnet's centre.

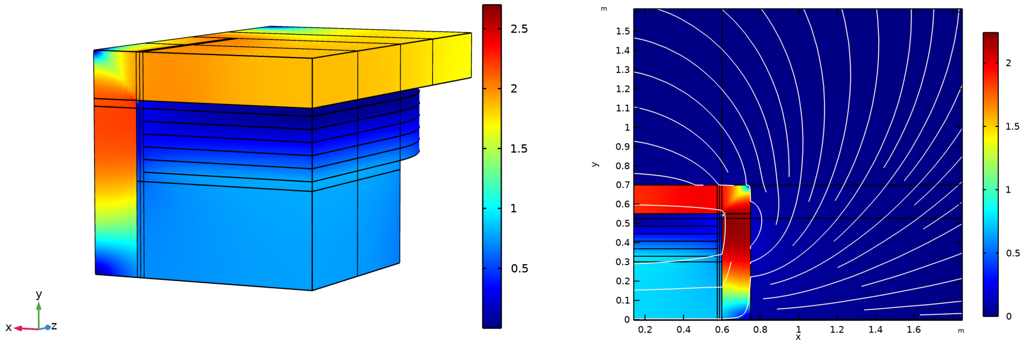

(a) (b)

Figure 3.8: Magnetic flux density norm $|B|$ 3D distribution inside the iron, coil as well as air aperture (a) and $|B|$ 2D mapping within the magnet and outside in a XY section at the centre of the magnet, corresponding to $z = 0$.

		Analytic value	Numeric value
Magnet bending power	[T m]	1.76	1.65
B_0	[T]	0.83	0.76

Table 3.2: Comparison between the main electromagnetic parameter values for analytic and FE numeric models.

In Table 3.2 the comparison between the values of the main electromagnetic parameters from the analytic and numeric models is reported. It's important to note that discrepancies between analytical and numerical values are within 8% by defect, indicating an 8% improvement in resolution.

In this case study, for reasons of time, simulation studies have been conducted on a previous unoptimized version nevertheless assessing preliminary physics performance, including geometrical acceptance and charge and momentum resolution. This design featured a 1 T air-core magnet with a uniform magnetic field along the x-axis, equipped with four tracking stations, as previously shown in Figure 3.1.
A simplified yet effective detector design was incorporated into the experimental geometry model within the SND@LHC software framework, as depicted in Figure 3.9. Muon neutrino charged current (CC) interactions GEANT4 Monte Carlo simulations were generated in the target region. Focusing on outgoing muons, the detection performance has been evaluated.

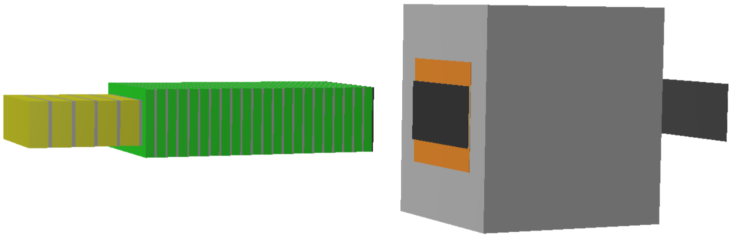

Figure 3.9: GEANT4 simplified 3D model of the first detector layout as implemented in the SND@LHC software framework geometry.

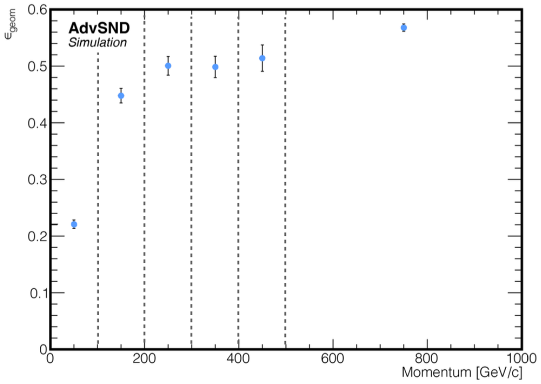

Figure 3.10: Geometrical acceptance provided by the spectrometer system as a function of the incoming muon momentum.

An overall geometrical acceptance of 50% — defined as the ratio of muons reaching the most downstream tracking station to the total muons produced in the target region — was achieved with an aperture of 1.20×60 m^2, as demonstrated in Figure 3.10. Although this acceptance is relatively low, optimization efforts have been made for later configurations. Additionally, the bending angle of muons was measured in both the θ_x and θ_y projections, with results presented in Figure 3.11. Since no deviation is expected in the x-projection due to the magnetic field's direction, the width of the fitted Gaussian distribution in Figure 3.11 (a), σ, represents the spectrometer's angular resolution. A 4σ cut [30] applied to the θ_y distribution results in a charge assignment efficiency of 83%, defined as the number of muons with angles above this threshold over the total number of muons traversing the spectrometer.

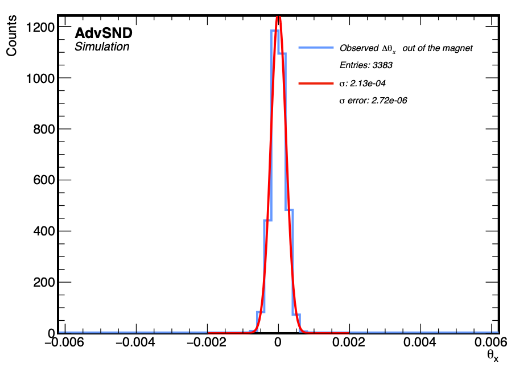

(a) (b)

Figure 3.11: Projections of the muon angle in the x (a) and y (b) directions. The θ_x distribution is fitted with a Gaussian to determine the spectrometer's angular resolution. By applying a 4σ cut to the bending angle, θ_y, a charge assignment efficiency of 83% is achieved.

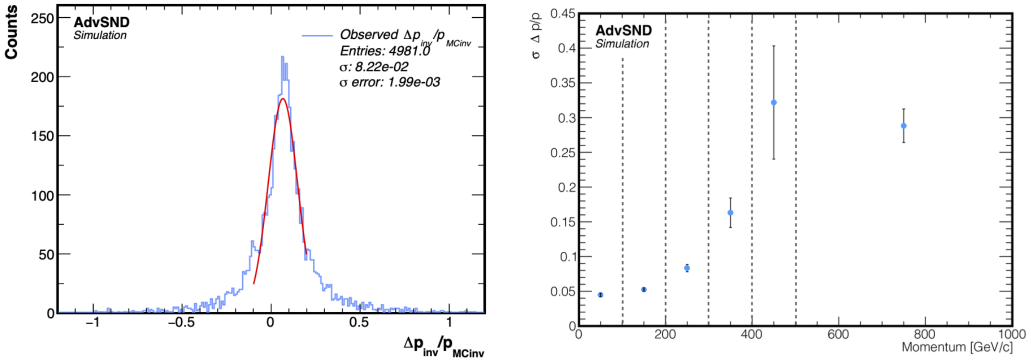

(a) (b)

Figure 3.12: Muon momentum resolution achievable by the spectrometer system as estimated by Geant4 simulation of ν_μ CC interactions in the target region: (a) overall and (b) as a function of the true momentum of the muon.

Momentum of muons has been estimated in the bending angle configuration and for that muon momentum resolution has been evaluated, as illustrated in Figure 3.12. An overall momentum resolution of 0.082 ± 0.002 is achieved, though this value varies significantly with the muon momentum. At a fixed bending power, higher-energy muons experience smaller bending angles, leading to reduced accuracy in momentum estimation. As shown in Figure 3.12 (b), the resolution tends to worsen as the momentum increases. Additionally, the larger error bars are attributed to the limited statistics of the muon momentum distribution, as depicted in Figure3.2 (a).

3.1.2 The iron-core spectrometer system

The second proposed configuration for the upcoming upgrade of the SND@LHC experiment involves the *magnetisation* of the HCAL. This magnet system is composed of two main parts: the HCAL, which consists of 21 detector planes interspersed with 22 magnetised iron slabs — referred to as the Hadron Calorimeter Magnet (HCM) — and a muon identification system. The muon system, known as the Muon System Magnet (MSM), is an iron-core magnet equipped with three tracking stations based on drift tubes, as shown in Figure 3.13. This configuration was largely influenced by space limitations. An air-core spectrometer with a bending angle setup would need around 9 meters of space, whereas magnetising the HCAL and incorporating an iron-core magnet downstream reduces the space requirement by approximately 1.5 times, offering a more compact solution. Notably, using an iron-core magnet in place of an air-core one significantly reduces the magnetomotive force and hence the magnet's power consumption by at least three orders of magnitude, primarily due to the large difference in magnetic permeability between iron and air. Additionally, the resulting low heat dissipation allows for the use of air cooling.

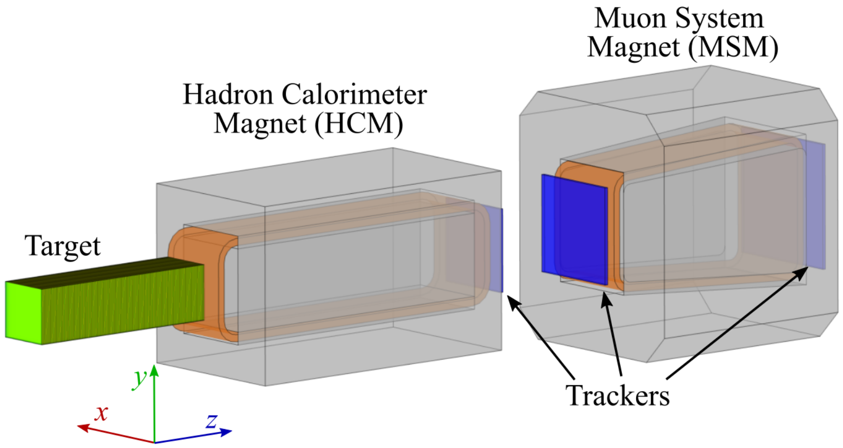

Figure 3.13: Schematic layout of the iron core configuration of the next upgrade of the SND@LHC experiment

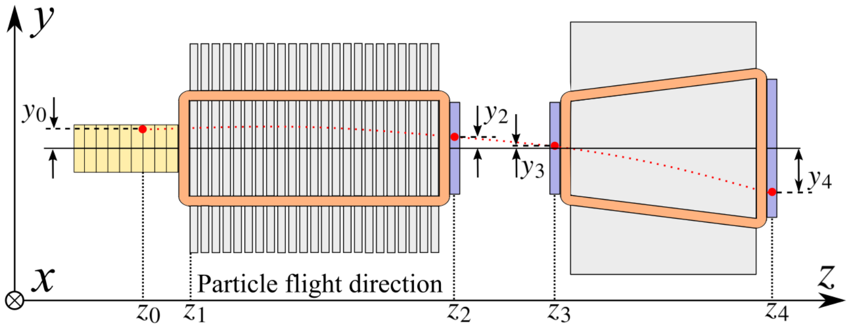

Figure 3.14: Lateral view of a schematic layout of the iron-core configuration, the red dotted line represents a possible muon trajectory and (y_i, z_i) are the positions recorded by the detector planes in the $y - z$ plane.

The iron-core design

As stated earlier, the design of the iron-core magnet for the spectrometer system might appear simple from the electromagnetic point of view, nevertheless, the problem of the scattering holds. The constraints were largely carried over from the previous design. However, in this case, the key parameters shaping the spectrometer specifications are muon momentum resolution and geometrical acceptance. These parameters can be improved by increasing the spectrometer's length and cross-section, but both are limited by the available space in the TI18 tunnel. In the following analytical statistical tools, described in Sec. 2.1.3, are applied. Referring to the notation in Figure 3.14, the displacement of a muon generated by a neutrino interaction in the target region, for a given magnetic flux density B, is approximately given by:

$$\Delta y = \theta_y \Delta z + \frac{qB}{2p}\Delta z^2 + \Delta y_\sigma \tag{3.5}$$

where θ_y represents the angle of the muon's momentum relative to the z-axis and Δy_σ accounts for the expected displacement due to scattering in the material.
By applying Eqs. (2.45) and (2.46) to this configuration, Eq. (2.48) from Sec. 2.1.3 yields:

$$\frac{\Delta p}{p} = \frac{2}{q}\frac{\sqrt{\varepsilon_s^2[2z_{02}^2 + z_{34}^2] + \varepsilon_t^2 z_{34}^2 + \sigma_\Sigma^2(p)}}{z_{02}z_{34}[z_{34}B + (z_{12} + 2z_{01})Bf_{\mathrm{HC}}]} \tag{3.6}$$

where ε_t and ε_s denote the position resolutions of the trackers within the target and around the magnets, respectively, and $\sigma_\Sigma(p)$ represents the error induced by scattering. Using Eq. (3.6), it becomes clear that the resolution improves with both the strength of the magnetic field and the length of the magnetised regions.

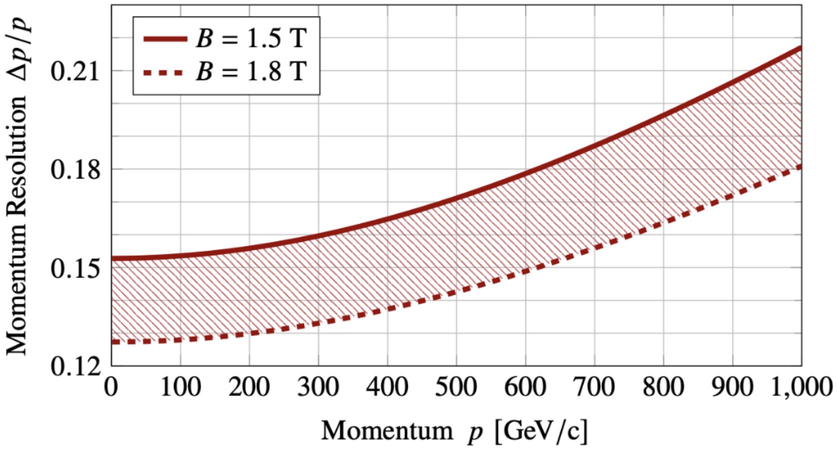

Figure 3.15: Muon momentum resolution as a function of the muon momentum, the region in the red band represents, the resolution achievable between $B = 1.5$ T and $B = 1.8$ T.

Given the space limitations on the HCAL's length, the distance between the two magnets, and the total system length, the focus can be placed on optimising the length of the muon system's magnet. The range of capabilities in terms of muon momentum resolution achievable by the spectrometer system is shown in Figure 3.15: spectrometers with fields in the range of 1.5 ÷ 1.8 T can achieve a resolution lower than 25 % for muon momenta up to 1 TeV/c.

The geometrical acceptance has been analysed to determine the optimal magnet aperture, once the magnetic flux density value was established. The optimal configuration was achieved by adapting the shape and cross-section of the magnets to match the expected angles of muon tracks originating from neutrino interactions while ensuring an overall geometrical acceptance of at least 90%. The geometrical acceptance was evaluated for various magnet aperture sizes, as illustrated in Figure 3.16. With the aperture of the HCM fixed at 60×60 cm^2, a geometrical acceptance of approximately 86% was achieved using a *pyramidal-frustum-shaped* MSM with upstream and downstream apertures of 70×70 cm^2 and 90×90 cm^2, respectively.

A greater acceptance — above 90% — is reached for muons from neutrinos originating from charm decays, which constitute the point of interest for the experiment. Given the essential characteristics of the magnets, specifically the aperture and magnetic flux density, the electromagnetic design process can proceed.

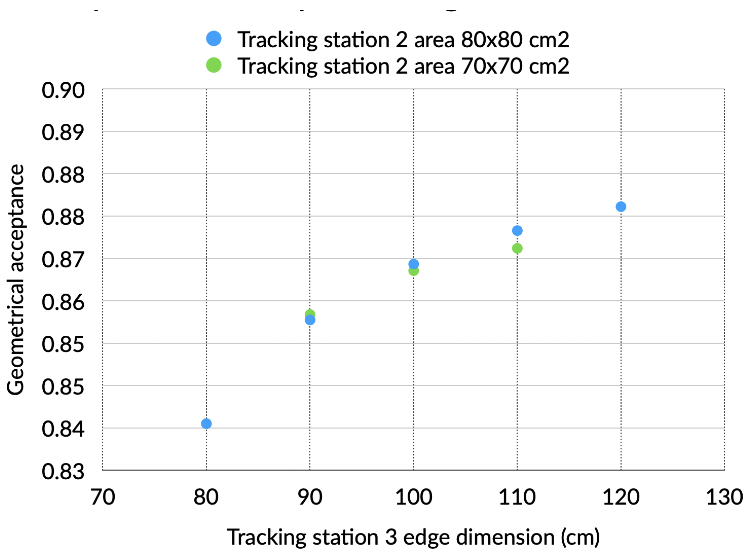

Figure 3.16: Geometrical acceptance as a function of the edge dimension of the most downstream tracking station of the spectrometer system, at fixed values of the tracking station 2 cross-section.

A slightly modified version of the Matlab tool was utilized to accommodate the distinctive shape of the MSM, which belongs to a novel class of magnets known as *flux-symmetric conical magnets* [16].

Referring to the notation in Figure 3.17, the flux balance equation is expressed as:

$$\bar{b}Bc = 2\bar{h}B_{\mathrm{ret}}c \tag{3.7}$$

where $\bar{a}$, $\bar{b}$, and $\bar{h}$ represent the average of the upstream and downstream dimensions of the magnet. The magneto-motive force NI required to obtain a flux density B in the core is approximately

$$\mathcal{F} = NI \approxeq \bar{a}\mathcal{H}(B) + \ell_{\mathrm{MSM}}\mathcal{H}\left(\frac{\bar{b}B}{2\bar{h}}\right) \tag{3.8}$$

where

$$\ell_{\mathrm{MSM}} = \bar{a} + 2\left(\frac{\bar{b}}{4} + t\right)$$

and $H = \mathcal{H}(B)$ defines the nonhysteretic nonlinear characteristic of the type of soft iron chosen for the yoke, that is in Figure 3.4. As a matter of fact, choosing a weakly saturated, still in non-linear region working point of $H \approx 9$ kA/m leads to $B \approx 1.7$ T.

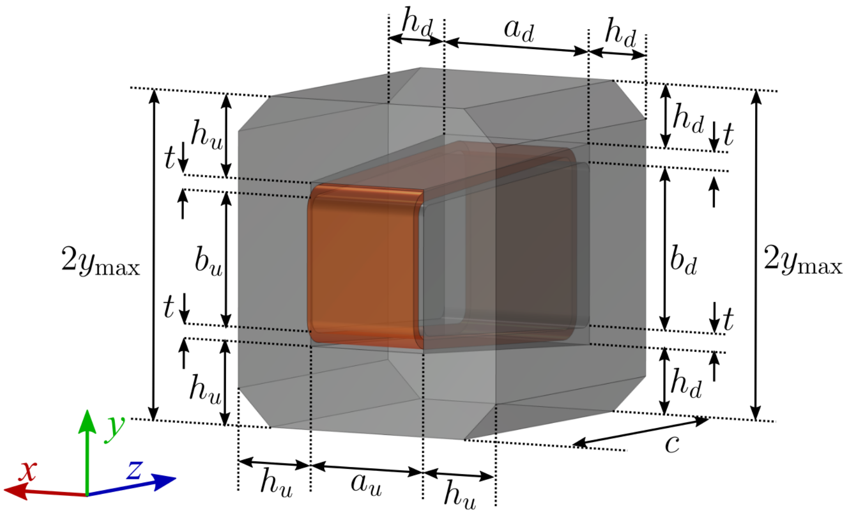

Figure 3.17: Three-dimensional model of the MSM design and definition of geometrical parameters, *u* and *d* pedices stand for "upstream" and "downstream", respectively.

Moreover, the approximate mean length per turn can be expressed as

$$l_t = b_u + b_d + 2c \qquad \text{for the MSM} \tag{3.9}$$

$$l_t = 2b + 2c \qquad \text{for the HCM} \tag{3.10}$$

which contributes to the electrical power consumption expression

$$P = \frac{\rho(T) l_t \mathcal{F}^2}{f a_u t} \tag{3.11}$$

Result

The set of constraints, goals and first insights into the basic parameters just provided results in an optimal design of the magnets summarised in Table 3.3. In particular, the coil of the MSM is made with 42 turns of copper, with a cross-section of 26×26 mm^2, this choice implies that the current density is sufficiently low so that air-cooling is possible. A cost-benefit analysis has been carried out, it must be noted that the choice of the core filled with iron, with the corresponding electrical power in the order of $1 \div 2$ kW, results in a negligible operational cost, especially if compared with the previous air-core solution. Therefore, only capital costs have been considered. The analysis approach is the same given in 2.1.1. the estimated costs for the spectrometer system magnets are summarised in Table 3.4.

Main magnet features	Value	Unit
Hadron Calorimeter Magnet		
Reference magnetic flux density	1.76	T
Total magnet length	2.54	m
Total cross-section	1.20×1.50	m^2
Core cross-section	0.60×0.60	m^2
Total power consumption	1.5	kW
Magneto-motive force	18.0	kA
Current density	0.75	A/mm^2
Stray field [@ iron surface]	$\lesssim 10$	mT
Total conductor mass	1.3	t
Total iron mass	22.5	t
Muon System Magnet		
Reference magnetic flux density	1.75	T
Total magnet length	1.60	m
Total cross-section	1.60×1.78	m^2
Core cross-section (upstream)	0.70×0.70	m^2
Core cross-section (downstream)	0.90×0.90	m^2
Total power consumption	1.5	kW
Magneto-motive force	21.0	kA
Current density	0.74	A/mm^2
Stray field [@ iron surface]	$\lesssim 10$	mT
Total conductor mass	1.25	t
Total iron mass	33	t

Table 3.3: Optimal design configuration obtained from 3D simulations after the optimisation procedure. A more detailed table is provided in [16].

	Unit cost	Units	Manufacturing factor	Cost
Hadron Calorimeter Magnet				
Coil (copper)	7.4/t	1.3 t	3	29
Magnetic structure (iron)	1.6/t	22.5 t	4	144
Muon System Magnet				
Coil (copper)	7.4/t	1.25 t	3	28
Magnetic structure (iron)	1.6/t	33 t	4	211
Total				412

Table 3.4: Cost estimates in kCHF for the magnets of the spectrometer system.

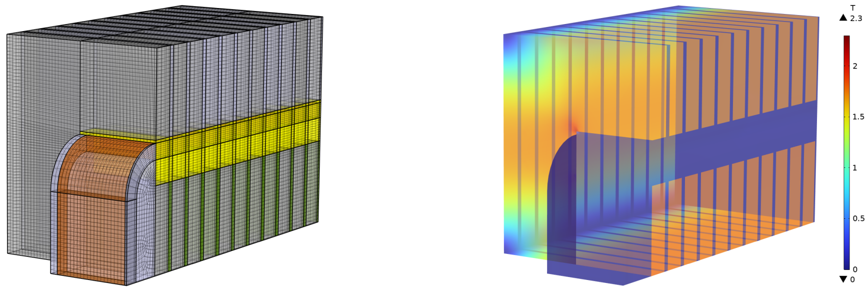

(a) (b)

Figure 3.18: 3-D view of the model used in COMSOL simulation corresponding to one-quarter of the whole HCM (a) and distribution of the modulus of magnetic flux density (b).

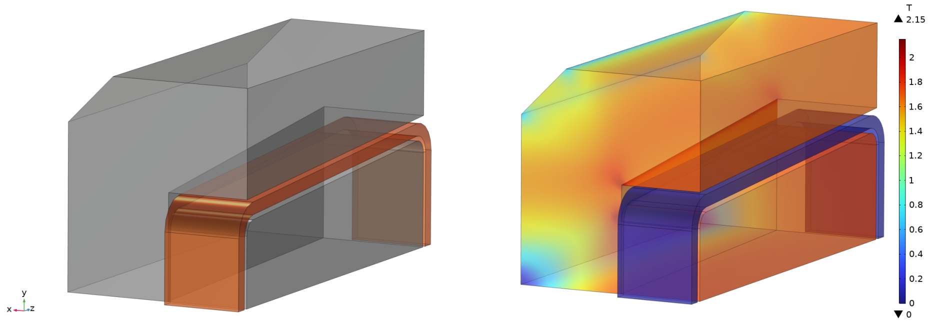

(a) (b)

Figure 3.19: 3-D view of the model used in COMSOL simulation corresponding to a one-quarter of the whole MSM (a) and distribution of the modulus of magnetic flux density (b).

As for the validation through numerical simulations, this has been carried out with COMSOL software as well and in order to reduce the computational load, the symmetry of the geometrical and physical problem has been exploited therefore only one-quarter of the whole structure has been modelled. Figure 3.18 and 3.19 show the 3D views of one-quarter of the whole magnet (a) and the modulus distribution of the magnetic flux density $|B|$. Whereas, in Figure 3.20 the 2-D distribution of the magnetic flux density norm $|B|$ within the magnet and the surrounding air domain in the $x - y$ plane is shown for the HCM (a) and for the MSM (b). In the active region, the average value of the magnetic flux density component along the x-axis is 1.75 T.

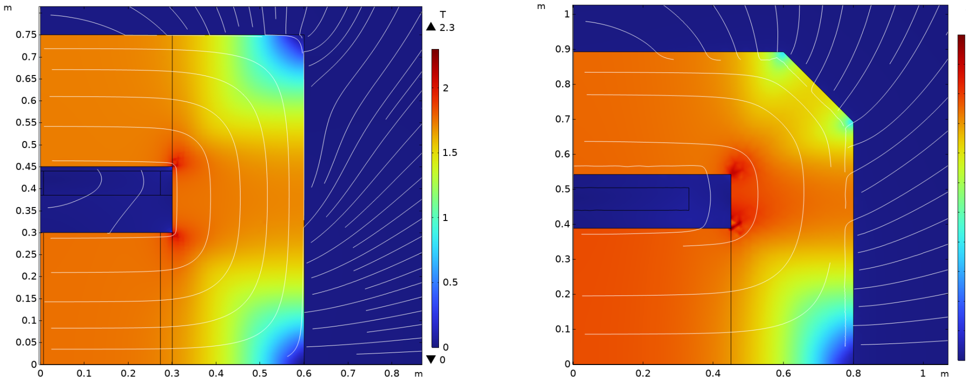

(a) (b)

Figure 3.20: 2-D mapping of the norm of the magnetic flux density $|B|$ for the HCM (a) and for the downstream part of the MSM (b).

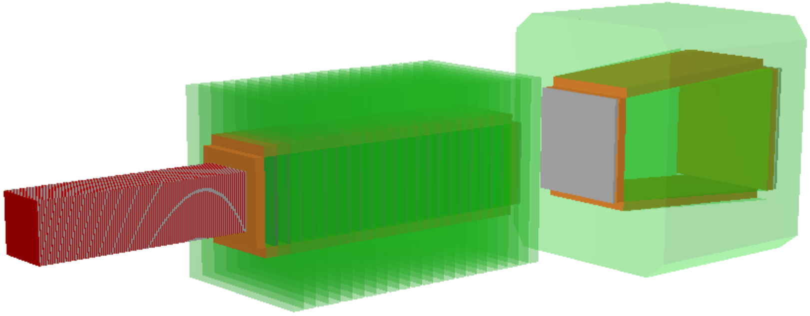

Figure 3.21: 3-D model implemented in the SND@LHC software framework, used in GEANT4 simulations.

A straightforward yet effective model of this layout, similar to the previous configuration, has been incorporated into the detector geometry within the SND@LHC software framework, as illustrated in Figure 3.21.The physics performance, in terms of muon charge identification efficiency and muon momentum resolution, has been evaluated. Figure 3.22 shows the distributions of the outgoing muons' angles in the x and y projection planes, based on neutrino simulations. The width of the fitted Gaussian distribution in Figure 3.22 (a) represents the angular resolution provided by the spectrometer, assuming a detector position resolution of 100 µm. Applying a 3σ cut on the bending angle θ_y distribution in Figure 3.22 (b) results in a muon charge identification efficiency of approximately 80%.

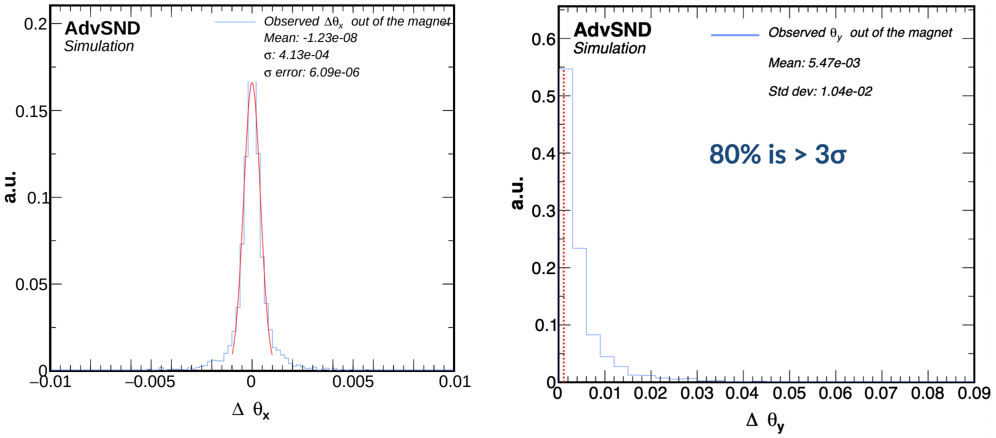

(a) (b)

Figure 3.22: Muon angle distribution in the x (a) and y (b) projections. The θ_x distribution has been fitted with a Gaussian, its width has been used to estimate the muon charge identification efficiency as about 80%.

The momentum of muons has been estimated using a slightly modified method from [45], and the muon momentum resolution has been assessed, as shown in Figure 3.23. An overall momentum resolution of 0.160 ± 0.001 was achieved, which is higher than that of the air core solution, primarily due to the contribution of multiple Coulomb scattering. However, a key advantage is that this resolution remains relatively constant with respect to the muon momentum, as illustrated in Figure 3.23 (b), therefore offering better performance than the air core solution when the hard part of the muon momentum spectrum is concerned.

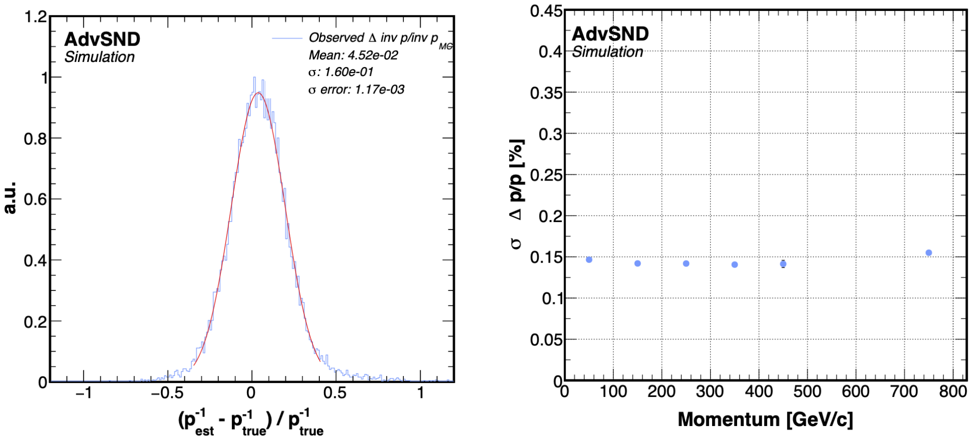

(a) (b)

Figure 3.23: Muon momentum resolution achievable by the spectrometer system as estimated by Geant4 simulation of ν_μ CC interactions in the target region: (a) overall and (b) as a function of the true momentum of the muon.

3.1.3 The compact solution

The latest — and currently proposed — configuration for the next upgrade of the SND@LHC experiment at the HL LHC aims to drastically reduce the civil engineering work required to install the apparatus in the TI18 tunnel. Earlier designs necessitated significant modifications to the tunnel structure, including changes to the floor and the re-routing of certain conduits, which resulted in considerable additional costs. The new configuration is far more compact, having reduced the magnetised area and eliminated the need for an iron-core magnet downstream, while still retaining a magnetised hadron calorimeter. While this solution requires limited excavation of the floor to meet specific boundaries, it offers the significant advantage of leaving the tunnel structure intact. However, exceeding these boundaries could affect the tunnel's stability, necessitating extensive excavation to restore the integrity of the concrete structures. Additionally, temporary mechanical reinforcements would be needed to maintain stability during construction. These structural concerns would make it impossible to meet the HL LHC's tight schedule. The key changes to the previous configuration are as follows:

- The detector has been raised by 10 cm, shortening the target region to remain within the structural safety limits for excavation and decreasing the HCAL's active cross-section to 40×40 cm^2.
- To maintain similar muon momentum resolution and charge identification, silicon modules have been proposed for the magnetised HCAL. These modules provide a resolution of 30 µm, a significant improvement over the $100 \div 150$ µm resolution of the previous trackers.

A schematic layout of the latest proposed configuration for the upgrade of the SND@LHC is illustrated in Figure 3.24 (a) and its integration in the TI18 tunnel [46], Figure 3.24 (b).

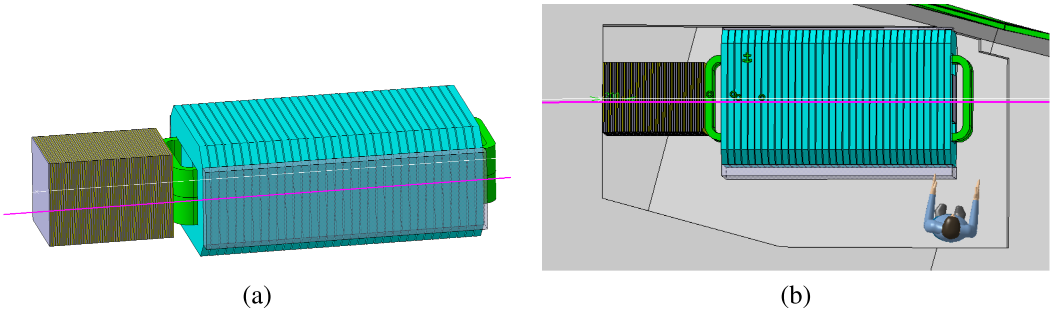

Figure 3.24: 3-D CAD model of the latest proposed layout of the compact version of the upgrade of the SND@LHC detector (a) and its integration in the TI18 tunnel (b).

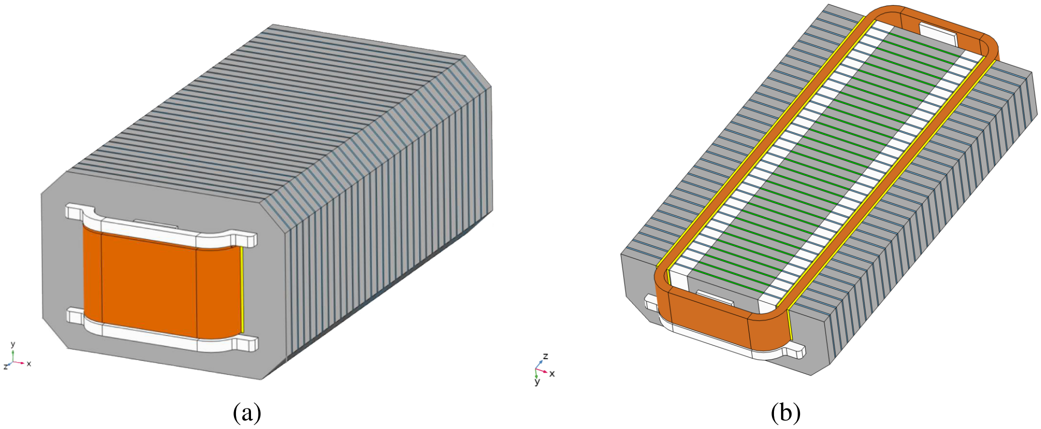

Figure 3.25: 3-D model of the compact solution of the upgrade of the SND@LHC experiment as simulated in COMSOL software.

The compact magnet design

In this configuration, no optimisation process has been performed, as the design of the previous HCM has been fully inherited, except for adjustments to its dimensions. Consequently, the numerical simulation model, along with the performance analysis in terms of geometrical acceptance and muon momentum resolution, will be discussed next.

Figure 3.25 shows a 3D model of the proposed electromagnetic design as implemented in a 3D COMSOL numerical simulation, alongside a section view that highlights various parts of the magnet. The design includes 34 magnetised iron slabs, each 5 cm thick, interleaved with 33 detector layers, each 0.8 cm thick. It is important to note that the coil has been rotated by 90 ° to reduce the space needed for the flux return yoke, resulting in a magnetic field oriented in the y-direction.

Main magnet features	Value	Unit
Reference magnetic flux density	1.75	T
Total magnet length	2.267	m
Total cross-section	1.15×0.8	m^2
Core cross-section	0.40×0.40	m^2
Total power consumption	1.19	kW
Magneto-motive force	13.0	kA
Current density	0.89	A/mm^2
Stray field [@ iron surface]	$\lesssim 21$	mT
Total coil mass	0.86	t
Total iron + s. steel	11.12	t

Table 3.5: Main features of the last configuration of the HCM for the SND@LHC upgrade obtained from 3D simulations.

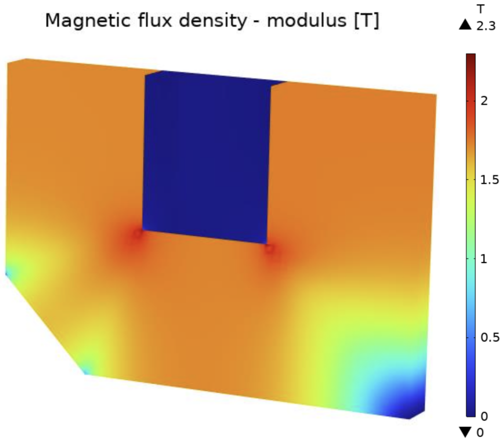

Figure 3.26: Distribution of the modulus of the magnetic flux density in the slab n.17.

To accommodate the electronics of the detectors between the magnetised iron slabs, additional space has been provided between the coil and the magnetised region. This space is filled with stainless steel slabs, as depicted in Figure 3.25 (b) in white, while the detector spaces are shown in green. Table 3.5 summarises the key features of the magnet design. A quarter of the entire magnet geometry has been simulated, and Figure 3.26 presents the distribution of the magnetic flux density modulus $|B|$ for a single iron slab, specifically slab 17, located near the middle of the magnet. The simulation demonstrates that a high degree of field uniformity is achieved within the active region.

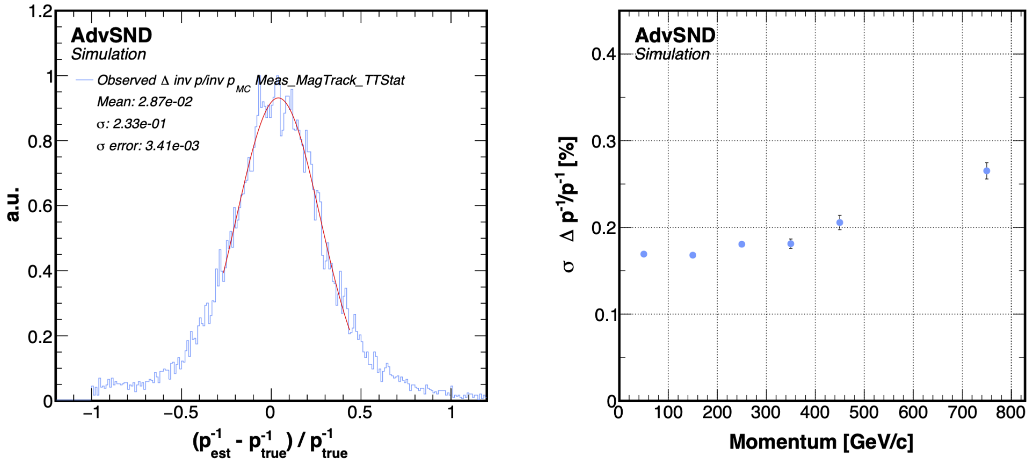

(a) (b)

Figure 3.27: Muon momentum resolution achievable by the compact solution of the SND@LHC upgrade as estimated by Geant4 simulation: overall (a) and as a function of the incoming muon momentum (b).

Regarding the physics performance, the shortening of the target and the reduction in transverse dimensions have inevitably impacted the geometrical acceptance, resulting in a 72% acceptance. Nevertheless, the muon momentum detection performance has been largely preserved. Muon momentum is estimated using the angular method, where the entry and exit angles of the muon are measured, allowing the momentum to be determined. The overall muon momentum resolution of 0.233 ± 0.003 is achieved, as depicted in Figure 3.27(a). Figure3.27 (b) further demonstrates a relatively constant trend in resolution with respect to the incoming muon momentum, even in this case.

3.2 The SND magnet of SHiP

The Search for Hidden Particles (SHiP) experiment is a general purpose fixed target facility proposed at the CERN *Super Proton Synchrotron* (SPS) whose primary goal is to search for new physics in the unexplored region of very weakly interacting particles at the intensity frontier using a 400 GeV/c proton beam impinging onto a high-density target.

The existence of particles such as dark photon, light scalars, Heavy Neutral Leptons (HNL) and axions will be therefore explored with unprecedented sensitivity in the GeV mass region. Furthermore, direct search for light dark matter (LDM) will be performed through the scattering off the atoms of the neutrino detector and tau neutrino physics will be studied. As a matter of fact, using the neutrino physics results from the SND@LHC experiment (and its upgrade), SHiP aims to perform the direct observation of the tau anti-neutrino and to study ν_τ and $\bar{\nu}_\tau$ cross-sections, alongside their properties thanks to its dedicated neutrino detector and to the beam dump facility (BDF) acting as a tau neutrino factory.

The SHiP design has gone through several changes since the original design from 2015 [12, 47] where it would have been served by a new, short, dedicated beam line in a new experimental cavern (ECN4) to the most recent one at the ECN3 [48].
As a matter of fact, the already existing ECN3 experimental facility makes it possible to implement the SHiP facility at a fraction of the cost of the original proposal, without compromising on the physics scope and the physics reach. The most recent setup of the SHiP experiment is shown in Figure 3.28 where two complementary detectors are foreseen: the upstream detector is designed for recoil signatures of LDM scattering and neutrino physics whereas the downstream detector system aims at measuring visible decays feebly interacting particles in a nearly background-free environment.

The high-intensity, high-energy proton beam at the BDF generates a powerful flux of neutrinos of all flavours – electron, muon, and tau neutrinos – as well as their corresponding anti-neutrinos. With a hadron absorber and muon shield effectively clearing the forward region of hadrons and muons, the SHiP experiment is optimally designed for neutrino physics studies. Positioned directly downstream of the muon shield, a compact detector utilising nuclear emulsion technology and a **muon spectrometer** enables the detection of all neutrino flavours and measurement of their energy.

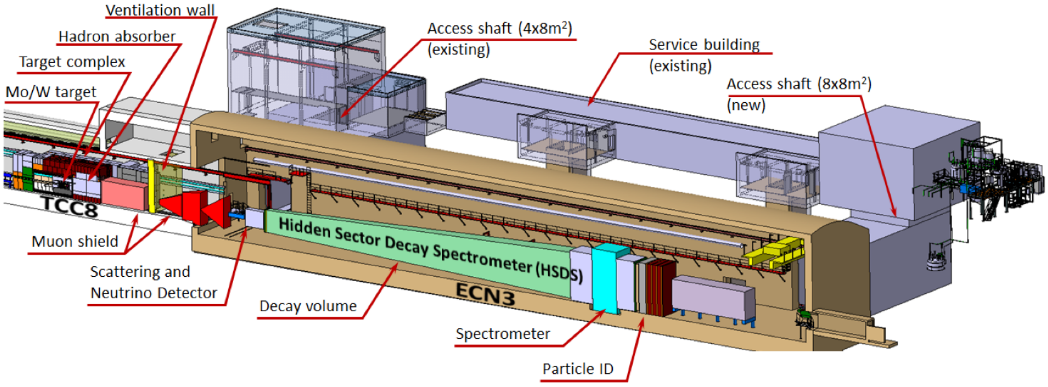

Figure 3.28: Overview of the SHiP experimental setup on the SPS TCC8/ECN3 experimental facility.

3.2.1 The original configuration and SND@ECN3

The original configuration of the neutrino detector of the SHiP experiment was included in the SHiP design at the ECN4, illustrated in Figure 3.29, it is placed in a region where most of charged particles, like muons are completely swept away by the upstream Muon Shield leaving neutral particles like neutrinos or Beyond Standard Model particles. The SND utilises a hybrid detector design, similar to the concept developed by the OPERA Collaboration [49].

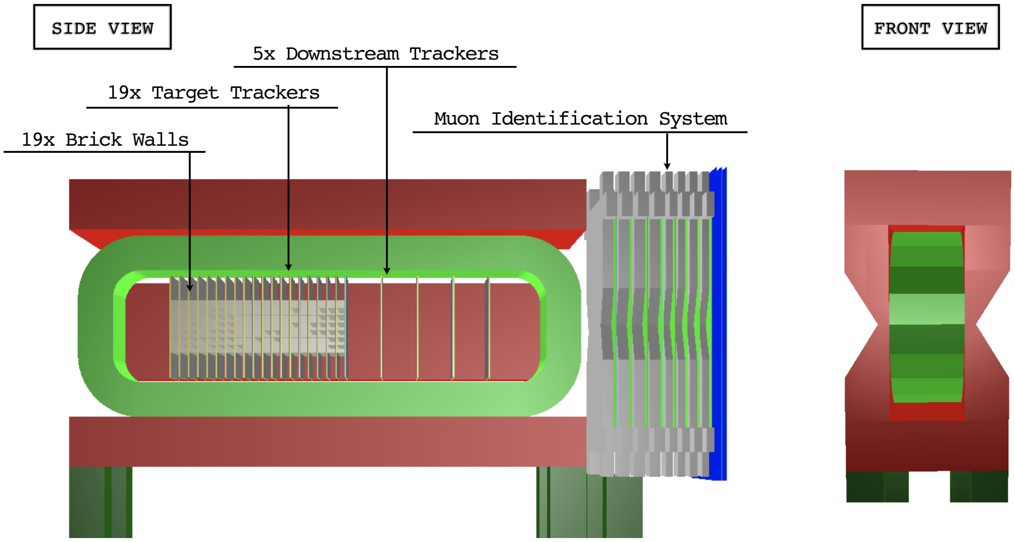

Figure 3.29: Original layout of the Scattering and Neutrino Detector of the SHiP experiment

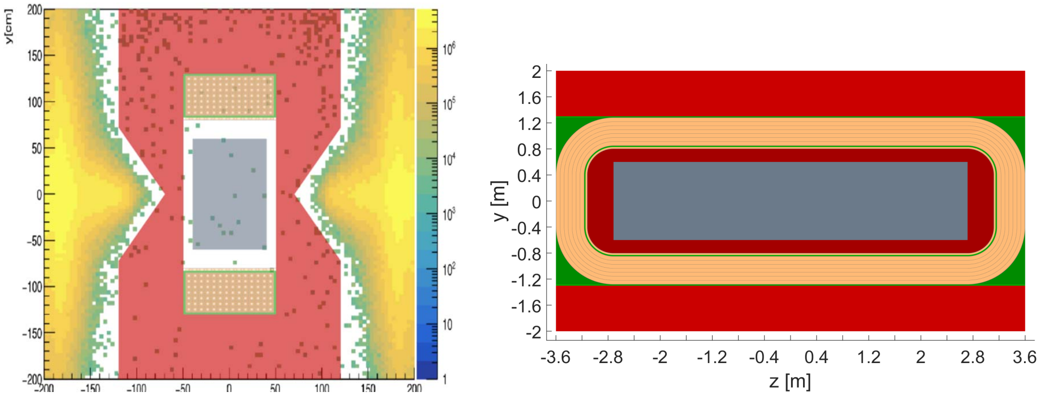

(a) (b)

Figure 3.30: Muon flux spatial distribution with the silhouette of the SND apparatus (a) and YZ projection sketch of the magnet conceptual design (b).

It alternates layers of nuclear emulsion films with high-density passive material, serving as a ν-target, along with electronic trackers. Additionally, the detector operates within a magnetic field, allowing for the charge and momentum measurement of hadronic final states.

The design

The SHiP SND magnet must be designed to provide a large, uniformly magnetised volume that can accommodate both the neutrino target and the spectrometer trackers. To achieve this, initial design constraints require the magnet to produce a field of at least 1.2 T over a volume of approximately 10 m^3, allowing for charge and momentum measurements of hadrons up to 10 GeV/c. Additionally, the magnet's stray field outside this region must be minimised to prevent interference with the muon flux, which is deflected by the muon shield. Figure 3.30 illustrates the region cleared from the muon flux where the apparatus should be placed as well as a sketch of the first conceptual design of the magnet. Moreover, the structure of the magnet must enable easy access for detector installation and maintenance, adding to the design complexity. For instance, the Compact Emulsion Spectrometer (CES) needs to be replaced every few weeks to limit integrated combinatorial background in track matching, essential for momentum measurements. This requirement requires the magnet to be designed for frequent and efficient opening.

Constraint	Value	Unit
Internal volume	$1 \times 1.6 \times 5.4$	m^3
Overall external size	$2.4 \times 4.0 \times 7.2$	m^3
Internal volume temperature	18	°C
Reference field	>1.2	T
Field homogeneity	≈ 1	%
External stray field	≤ 10	mT

Table 3.6: Main magnet design constraints.

Table 3.6 outlines the key design constraints, including a temperature limitation, which is due to the operating temperature requirements of the nuclear emulsion films used in the neutrino target. Given the design constraints for the magnet, optimisation options are limited. However, an analytical model has been developed, forming the initial version of the Matlab tool detailed in Sec.2.3. The analysis performed — thoroughly covered in [14] — focuses on identifying design solutions that satisfy both dimensional constraints and stray field requirements while minimising power. Once the iron yoke material, typically AISI 1010 as commonly used in this Ph.D. dissertation, has been specified, key scaling laws of the magnet's characteristics have been derived with the yoke thickness as a parameter.

Figure 3.31 illustrates the model's predictions on how efficiency, maximum iron flux density, power, magneto-motive force, and maximum stray flux density vary with yoke thickness h. These values are calculated assuming a reference magnetic flux density of $B = 1.2$ T. Notably, the power curve exhibits a minimum at a particular iron thickness, offering valuable insights for design. However, minimising both the stray field and power simultaneously presents a challenging trade-off.

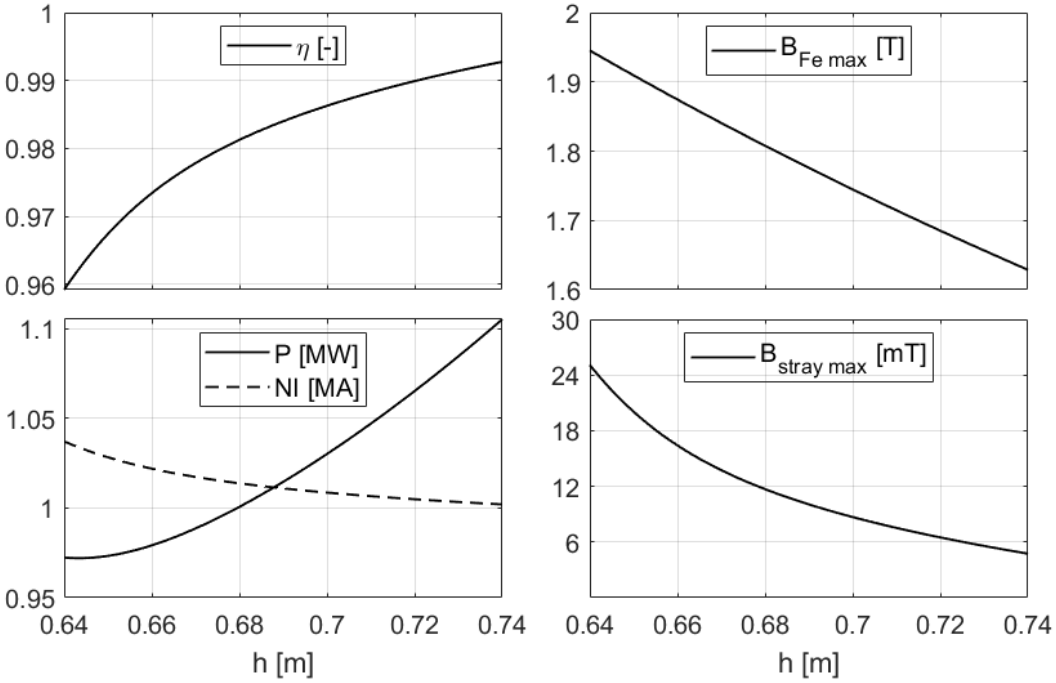

Figure 3.31: Main magnet features as a function of the iron yoke thickness

Result

The constraint on the maximum stray flux density is met with $h = 0.7$ m, resulting in a magnetic efficiency of approximately 99%, a power consumption of 1.03 MW, a magneto-motive force of 1.01 MA, and an iron flux density of 1.75 T. Consequently, the selected design configuration is detailed in Table 3.7. A 3-D analysis was also conducted using simulation software, confirming that all constraints are met and showing strong agreement with the analytical model, as shown in Table 3.8.

Main magnet features	Value	Unit
Reference magnetic flux density	1.75	T
Stray field [@ iron surface]	10	mT
Total power consumption	1.03	MW
Yoke thickness	70	cm
Coil thickness	50.1	cm
Coil fill factor	0.62	
Total iron mass	356	t
Magneto-motive force	1.014	MA
Current density	3.2	A/mm^2
Voltage	99	V
Total resistance	9.6	mΩ
Water speed	2.7	$m\cdot s^{-1}$
Reynolds number/1000	98	
Pressure drop	6.8	bar

Table 3.7: Reference design configuration of the magnet for the SND of the SHiP experiment.

		Analytic value	Numeric value
B_0	[T]	1.25	1.25
NI	[MA]	1.01	1.014
B_{Fe}	[T]	1.75	1.73
B_{stray}	[mT]	11	10

Table 3.8: Comparison between the main electromagnetic parameter values for analytic and FE numeric models.

Due to the symmetry only one eight of the entire structure is simulated, on the corresponding cut boundaries the symmetry condition is imposed, as well as the magnetic insulation at the external region boundaries. The FEM simulation for the set of used parameters is reported in Figure 3.32, where the modulus of the flux density $|B|$ is given in a 3-D view and 2-D section, respectively.

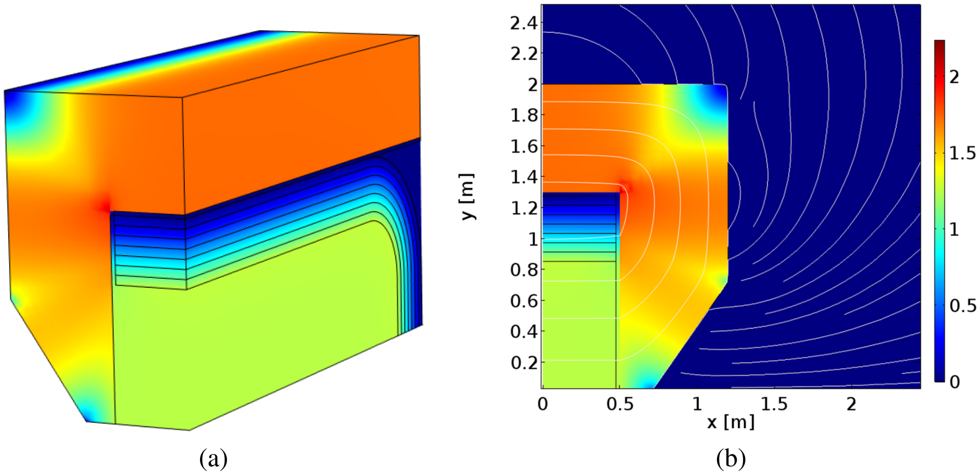

(a) (b)

Figure 3.32: Modulus of the flux density norm $|B|$ mapping within the magnet in the 3-D model (a) and outside in the 2-D view (b).

The SND magnet at the ECN3

The relocation of the SHiP experiment apparatus from ECN4 to the existing ECN3 facility required a complete revision of the experiment's layout. This displacement resulted in adjustments across multiple sections of the setup, involving relocation, shortening, or reduction to fit the SHiP detector fully within ECN3. Specifically, the muon shield in ECN3 now relying on a hybrid system of superconducting and normal-conducting magnets, moves the SND detector around 27 meters from the target center — 10.5 meters closer than initially planned for ECN4. Consequently, the new SND configuration spans approximately 6 meters in length.

This adjustment led to a complete rearrangement of the SND layout, adopting a configuration similar to that of the upgraded SND@LHC. The layout features a neutrino target region, equipped with emulsion cloud chamber (ECC) walls interleaved with target tracker planes, which provide time-stamping of interactions in the target. Downstream, a muon magnetic spectrometer housing four tracking stations within an air-core magnet, enables charge and momentum measurement for muons from muon-neutrino interactions. A schematic illustration is provided in Figure 3.33. However, unlike the SND@LHC upgrade, the SHiP SND spectrometer focuses on lower-momentum particles, reducing the requirements for both its length and bending power.

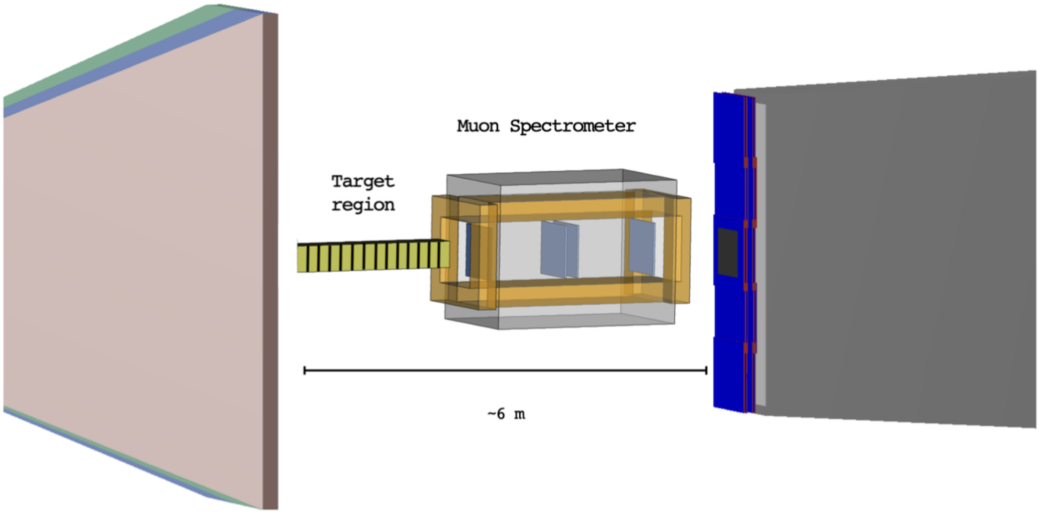

Figure 3.33: Schematic layout of the Scattering and Neutrino Detector (SND) at the SHiP experiment in the ECN3.

Main magnet features	Value	Unit
Total volume	$1.5 \times 2.2 \times 3.3$	m^3
Reference magnetic flux density	1	T
Total power consumption	0.7	MW
Total iron mass	50	t
Total coil mass	5	t
Estimated building cost	0.3	M€

Table 3.9: Reference design configuration of the magnet for the SND of the SHiP experiment at the ECN3.

In such a configuration, the space allowed for the magnet of spectrometer is about 3 m provided that the space required to house the full neutrino target is $\sim$ 2.6 m. Therefore, the process of optimisation of the magnet has relied on the experience gained with the design of the magnet for the upgraded SND@LHC, leading to a reference design summarised in Table 3.9. However, this design stage has not been extended to further detail as new proposals emerged. Nevertheless, this configuration served as a foundational reference in an optimization exercise, which is detailed in the following Section.

Requirements	
Maximum height	2.2 m
Maximum length	3.3 m
Active region section	0.8×1.0 m^2
Muon momentum resolution	≤ 0.25

Table 3.10: Constraints applied to the magnet design optimization for SND@SHiP magnet follow-up.

3.2.2 Power optimized SND magnet at ECN3

As a follow-up to such a design, an exercise has been carried out in order to explore the parameters' space in an exclusively analytical framework applying constraints on the available space and muon momentum resolution, as presented in Table 3.10 [50, 51]. The target of such an exercise is to provide the optimal point in a multi-objective approach which includes high physics performance, sustainability as well as possibly low total cost. This translates into jointly minimizing the particle momentum resolution, the power consumption and the used materials and electric energy, respectively. The set of analytical tools used in this exercise has been provided in Sec. 2.1.

After applying the constraints, some degrees of freedom are left, paving the way for the optimization process. A function of the coil thickness t and the iron yoke thickness h is used as running parameter since they are constrained by the maximum height of the magnet:

$$y_{\max} = 2(t + h) + b$$

where b is the vertical magnet aperture. The quantity $t/(t + h)$ — referred to as "copper-iron ratio" in the following — is indeed used as free parameter. The dependence of the main figures of the optimization procedure — such as power consumption, costs and efficiency — on the copper-iron ratio has been therefore explored, as shown in Figure 3.34. Interesting considerations can be given: in particular, the critical point where the magnet design becomes unbalanced is clearly visible, around $t/(t + h) \sim 0.55$, after this point the lack of the returning yoke becomes dominant (confirmed by the stray field trend) therefore the efficiency drops and quantities rocket. It is just at the edge of this situation that the optimal lies. Moreover, note that for a lifespan of 10 years, the operating cost is prevalent on the building cost.

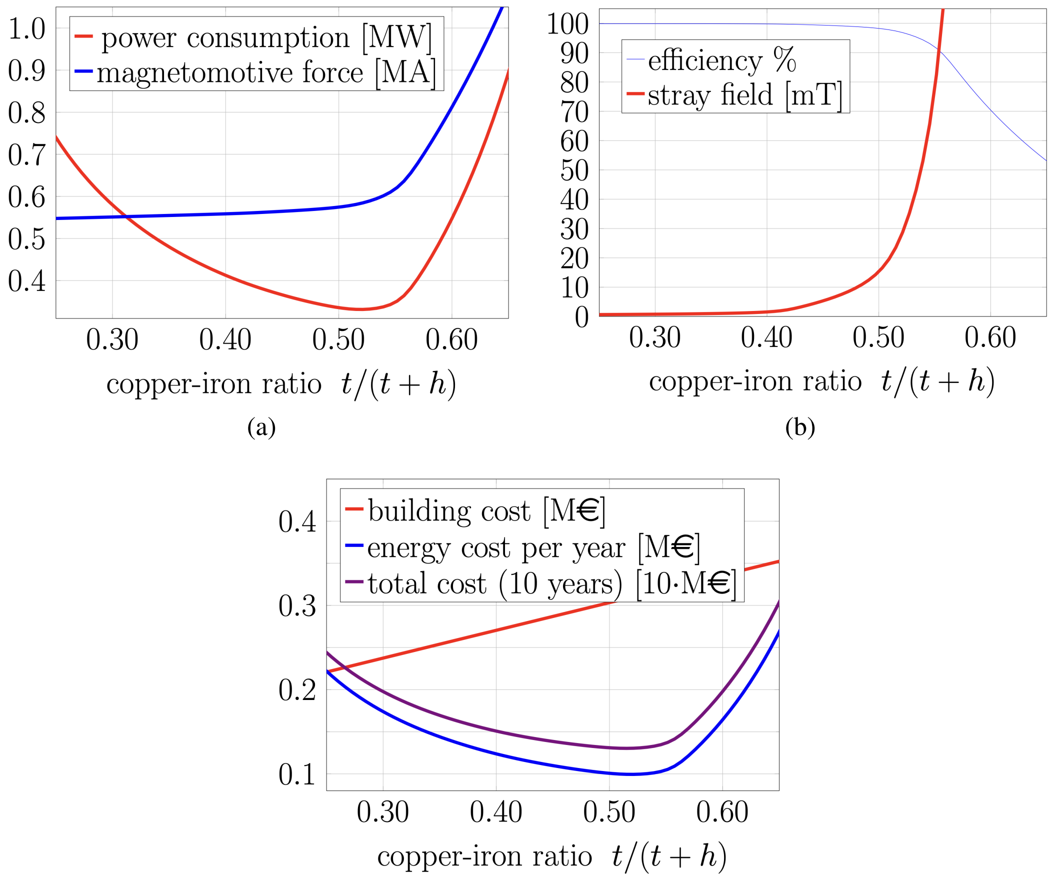

(a)

(b)

(c)

Figure 3.34: Dependence of magnet design's main figures of merit on the free parameter, copper-iron ratio $\frac{t}{t+h}$. Note in (c) that the total cost has been scaled by 10 for visualisation purposes.

Figure 3.35 provides a clear picture of the relationship between the particle momentum resolution and the required power consumption as functions of the copper-iron ratio. Depending on the particle momentum resolution the power minimum is achieved for different values of the ratio and, if the minimum for every particle momentum resolution value is considered, one can draw a line which represents all possible optimal solutions.

Remarkably, given the very critical dependence of the power need for the high-performance region (low particle momentum resolution), a factor **five** increase in power is needed to improve the resolution from 0.20 to 0.15.

In Table 3.11, the design configuration of one of the optimal points — corresponding to a particle momentum resolution of 0.25 — is summarized.

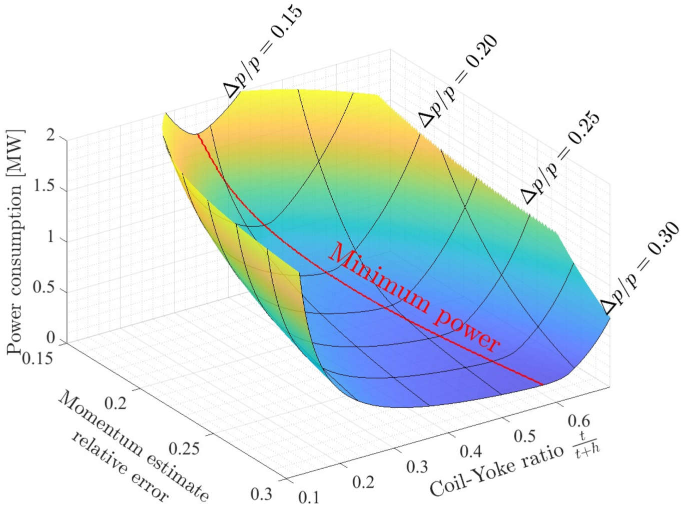

Figure 3.35: Power consumption and particle momentum resolution as functions of the free parameter, copper-iron ratio $\frac{t}{t+h}$. For a given particle momentum resolution, a line of power minima (in red) can be traced representing the design optimal points.

Main magnet features	Value	Unit
Coil-iron ratio	0.5212	
Reference magnetic flux density	0.89	T
Total power consumption	0.33	MW
Magneto-motive force	0.58	MA
Current density	3.4	A/mm^2
Stray field	28	mT
Magnet efficiency	0.9685	
Building cost	0.31	M€
Energy cost per year	0.10	M€
Total cost (10-years life)	1.3	M€

Table 3.11: Design configuration of the magnet in the optimal design as result of the optimization procedure.

3.2.3 Integration of the SND into the SHiP Muon Shield

To further optimise the space within the SHiP layout, integration of the SND detector layout within the upstream Muon Shield is under investigation. This approach leverages the existing magnetic field and constitutes part of the ongoing studies. Preliminary results from these investigations are presented below.

The muon shield is a crucial component of the SHiP experiment. Muons produced in proton-target interactions upstream can increase occupancies in the SND detector and may interact with matter, leading to false signals mimicking decays of BSM particles within the SHiP setup. Therefore, the muon shield is designed to either deflect or absorb these muons. An alternate-polarity scheme has been proposed and developed for the SHiP muon shield [52]. The operating principle of this scheme is illustrated in Figure 3.36 (a). High-energy muons are initially deflected by the core of the first section (set to a specific polarity) and then continue to be redirected by the return field in the yoke of the second section (with opposite polarity). On the other hand, mid-momentum muons are refocused by the return field in the first section, guiding them onto the yoke of the second section, where they are deflected back outward. Consequently, the muon shield splits positive and negative muons from the target into two distinct plumes on either side — as shown in Figure 3.36 (b) — creating a central region ideal for low-background experiments, as the SND. This design suppresses the muon rate in the SHiP detector by approximately six orders of magnitude.

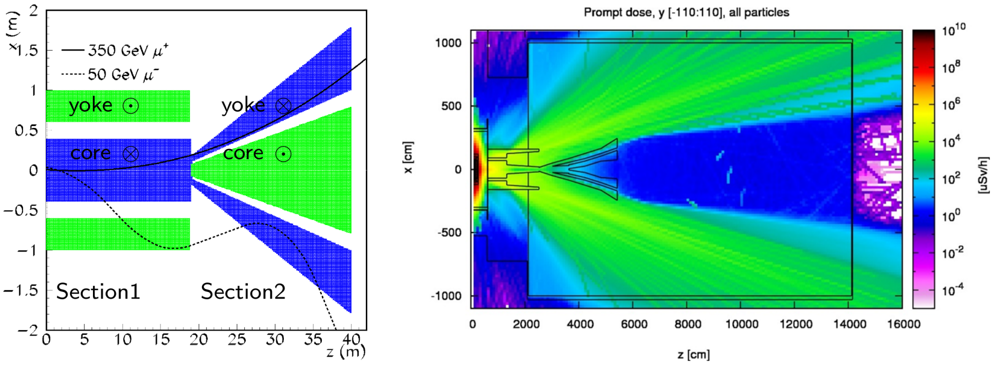

(a) (b)

Figure 3.36: Principle of the SHiP muon shield's alternate-polarity scheme (a): green and blue colors represent the field polarity in the iron. Expected prompt dose — primarily from muons — at the SHiP experiment (b); the blue area highlights the cleared region suitable for positioning the SND detector.

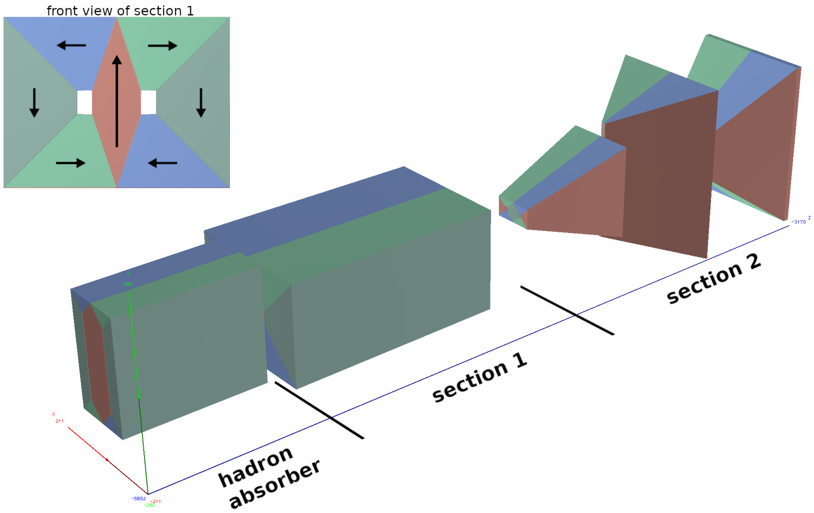

Figure 3.37: Geometry of the hybrid SC/NC muon shield configuration: the top-left figure illustrates the colour code for magnetic field orientation. The leftmost component of the shield represents the magnetised hadron absorber, followed by the SC magnet of section 1, and finally, the last three components are the NC magnets in section 2, set to the opposite polarity.

The muon shield's design was refined using a Bayesian machine-learning algorithm [53], which tested thousands of configurations, ultimately yielding optimized shapes with significantly reduced iron mass while maintaining shield performance. Given the proposal to implement the SHiP experiment at the existing ECN3 facility, further studies were conducted to adapt the layout to this new setting. As a result, the focus at ECN3 has shifted to a hybrid scheme using both superconducting (SC) and normal conducting (NC) magnets, with an SC magnet in section 1 followed by three NC magnets with opposing polarity. These magnets consist of seven iron volumes, each featuring a field with a fixed orientation and constant amplitude, as shown in Figure 3.37. All iron volumes maintain a field strength of 1.7 T, except for the core volume of the SC magnet, which has a fixed vertical field of 5.1 T. The integration of the SND detector in the muon shield has been focused on the last section of the muon shield, namely sections 2-3 and 2-4. Different exercises have been carried out — exclusively with 3-D numerical simulations — in order to assess the impact of the presence of the SND within the muon shield, exploring different scenarios, based on possible configurations of the SND layout, starting from the one proposed for the compact solution of the upgraded SND@LHC [54].

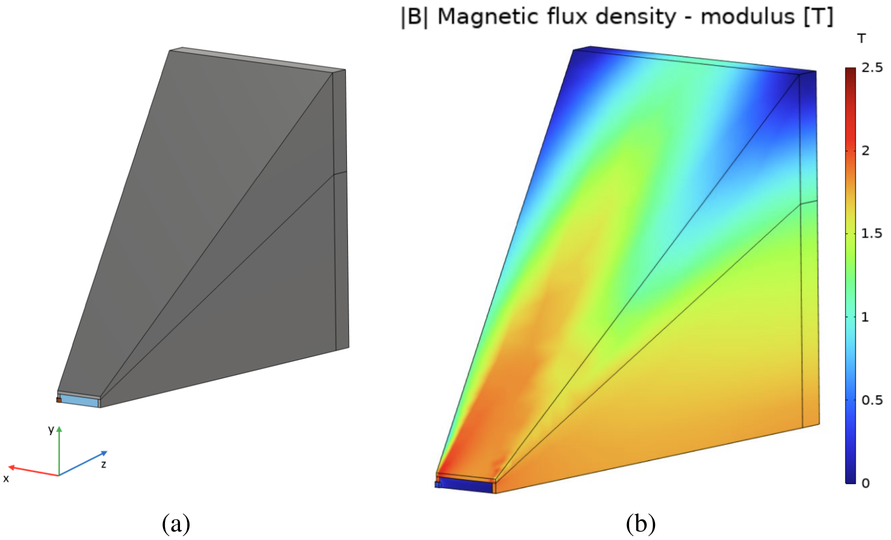

(a) (b)

Figure 3.38: 3-D models from the numerical simulation, one-quarter has been simulated (a), distribution of $|B|$ in the muon shield section model without the SND implementation.

As a reference geometry, one-quarter of the sections 2-3 2-4 of the muon shield has been simulated. The simulated model as well as the modulus of the magnetic flux density distribution are presented in Figure 3.38. Reference figures of merit can be considered, i.e. the magneto-motive force, the magnetic flux density value along y in the active region and the bending power taken as $\int_z |B_y| dl$, whose values are 53.6 kA, 1.684 T and 6.889 T m respectively.

Baseline layout

The first exercise has involved the implementation of a simple SND layout made up of 20 detector planes — modelled as air gaps, 20 mm thick — interleaved by 20 iron slabs, 50 mm thick with an active area of 40×40 cm^2, as illustrated in Figure 3.39. The 3-D field map is illustrated in Figure 3.40 (a) where no significant changes in the field distribution can be observed, indeed the magneto-motive force has been kept constant whereas variations of 0.3 % and 7 % occur for the magnetic flux density and the bending power in the active region, respectively. Figure 3.40 (b) illustrates the detail of the field distribution within the SND detector: 1.874 T and 23.9 mT are observed in the iron and in the air gaps respectively, taken as the mean value.

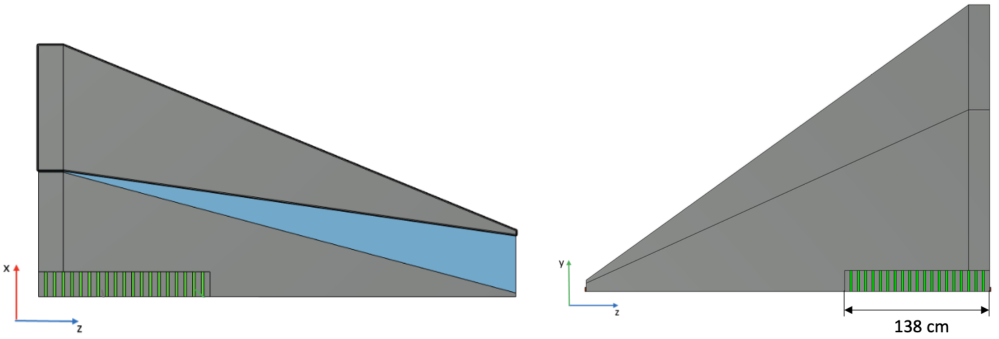

(a) (b)

Figure 3.39: First integration exercise of the SND layout with 20 iron slabs and 20 detector planes as seen in $x - z$ (a) and $y - z$ (b) projections.

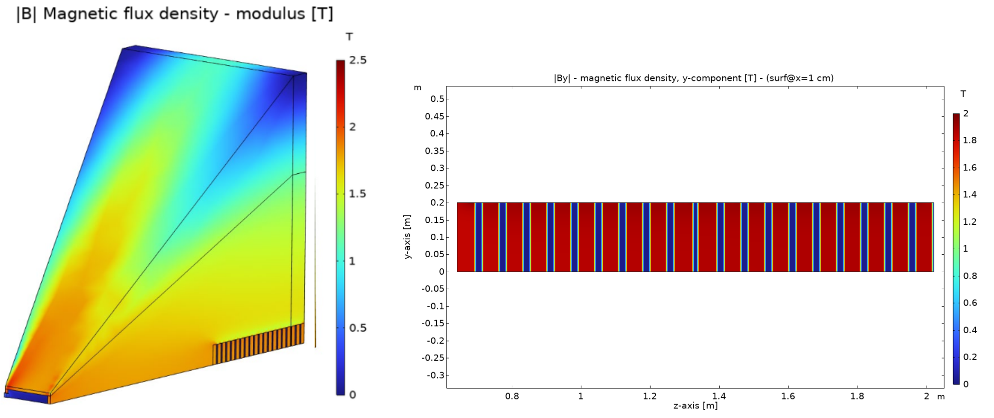

(a) (b)

Figure 3.40: 3-D distribution of the quantity $|B|$ in the muon shield section with the integration of the first SND layout (a); a detailed view of the magnetic flux density along y distribution in the SND detector (b).

Double SND detector layout

The second exercise has doubled the number of iron slabs and detector planes of the SND layout, keeping the active surface untouched, illustrated in Figure 3.41. Even in this case no "show-stopper" variations are observed, in particular a magnetic flux density of 1.668 T and a bending power of 5.84 T m are reached, Figure 3.42 (a). As far as the SND detector is concerned, the magnetic flux density value in the iron slabs results in 1.909 T whereas 29.2 mT are reached in the air gaps, as in Figure 3.42 (b).

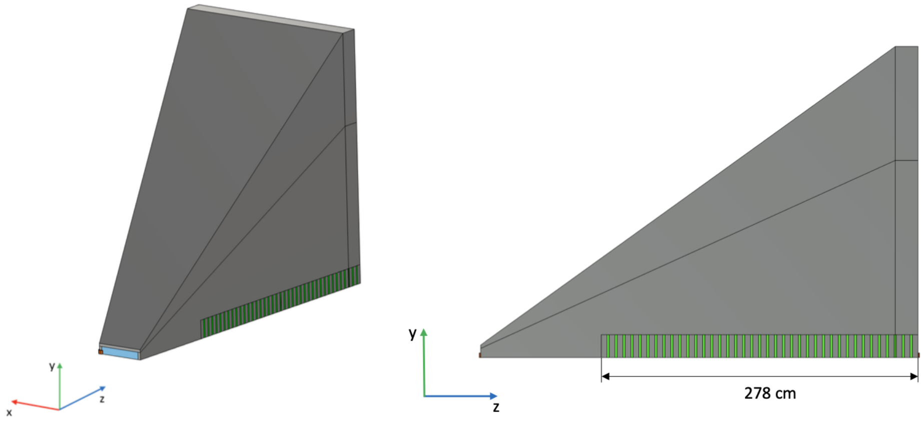

(a) (b)

Figure 3.41: Second layout integration in the muon shield as modelled in 3-D simulations: perspective view (a) and $y - z$ projection (b).

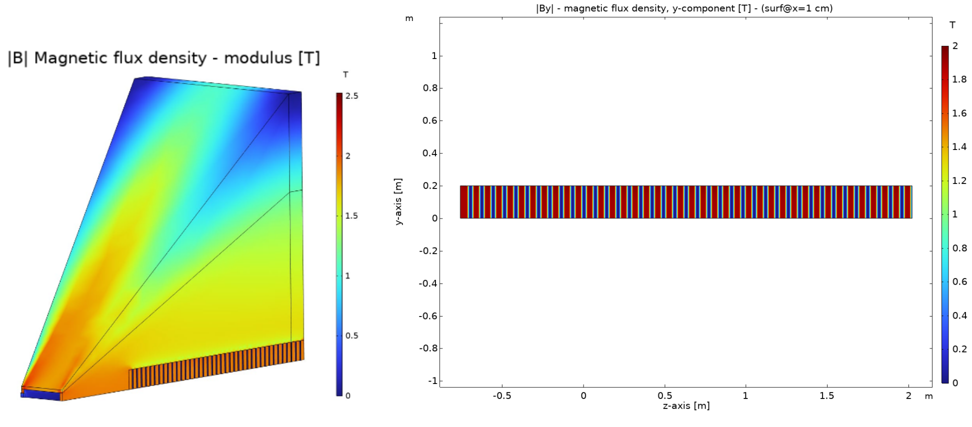

(a) (b)

Figure 3.42: 3-D distribution of the quantity $|B|$ in the muon shield section with the integration of the second doubled SND layout (a); a detailed view of the magnetic flux density along y distribution in the SND detector (b).

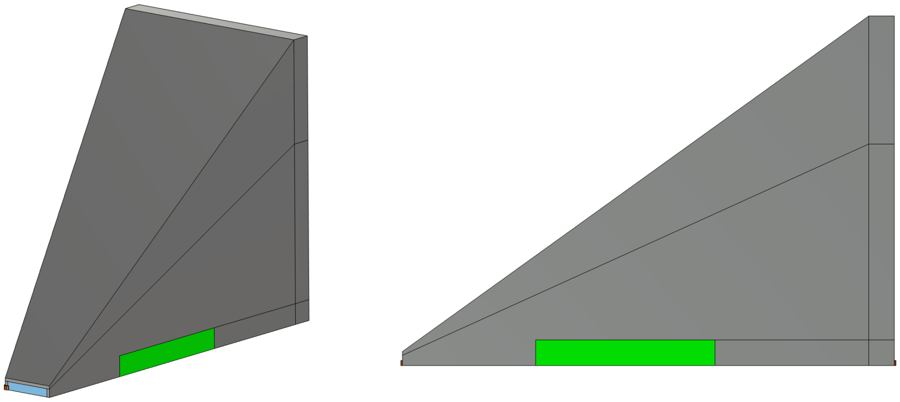

(a) (b)

Figure 3.43: Second layout integration in the muon shield as modelled in 3-D simulations: perspective view (a) and $y - z$ projection (b).

Double SND detector layout (compact)

The last exercise took into account the possibility of having a SND layout made up of a region with detector planes only alongside a compact iron bulk region downstream. This translates into having a 140 cm long air gap followed by a 140 cm long magnetised iron region, as illustrated in Figure 3.43. In this case, the field distribution visually changes in the active region leading to a magnetic flux density value of 1.636 T and a bending power of 4.85 T m. In particular in the region of the SND, the magnetic field within the iron is 1.919 T whereas a 60.5 mT magnetic field in the air-modelled region, as in Figure 3.44 (b).

Table 3.12 summarises the outcome of the three exercises compared with the reference layout without the SND integration.

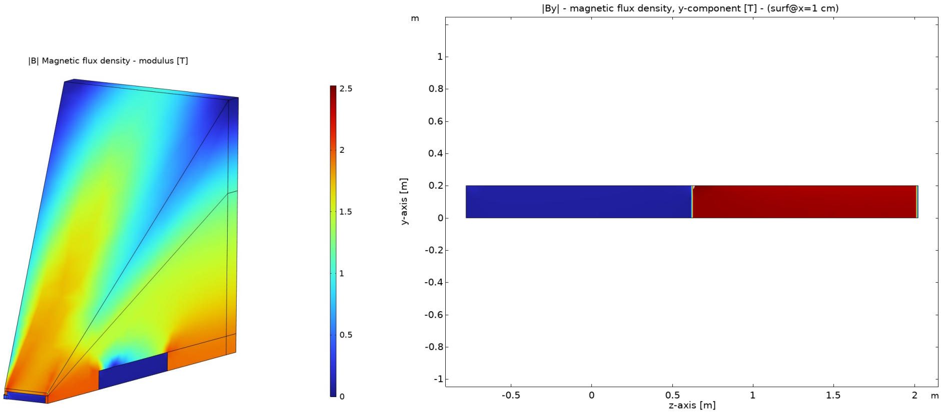

(a) (b)

Figure 3.44: 3-D distribution of the quantity $|B|$ in the muon shield section with the integration of the second doubled SND layout (a); a detailed view of the magnetic flux density along y distribution in the SND detector (b).

Configuration	MS Feature	Value	
Pure iron core	Magneto-motive force	[kA]	53.6
	Magnetic flux density	[T]	1.684
	Bending power	[T m]	6.889
Starting point	Magneto-motive force	[kA]	53.6
	Magnetic flux density	[T]	1.678
	Bending power	[T m]	6.371
Double SND layout	Magneto-motive force	[kA]	53.6
	Magnetic flux density	[T]	1.669
	Bending power	[T m]	5.84
Double SND layout (compact)	Magneto-motive force	[kA]	53.6
	Magnetic flux density	[T]	1.636
	Bending power	[T m]	4.85

Table 3.12: Different scenarios for the integration of the SND detector within the SHiP Muon Shield

CONCLUSION

This Ph.D. work has explored the complex yet essential task of designing magnets for particle detectors in High Energy Physics, focusing on advancing traditional design methodologies toward a more sustainable, energy-efficient approach.

By addressing the limitations of the traditional step-by-step design approach, this work has proposed an integrated framework that gives equal consideration to performance, cost, and sustainability factors. This shift in design philosophy is increasingly relevant as climate change and resource scarcity push for more energy-efficient solutions in all scientific as well as industrial domains, including HEP. Through a revised mathematical formulation and the development of analytical and numerical tools, this Ph.D. work has contributed to indicate a pathway to optimizing magnet design with a particular focus on minimizing power consumption.

The selection and development of proper analytical and semi-analytical models, validated by numerical tools, offer a robust framework for the early phases of magnet design. They have been integrated into a dedicated Matlab tool created within the Electrical Engineering group involved in the SHiP and SND@LHC Collaborations. This tool highlights the practical benefits of the integrated design approach, showing how it can simplify the design process while pursuing detection performance and efficiency at the same time.

Some contributions to the design of magnetic spectrometers for the SND@LHC and SHiP experiments are reported, demonstrating — where possible — the tangible improvements achievable through this approach.

In particular, three different design proposals have been analysed for both SND@LHC and SHiP experiments, whose main characteristics along with their strength and critical points have been highlighted.
Remarkably, some of these have materialized in published papers and conference posters whereas others have played a role in the feedback loop within the Collaborations, forming the basis for more advanced designs.

In summary, this work contributes a significant step toward sustainable magnet design in particle physics, setting a foundation for future research and development in designing high-performance, energy-efficient magnets for cutting-edge physics experiments.

BIBLIOGRAPHY

[1] **CMS Collaboration**, S. Chatrchyan et al., *The CMS Experiment at the CERN LHC*, *JINST* **3** (2008) S08004.

[2] B. Curé et al., *Fifteen Years of Operation of the Compact Muon Solenoid Detector Superconducting Magnet*, *IEEE Trans. Appl. Supercond.* **34** (2024), no. 5 1–8.

[3] **ATLAS Collaboration**, G. Aad et al., *The ATLAS Experiment at the CERN Large Hadron Collider*, *JINST* **3** (2008), no. 08 S08003.

[4] **ALICE Collaboration**, K. Aamodt et al., *The ALICE experiment at the CERN LHC*, *JINST* **3** (2008) S08002.

[5] F. Wittgenstein et al., *Construction of the L3 Magnet*, pp. 130–135. Springer, Dordrecht, 1990.

[6] **LHCb Collaboration**, A. A. Alves, Jr. et al., *The LHCb Detector at the LHC*, *JINST* **3** (2008) S08005.

[7] G. de Rijk, *Warm Magnets*, in *CAS - CERN Accelerator School 2019: Introduction to Accelerator Physics*, 7, 2021. [`arXiv:2107.03965`].

[8] T. Zickler, *Basic design and engineering of normal-conducting, iron-dominated electromagnets*, in *CERN Accelerator School: Course on Magnets*, 3, 2011. [`arXiv:1103.1119`].

[9] T. Roser et al., *Sustanability considerations*, in *European Strategy for Particle Physics - Accelerator R&D Roadmap*, p. 245. 2022.

[10] Y. Iwasa, *Case studies in superconducting magnets: design and operational issues*. Springer science & business media, 2009.

[11] A. Devred et al., *Proof-of-Principle of an Energy-Efficient, Iron-Dominated Electromagnet for Physics Experiments*, *IEEE Transactions on Applied Superconductivity* **34** (2024), no. 5 1–7.

[12] **SHiP Collaboration**, C. Ahdida et al., *The SHiP experiment at the proposed CERN SPS Beam Dump Facility*, *Eur. Phys. J. C* **82** (2022), no. 5 486, [`arXiv:2112.01487`].

[13] A. Ballarino et al., *Status of MgB_2 wire and cable applications in Europe*, *Journal of Physics: Conference Series* **871** (2017), no. 1 012098.

[14] **SHiP Collaboration**, M. de Magistris et al., *The magnet of the scattering and neutrino detector for the SHiP experiment at CERN*, *JINST* **15** (01, 2020) P01027.

[15] D. Centanni et al., *Power-Efficient Design of Large-Aperture Magnets for High-Energy Physics*, *Sustainability* **15** (2023), no. 14.

[16] **SND@LHC Collaboration**, D. Abbaneo et al., *An integrated flux-symmetric spectrometer-magnet system for the SND@LHC experiment upgrade*, *JINST* **19** (2024), no. 12 P12002.

[17] V. Scalera et al., *Advanced SND@LHC Magnet Design: New Options Design*, 2022. SND@LHC 11th Collaboration Meeting.

[18] D. Tommasini, *Practical Definitions and Formulae for Normal conducting Magnets*, tech. rep.

[19] M. A. Green et al., *Cost optimization of msu conventional room temperature magnets as a function of magnet conductor current density*, *IEEE Transactions on Applied Superconductivity* (2012) 4002504–4002504.

[20] S. Sgobba, *Physics and measurements of magnetic materials*, in *CERN Accelerator School: Course on Magnets*, 3, 2011. [`arXiv:1103.1069`].

[21] S. Arjuna Rao et al., *Prominence of Magnetic Properties in Grain Oriented and Non-Grain Oriented Steels for Transformer Industry*, *pr* **9** (Mar, 2013) 147–156.

[22] A. Saito et al., *Magnetization properties and domain structures of grain-oriented silicon steel sheets due to bending stress*, *IEEE Transactions on Magnetics* **36** (2000), no. 5 3078–3080.

[23] H. Hagihara et al., *Magnetic Properties Evaluation of Grain-Oriented Electrical Steel Sheets Under Bending Stress*, *IEEE Transactions on Magnetics* **50** (2014), no. 4 1–4.

[24] L. Rolandi et al., *Particle Detection with Drift Chambers*. Particle Acceleration and Detection. Springer, 2008.

[25] H. Spieler, *Semiconductor Detector Systems*, vol. v.12 of *Semiconductor Science and Technology*. Oxford University Press, Oxford, 2005.

[26] **OPERA Collaboration**, N. Agafonova et al., *Measurement of the atmospheric muon charge ratio with the OPERA detector*, *Eur. Phys. J. C* **67** (2010) 25–37, [`arXiv:1003.1907`].

[27] **SND@LHC Collaboration**, G. Acampora et al., *SND@LHC: the scattering and neutrino detector at the LHC*, *JINST* **19** (2024), no. 05 P05067, [`arXiv:2210.02784`].

[28] W. R. Leo, *Passage of Radiation Through Matter*, pp. 17–68. Springer Berlin Heidelberg, Berlin, Heidelberg, 1994.

[29] C. Grupen and B. Schwartz, *Particle Detectors*. Cambridge Monographs on Particle Physics, Nuclear Physics and Cosmology. Cambridge University Press, 7, 2023.

[30] W. S. Parzefall, *A Muon Spectrometer for SND@LHC*, 2022. Private note.

[31] **SND@LHC Collaboration**, V. Scalera, *Analytical Tools for the Evaluation of the AvdSND FAR Magnetic Spectrometer Performance*, tech. rep., 2024.

[32] R. Albanese and G. Rubinacci, *Magnetostatic field computations in terms of two-component vector potentials*, *International Journal for Numerical Methods in Engineering* **29** (1990), no. 3 515–532.

[33] P. P. Silvester and R. L. Ferrari, *Finite Elements for Electrical Engineers*. Cambridge University Press, 3 ed., 1996.

[34] J. P. A. Bastos and N. Sadowski, *Magnetic materials and 3D finite element modeling*. CRC press, 2017.

[35] "The AC/DC Module of COMSOL Multiphysics©." `https://www.comsol.com/acdc-module`. Accessed: October 2024.

[36] **GEANT4 Collaboration**, S. Agostinelli et al., *GEANT4 – A simulation toolkit*, *Nucl. Instrum. Meth. A* **506** (2003) 250–303.

[37] G. Battistoni et al., *Overview of the FLUKA code*, *Annals of Nuclear Energy* **82** (2015).

[38] T. Böhlen et al., *The FLUKA Code: Developments and Challenges for High Energy and Medical Applications*, *Nuclear Data Sheets* **120** (2014).

[39] C. Andreopoulos et al., *The GENIE Neutrino Monte Carlo Generator: Physics and User Manual*, [`arXiv:1510.05494`].

[40] **SND@LHC Collaboration**, D. Abbaneo et al., *AdvSND, The Advanced Scattering and Neutrino Detector at High Lumi LHC Letter of Intent*, tech. rep., CERN, Geneva, 2024.

[41] **SND@LHC Collaboration**, R. Albanese et al., *Observation of Collider Muon Neutrinos with the SND@LHC Experiment*, *Phys. Rev. Lett.* **131** (2023), no. 3 031802, [`arXiv:2305.09383`].

[42] **SND@LHC Collaboration**, R. Albanese et al., *Measurement of the muon flux at the SND@LHC experiment*, *Eur. Phys. J. C* **84** (2024), no. 1 90, [`arXiv:2310.05536`].

[43] S. Myers, *Particle Physics Reference Library: Volume 3: Accelerators and Colliders*, vol. 3. Springer Nature, 2020.

[44] "London metal exchange." `https://www.lme.com/en/Metals/Non-ferrous/LME-Copper#Price+graphs`. Accessed: 2022-06-09.

[45] W. S. Parzefall, *New concept for the magnetic spectrometer*, 2022. SND@LHC 10th Collaboration Meeting.

[46] L. Krzempek, *Integration study of the compact Advanced SND experiment in TI18*, 2024. LHC-X1SND-EN-003-EDMS 3153508.

[47] **SHiP Collaboration**, M. Anelli et al., *A facility to Search for Hidden Particles (SHiP) at the CERN SPS*, [`arXiv:1504.04956`].

[48] **SHiP Collaboration**, R. Albanese et al., *BDF/SHiP at the ECN3 high-intensity beam facility*, tech. rep., CERN, Geneva, 2023.

[49] **OPERA Collaboration**, R. Acquafredda et al., *The OPERA experiment in the CERN to Gran Sasso neutrino beam*, *Journal of Instrumentation* **4** (2009), no. 04 P04018.

[50] D. Centanni, *Sustainable design of larger aperture magnets for High Energy Physics and Medical Diagnostics*, 2023. Trends in Magnetism (TMAG) 2023, poster.

[51] D. Centanni, *Sustainability-oriented approach to the design of large aperture magnets for High Energy Physics and Medical Diagnostics*, 2024. International Conference on Magnetism (ICM) 2024, poster.

[52] **SHiP Collaboration**, A. Akmete et al., *The active muon shield in the SHiP experiment*, *JINST* **12** (2017), no. 05 P05011, [`arXiv:1703.03612`].

[53] **SHiP Collaboration**, A. Baranov et al., *Optimising the active muon shield for the SHiP experiment at CERN*, *J. Phys. Conf. Ser.* **934** (2017), no. 1 012050.

[54] V. P. Loschiavo et al., *First look at SND implementation within muon shield*, 2024. SHiP 30th Collaboration Week.

[55] D. Centanni et al., *AdvSND@LHC detector simulation and performances*, 2022. SND@LHC 10th Collaboration Meeting.

[56] D. Centanni, *Detector geometry and muon spectrometer performances*, 2023. SND@LHC 12th Collaboration Meeting.

[57] D. Centanni, *Magnetic Spectrometer Performances*, 2024. SND@LHC 16th Collaboration Meeting.

[58] A. Quercia et al., *Advanced SND@LHC magnet: the new "minimal" baseline design*, 2024. SND@LHC 18th Collaboration Meeting.